OUKA
Osaka University Knowledge Archive

Title	LOCALIZED STATES PROFILE AND CARRIER TRANSPORT IN AMORPHOUS SILICON ALLOYS
Author(s)	堤, 保雄
Citation	大阪大学, 1994, 博士論文
Version Type	VoR
URL	https://doi.org/10.11501/3097852
rights	
Note	

Osaka University Knowledge Archive : OUKA

https://ir.library.osaka-u.ac.jp/

Osaka University

LOCALIZED STATES PROFILE AND CARRIER TRANSPORT IN AMORPHOUS SILICON ALLOYS

アモルファスシリコン系合金材料の局在準位とキャリア輸送に関する研究

Yasuo TSUTSUMI

June, 1994

LOCALIZED STATES PROFILE AND CARRIER TRANSPORT IN AMORPHOUS SILICON ALLOYS

Yasuo TSUTSUMI

June, 1994

ABSTRACT

A series of systematic studies has been carried out on the measurements of localized states profile in the mobility gap as well as carrier transport property of amorphous silicon alloys. The density-of-states distribution and nature of deep localized states in undoped a-Si:H (Hydrogenated amorphous silicon) have been investigated by a newly developed gap-states spectroscopy, modulated photocurrent spectroscopy (MPCS), which is based on the frequency-resolved spectrum of modulated photocurrent with below-gap photoexcitation. The energy scale is directly specified by the energy of the subband-gap light populating the particular gap states. The MPCS has revealed two pronounced features in the gap-states distribution of undoped a-Si:H, one of which is assigned as due to the doubly occupied dangling bond (D^-) located about 0.5eV below the conduction band edge. The energy position of another deep localized states (named here H1 centre) is found to be about 0.54eV above the valence band edge, although the origin is not yet identified. Upon light soaking, the densities of not only the D^- centre but also H1 centre designate systematic changes, suggesting that these two centres are involved in the photo-induced degradation effects although the dangling bonds may play a central role in carrier recombination. The analysis for the pre-exponential factor of the thermal emission rate of the electron from the D^- centre suggests that the emission occurs in two stages through unrelaxed states.

MPCS has been utilized to investigate the energy location and nature of dangling bonds in undoped a-SiGe:H (Hydrogenated amorphous silicon germanium) and a-SiC:H (Hydrogenated amorphous silicon carbide) alloys having the band gap energy ranging from 1.16eV to 2.01eV, with a special focus on the doubly occupied dangling bond (D^-) centre. The energy depth of the D^- centre below the conduction band edge holds a well-defined linear dependence on the band gap energy. The Ge D^- centre lies by about 0.1eV below the Si D^- centre, while a sharp switch of the predominant deep centres occurs from Si dangling bonds to Ge dangling bonds as the Ge concentration approaches about 35 at.% which corresponds to an optical bandgap energy around 1.5eV. The analysis for the pre-exponential factor of the thermal emission rate of electron from the D^- centre suggests that different electron transition processes are operative for Si and Ge dangling bonds.

The gap-states profile in device-quality undoped a-Si:H have been investigated by means of time-resolved photocurrent spectroscopy (TPCS) on the practical solar cell configuration, with a particular emphasis on the states located shallower than well-identified dangling bond states. A new procedure of photocurrent analysis taking into account the multiple-trapping effects has been introduced to be accommodated to the shallow-lying states, showing the presence of distinct density-of-states structures in the energy interval between 0.25eV and 0.5eV from both the extended band edges.

Photothermal deflection spectroscopy (PDS) has been used to study the tail states at the band edges of a-Si:H alloys. The slope of the Urbach edge in the optical absorption spectrum involves informations about the valence band-tail states. The valence band-tail states are found to vary systematically with material composition and details of preparation conditions and/or thermal history.

A theory is developed on the absorption spectrum of amorphous semiconductors in the presence of an external electric field. Besides the isotropic third-derivative electroabsorption (EA) signal, the theory reveals the appearance of a polarization-dependent anisotropic EA signal characteristic of disordered media. Comparing the theoretical and experimental results on the EA effects, as well as the average dipole-matrix elements, enables evaluations of the mean

free path and the mobility. The result shows that the electron mobility reaches about $11.2cm^2/Vs$ for device-quality undoped a-Si:H, while the hole mobility is about 20% of the electron mobility. Alloying with carbon leads to a continuous reduction of mobility, with the largest drop (15%) for a carbon concentration of 10 at.%, this being in sharp contrast to a less-pronounced effect by germanium alloying.

Previous performance modeling of amorphous-based p-i-n junction devices has relied sometimes on the crystalline model or arbitrary choice of physical parameters. This work extends the modeling of amorphous-based devices taking into account of practical physical parameters of present-day a-SiGe:H alloys. Realistic efficiencies for both single and tandem junction devices are estimated with the optimum selections of the band gap. An efficiency around 14.7% is projected for a four-terminal two-cell tandem device with present-day best a-SiGe alloy having the band gap around 1.48eV. Additional efficiency improvement will be possible through utilization of optical confinement effect and introduction of photovoltaically active wide-window heterojunction materials, which would yield an enhancement of the efficiencies by a factor of about 20%.

ACKNOWLEDGMENT

The author would like to express his sincere thanks to Professor Yoshihiro Hamakawa for his constant advice and encouragement throughout the course of this thesis work and critical reading of this thesis.

This work has been done at the Semiconductor Laboratory, Faculty of Engineering Science, Osaka University, Toyonaka, Osaka and Department of Electrical Engineering, Akashi College of Technology, Akashi, Hyogo, under the direction of Professor Y. Hamakawa and Professor H. Okamoto, .

The author is deeply grateful to Professor H. Okamoto for his constant instructive and heartfelt advices and also his critical reading of this thesis. This work would not have been completed without his support.

The author wishes to express his gratitude to Professor emeritus S. Sakata of Akashi College of Technology for his constant encouragement.

The author is much indebted to Professor M. Okuyama, Dr. K. Hattori and Miss W. Ma of the Laboratory, Professor T. Nishino of Kobe University and Professor H. Takakura of Toyama Prefectural University for their useful advice and discussions throughout the course of this study. The author would like to express sincere gratitude to Mr. C. Sada of the Laboratory for his kind encouragement, useful discussion and skillful technical assistance throughout this thesis work.

The author wishes to give his highest appreciation to Professors S. Nitta, K. Shimakawa and S. Nonomura of Gifu University for their constant encouragement and useful suggestion. The author wishes to express his gratitude to his co-workers in the Semiconductor Laboratory, Messrs. K. Abe, T. Wada, K. Uchiyama, H. Yamamoto and S. Yoshihara for their valuable discussions and skillful collaboration.

The author is indebted to Messrs. N. Fujita, H. Itozaki, M. Ishii and T. Tomikawa of Itami Research Laboratories, Sumitomo Electric Industries, Ltd. for providing a-SiGe:H samples. The author is thankful to Mr. Y. Nitta of Kanegafuchi Chemical Co., Ltd. and Mr. Y. Hattori of

Nippon Denso Co., Ltd. for valuable discussions and encouragement.

The author wants to express his thanks to enjoyable and valuable discussions with other colleagues in the amorphous semiconductor research group; Professor D. Kruangam of Chulalongkorn University, Messrs. M. Deguchi, T. Toyama and M. Mori.

Finally the author wishes to thanks his wife and parents for their endless and warm encouragement.

CONTENTS

Chapter 1. INTRODUCTION

1-1. Historical background 1

1-2. Purpose of this work 3

References 6

Chapter 2. CHARACTERIZATION OF MID-GAP STATES

2-1. Introduction 8

2-2. Modulated photocurrent spectroscopy (MPCS) 9

2-2-1. Principle of MPCS 9

2-2-2. Simulation studies 15

2-2-3. Experimental details 16

2-3. Deep localized states in undoped a-Si:H 18

2-3-1. Density-of-states distribution 18

2-3-2. Attempt-to-escape frequency 23

2-3-3. Substrate temperature dependence of deep states 29

2-3-4. Light-induced changes 35

2-4. Deep localized states in undoped a-SiGe:H 39

2-4-1. Density and distribution of deep states 39

2-4-2. Energy location of doubly occupied dangling-bond centre 44

2-4-3. Electron transition process 50

2-5. Deep localized states in undoped a-SiC:H 55

2-6. Mobility-lifetime products 57

2-7. Summary 58

References 60

Chapter 3. CHARACTERIZATION OF SHALLOW LEVEL STATES

3-1. Introduction 63

3-2. Time-resolved photocurrent spectroscopy (TPCS) 64

3-2-1. Principle of TPCS 64

3-2-2. Simulation studies 67

3-2-3. Experiment details 68

3-3. Shallow level states in undoped a-Si:H 69

3-3-1. Electron traps 69

3-3-2. Hole traps 71

3-3-3. Density-of-states profile 72

3-3-4. Light-induced changes 73

3-4. Summary 77

References 78

Chapter 4. OPTICAL ABSORPTION NEAR BAND EDGES

4-1. Introduction 79

4-2. Outline of photothermal deflection spectroscopy (PDS) 79

4-3. Optical absorption spectra in a-Si:H alloys 81

4-3-1. Optical absorption tails in a-Si:H 83

4-3-2. Optical absorption tails in a-SiGe:H and a-SiC:H 89

4-4. Summary 90

References 91

Chapter 5. BAND-EDGE STATES AND CARRIER TRANSPORT PROPERTIES

5-1. Introduction 92

5-2. Polarized electroabsorption (EA) effects 93

5-2-1. Model and formulation 94

5-2-2. Low-field EA effects 96

5-2-3. Quantitative aspect of EA effects 98

5-2-4. Experimental details 100
5-3. General feature of polarized EA 101
5-4. Structural disorder and carrier mobility 104
5-4-1. Effect of deposition temperature in undoped a-Si-H 104
5-4-2. Effect of thermal annealing in undoped a-Si:H 107
5-4-3. Alloying effects 109
5-5. Summary 111
References 112

Chapter 6. DEVICE MODELING IN AMORPHOUS SILICON SOLAR CELLS
6-1. Introduction 113
6-2. Device modeling of single and tandem solar cell 114
6-3. Efficiency estimates for single and tandem devices 117
6-3-1. Built-in potential 117
6-3-2. Relation between film quality and conversion efficiency 119
6-4. Realistic efficiencies of single and tandem devices with present-day a-SiGe alloys 122
6-4-1. Determination of film quality parameters 122
6-4-2. Realistic efficiencies 125
6-5. Summary 126
References 127

Chapter 7. CONCLUSIONS 128

VITA 131

LIST OF PUBLICATIONS 132

Chapter 1. INTRODUCTION

1-1. Historical background

For many years it has been thought to be a basic and fundamental fact that an amorphous semiconductor could not be substitutionally doped [1]. Nevertheless, in 1975, W. E. Spear and P. G. LeComber demonstrated a new amorphous silicon material which can be doped [2]. It could be doped both n-type and p-type and its room temperature conductivity can be varied over more than ten orders of magnitude. It was discovered that a very important feature of this material is that it contains significant amounts of bonded hydrogen. The role of hydrogen in the atomic structure, the electronic structure, and the doping mechanism remains an outstanding problem to be addressed by both theoretical and experimental investigations. Nonetheless, doping of the material opened up possibilities for the fabrication of thin-film electronic devices, including photovoltaic solar cells. These exciting prospects have led to a recent explosion of experimental and theoretical works on hydrogenated amorphous silicon and other closely related materials.

One of the main asserts amorphous silicon has for semiconductor device applications is the ease by which its bandgap can be varied by alloying with other elements. The optical bandgap can be increased from 1.8eV (a-Si:H) to as high as 3.5eV by alloying with carbon [3]. Alloying with germanium has the opposite effect: it allows the band gap to be lowered continuously down to 1.0eV [4]. This precise control over the band gap can be utilized to optimize device performance and even to create novel device structures. Alloys have application in photovoltaic, electrophotography, light emitting devices and thin film transistors (TFTs), amongst others. In the amorphous silicon solar cells, there has been notable progress in recent years with the invention of amorphous silicon carbide (a-SiC) [5]. Because this alloy, a-SiC, has not only valence controllability with impurity doping (p-n control), but also energy gap controllability with variation of carbon content in the alloy system. This event opened up an amorphous silicon alloy age with a series of new materials such as amorphous silicon-germanium (a-SiGe), microcrystalline silicon (μc-Si), and amorphous silicon nitride (a-SiN). With these new materials, amorphous silicon solar cell efficiency is improving day by day. Although the in-line mass-

product efficiency is 8-9% for wide-area a-Si solar cells, the laboratory efficiencies are 13.2% with a-SiC/a-Si heterojunctions, 13.7% for a-Si/a-SiGe/a-SiGe triple-tandem junction, and 15.04% and 21.0% for a-Si/polycrystalline Si two- and four-terminal stacked junction solar cells [6].

However, this material has some peculiar effects: e. g., Steabler-Wronski effect [7], dispersive carrier transport, geminate recombination, etc. Origins of these anomalies are based upon an existence of large density of localized gap states due to the amorphous network system in the lattice structure configurations, as sketched in Fig.1-1. The sharp valence and conduction band edges are replaced by band tails extending into the energy gap. From a chemical point of view, these band tails arise from bond-length variation, bond-angle deviations, and/or dihedral-angle disorder, which are induced to relieve the internal strain in the overconstrained tetrahedral network. The structural constrains can also lead to the presence of defect configurations in which

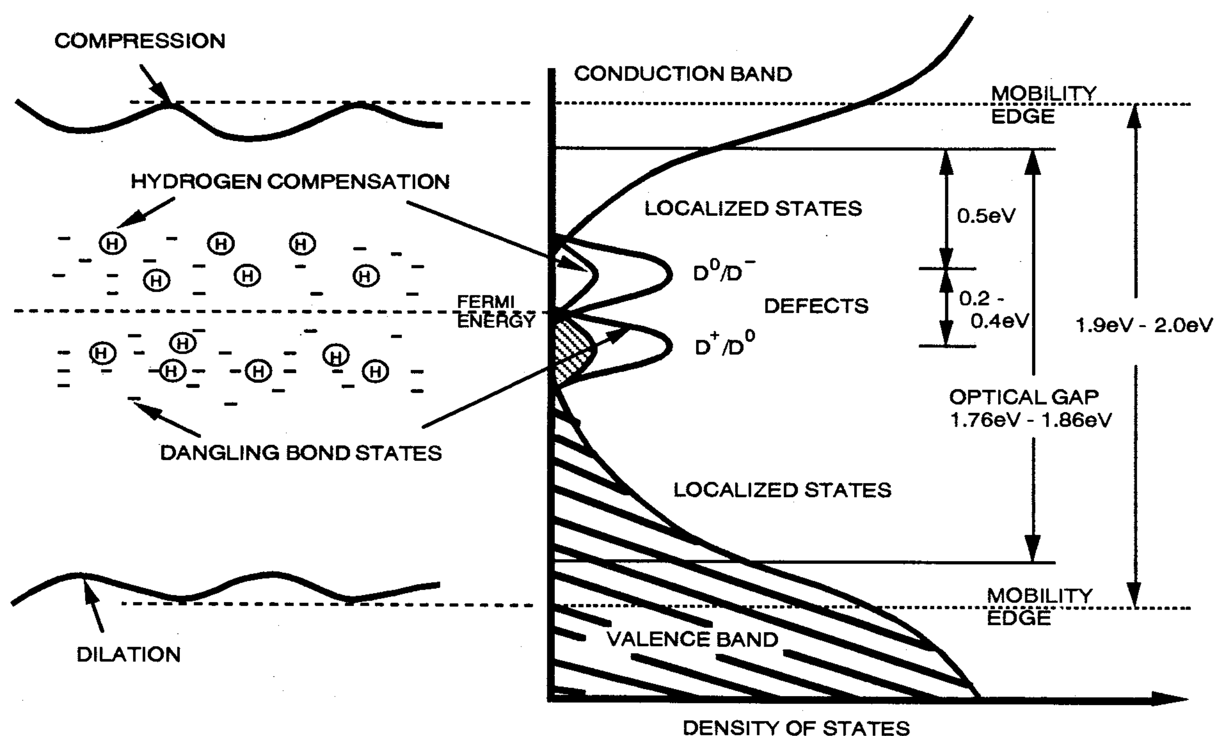

Fig. 1-1. (a) Schematic band diagram of a-Si (b) its energy distribution of electronic states showing the extended states and localized band tails of the ideal network and defect states in the gap.

the optimum number of nearest neighbors is not attained. Such strain-induced defects, as well as thermodynamically-induced defects, tend to create localized states in the gap. Thus it is necessary to understand the nature and density-of-states distribution of localized gap states and their role in the transport and recombination processes. At present, these properties have been investigated by several methods [8], which are transport methods (e. g. conductivity, photoconductivity, space-charge-limited-current SCLC, time-of-flight TOF), optical methods (e. g. photolumimescence PL, subband-gap absorption), structural methods and others (e. g. electron-spin-resonance ESR). However, it is not yet understood well, and needs extended investigations before the amorphous silicon technologies come into the established phase.

1-2. Purpose of this work

The prime feature of amorphous semiconductors is the absence of the steric constraints imposed by the structural symmetry and the necessary of the long-rang periodicity, which allows us to synthesize various kinds of multi-component alloys having tailor-made band gap. For the example, the band gap of amorphous silicon-based alloys can be continuously controlled from 1.0eV to 1.7eV in a-SiGe:H and from 1.8eV to 3.5eV in a-SiC:H. However, since these materials are formed with highly non-equilibrium condition, their properties are quite sensitive to the preparation conditions as well as the source materials, and optimization of the material processing technology is yet far beyond completed. It is clear that if amorphous silicon alloys possessing the film quality compatible with a-Si:H are actualized, they largely contribute to the further development of amorphous-based devices such as solar cell and photoreceptors. For this to be realized, the optimization of the material preparation technology should proceed along with the better understanding of the material properties, particularly the gap states density-of-states as well as band edge parameters which will play a central role in determining the electronic properties of the materials and thereby the performances of the devices made of them. The investigation of these properties is purpose of this thesis 9)-18).

In chapter 2, the density-of-states distribution and nature of deep localized states in undoped a-Si:H alloys (a-Si:H, a-SiGe:H and a-SiC:H) are investigated by a newly developed

gap-states spectroscopy, modulated photocurrent spectroscopy (MPCS), which is based on the frequency-resolved spectrum of modulated photocurrent with subband-gap photoexcitation. The energy scale is directly specified by the energy of the subband-gap light populating the particular gap states. The results are combined with those from ESR spin density and transport experiments, providing insights for the origin of the observed deep localized states and their role in carrier recombination. Two type of defect centres, one of which is assigned as due to a dangling bond, are observed in undoped a-Si:H. The author presents the density-of-states distribution and the nature of the two defect centres and discusses their implications for the role of two defect centres played in the light-induced phenomena of undoped a-Si:H. In addition, the author discusses the temperature dependence of the attempt-to-escape frequency and suggests that transitions through unrelaxed states of dangling bond centres might be important. Furthermore, the result of experiments on a-SiGe:H and a-SiC:H alloys with bandgaps between 1.16eV to 2.01eV is presented. The energy of the doubly occupied dangling-bond centres exhibits a systematic shift with the bandgap energy, while the density of the dangling-bond centre gradually increases upon decreasing the bandgap. On the basis of experimental data, the author discusses the identity of the dangling bonds in association with carrier transition process through the Si and Ge dangling-bond centres.

In chapter 3, the author approaches the localized states distribution with the use of time-resolved photocurrent spectroscopy (TPCS) on the practical a-Si:H solar cell structure. The experimental procedure is identical with that in conventional Time-of-Flight measurement, while a new analytical procedure is introduced to extract localized states distribution from photocurrent transients. Shortly speaking, effects of multiple trapping process are precisely taken into account, without which deduced density-of-states profile tends to involve a large ambiguity, particularly for the shallower energy region. The analysis of the TPCS spectra indicates the presence of distinct density-of-states structures in the energy interval between 0.25eV and 0.5eV from each the extended band edge.

In chapter 4, the optical absorption spectra of various a-Si:H alloys measured by photothermal deflection spectroscopy (PDS) method are presented. The exponential portion of

the optical absorption spectrum is referred to as the Urbach tail. The Urbach energy simply reflects the valence band-tail, because the characteristic energy of the conduction band tail is much smaller than that of the valence band tail. Since the band tail arises from disorder in the amorphous network, it is to be expected that any modification of the network will be reflected in the distribution of the band tails. The results indicate that the Urbach energy systematically changes with material composition and details of preparation conditions and/or thermal history, which is likely to reflect the changing distribution of valence band-tail states.

Chapter 5 describes a low-field electroabsorption (EA) theory in which the effects of disorder are incorporated in the context of a site-disordered tight-binding (TB) model. Besides the isotropic third-derivative EA signal, the theory reveals the appearance of a polarization-dependent anisotropic EA signal characteristic of disordered media. The author reaches the conclusion that the polarization-dependent EA effect arises essentially from a field-induced change in the matrix element for optical transition involving localized states near the band edge, so that it serves as an indicator for the degree of disorder in amorphous semiconductors. Comparing the theoretical and experimental results on the EA effects, as well as the average dipole-matrix elements, enables evaluations of the carrier mean free path and the carrier mobility in the vicinity of band edges. The result of experiments on various a-Si:H alloys by the polarized EA method indicates that the mobility varies systematically with material composition and details of preparation conditions and/or thermal history, although the range of variation is not so significant (less than 20%) so long as the material studied in this work are concerned.

In chapter 6, the modeling of amorphous-based devices taking into account of practical physical parameters of present-day a-SiGe:H alloys is presented. This model can be used to extract information about physical parameters responsible for the photovoltaic performances in actual device structures. The author also characterizes several physical parameters in the p-i-n junctions using a-SiGe:H alloys of various band gaps, and evaluates realistic efficiencies for geometrically optimized devices. Realistic efficiencies expected for both single and tandem junction devices are demonstrated with the optimum selections of the band gap.

In the final chapter, main conclusions obtained in this thesis work are summarized.

References

(1) N. F. Mott, Phil. Mag. 19 (1969) 835.

(2) W. E. Spear and P. G. LeComber, Solid St. Commun., 17 (1975) 1193.

(3) F. W. Smith, J. Appl. Phys. 55 (1984) 764.

(4) J. Chevaller, H. Wieder, A. Onton and C. R. Guarnieri, Solid St. Commun., 24 (1977) 867.

(5) Y. Tawada, M. Kondo, H. Okamoto and Y. Hamakawa, Solar Energy Mat., 6 (1982) 237.

(6) Y. Hamakawa W. Ma and H. Okamoto, MRS Bulletin, Vol XVII, 10 (1993) 38.

(7) D. L. Staebler and C. R. Wronski, Appl. Phys. Lett., 31 (1977) 292.

(8) R. A. Street and D. K. Biegelsen, Hydrogenated Amorphous Silicon II, edited by J. D. Joannopoulos and G. Lucovsky (Springer-Verlag, Berlin and New York, 1984), p195.

(9) Y. Tsutsumi, S. Sakata, K. Abe, Y. Nitta, H. Okamoto and Y. Hamakawa, J. Non-Cryst. Solids, 97/98 (1987) 1063.

(10) Y. Tsutsumi, K. Abe, Y. Nitta, H. Okamoto and Y. Hamakawa, Tech. Dig. of the International PVSEC-3, Tokyo (1987) 675 .

(11) K. Abe, H. Okamoto, Y. Nitta, Y. Tsutsumi, K. Hattori and Y. Hamakawa, Phil. Mag. B, 58 (1988) 171.

(12) Y. Tsutsumi, H. Okamoto and Y. Hamakawa, Phil. Mag. B, 60 (1988) 695.

(13) H. Okamoto, Y. Tsutsumi, K. Abe and Y. Hamakawa, Proc. 4th International PVSEC, Sydney (1989) 71.

(14) Y. Tsutsumi, K. Uchiyama, H. Okamoto and Y. Hamakawa, J. Non-Cryst. Solids, 114 (1989) 627.

(15) Y. Tsutsumi, K. Uchiyama, H. Okamoto and Y. Hamakawa, Tech. Dig. of the International PVSEC-5, Kyoto (1990) 809.

(16) Y. Tsutsumi, H. Yamamoto, K. Hattori, H. Okamoto and Y. Hamakawa, J. Non-Cryst. Solids 164-166 (1993) 893.

(17) Y. Tsutsumi, H. Okamoto, K. Hattori and Y. Hamakawa, Phil. Mag. B, 69 (1994) 253.

(18) Y. Tsutsumi, H. Okamoto, K. Hattori and Y. Hamakawa, Mat. Res. Soc. Symposium Proceeding Vol."Amorphous Silicon Technology-1994", (1994) (in press).

Chapter 2. CHARACTERIZATION OF MID-GAP STATES

2-1. Introduction

Deep localized states in the mobility gap play a central role in determining the transport and recombination properties of amorphous semiconductors. Since these properties are closely linked with device performance, it is of a great importance to obtain information about the nature, density and distribution of localized gap states arising from structural defects. Several approaches are considered, of which the most powerful are the methods utilizing capacitance transients like deep-level transient spectroscopy (DLTS)[1] and isothermal capacitance transient spectroscopy (ICTS)[2]. However, if undoped materials of high resistivity which play a central role in photocurrent generation are to be focused, these well-tested techniques tend to loss their essential advantages. As an alternative way, we have developed a new gap-states spectroscopy, modulated photocurrent spectroscopy (MPCS), which is based on the frequency-resolved spectroscopy of junction photocurrent under subband-gap illumination[3][4]. MPCS can be satisfactorily applied to undoped materials of high resistivity since it employs the frequency-resolved spectrum. Energy scaling is one of the most important tasks in every gap-state spectroscopy. In MPCS the energy scale is specified by the energy of subband-gap light which is used to populate the particular gap states. The direct photoexcitation of gap states and subsequent thermal emission give rise to a time-varying space charge, which results in displacement currents of opposite signs for electron and hole transitions. This phenomenon provides the capability of identifying the contribution of electron and hole emissions. MPCS enables us to obtain information about the nature, density and energy locations of deep states in undoped a-Si:H alloys.

In this chapter, the author presents an outline of MPCS as well as the results of experiments, which have been carried out on practical photovoltaic devices consisting of undoped a-Si:H, a-SiGe:H and a-SiC:H alloys as a photosensitive layer. The results are combined with those from ESR and transport experiments, providing insights for the origin of the observed deep-states and their role in carrier recombination. The result of the experiments for undoped a-Si:H leads us to the conclusion that the D^- states have a near-Gaussian distribution centered at

around 0.5eV below the conduction band edge.[3)6)] In addition, the author discusses the temperature dependence of the attempt-to-escape frequency and suggests that transitions through unrelaxed states of dangling bond centres might be important. The result of experiments is presented on undoped a-SiGe:H and a-SiC with bandgaps between 1.16eV to 2.01eV measured by means of the MPCS [4)-6)], showing that the energy of the doubly occupied dangling-bond centres exhibits a systematic shift with the bandgap energy, while the density of the dangling-bond centre gradually increases on decreasing the bandgap. On the basis of experimental data, The identity of the dangling bonds is discussed in association with carrier transition process through the Si and Ge dangling-bond centres. Finally, the author presents the experimental results of light-induced changes in the deep states of undoped a-Si:H and discusses their implications for the role of two kinds of deep-lying centres played in the light-induced phenomena of undoped a-Si:H.[7)]

2-2. Modulated photocurrent spectroscopy (MPCS)

2-2-1. Principle of MPCS

MPCS is concerned with the frequency-resolved spectrum of the modulated photocurrent (MPC) which is measured under chopped excitation light of energy less than the bandgap energy ε_g. Consider a p-i-n junction or Schottky barrier cell, the photosensitive region (undoped a-Si:H, a-SiGe:H or a-SiC:H) of which contains deep localized states distributed continuously through the gap, and assume that they are empty in thermal equilibrium. On illumination with subband-gap light of energy $h\nu$, as shown in Fig.2-1, the states located deeper than the energy ε_g-$h\nu$ from the conduction band edge ε_c are populated with non-equilibrium electrons through optical transitions from the valence band to these states. The non-equilibrium electrons placed at energy ε below ε_c are then thermally released into the conduction band at the rate $E_n(\varepsilon)$ which can be represented in terms of attempt-to-escape frequency ν_n as

$$E_n(\varepsilon) = \nu_n \exp(-\varepsilon / kT), \qquad (2\text{-}1)$$

where k denotes the Boltzmann constant and T the absolute temperature. If the emission takes place within one period of light modulation, that is $E_n(\omega) \geq \omega$, where ω denotes the modulation frequency, then the induced photocurrent follows the modulation sequence and thereby contributes to the in-phase MPC $J_0(\omega)$.

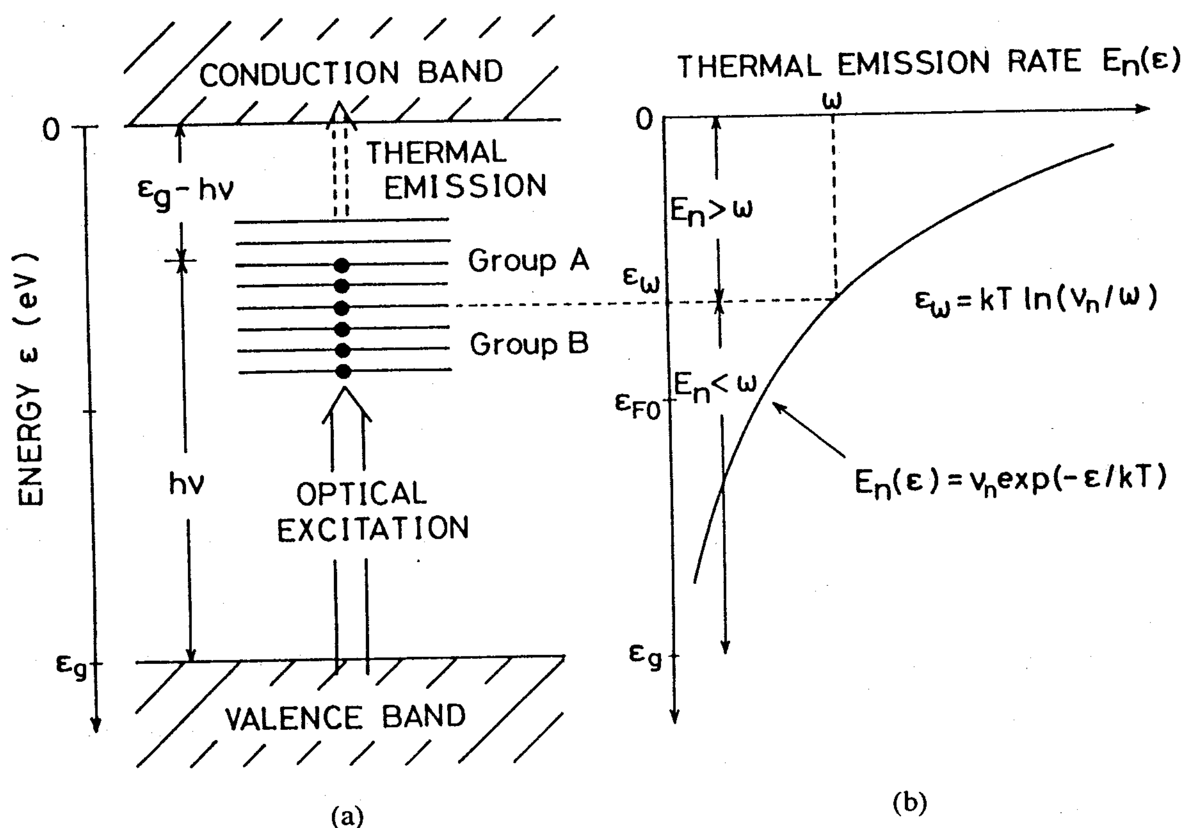

Fig. 2-1. (a) Energy level scheme for analysis of the MPC, showing the photocurrent generation process; optical excitation of localized states followed by thermal emission of electrons into the conduction band. The states located deeper than ε_g-$h\nu$ from the conduction band edge are populated with electrons by the subband-gap photoexcitation of a energy $h\nu$, and contribute to the photocurrent generation. (b) the thermal emission rate $E_n(\varepsilon)$ against the energy depth from the conduction band edge ε_g.

As indicated in Fig.2-1, the deep localized states are approximately classified into two groups with a characteristic energy depth

$$\varepsilon_\omega = kT \ln(\nu_n / \omega) , \tag{2-2}$$

at which the thermal emission rate coincides with the modulation frequency ω [10]. Since $E_n(\omega) \geq \omega$ is satisfied for the states lying at energies shallower than ε_ω (group A in the figure), the electron transitions through these states contribute to the generation of in-phase MPC $J_0(\omega)$. Therefore, $J_0(\omega)$ is roughly related to the density $D(\omega)$ of states by

$$J_0(\omega) \propto \int_{\varepsilon_g - h\nu}^{\varepsilon_\omega} D(\varepsilon) d\varepsilon . \tag{2-3}$$

If we define the MPCS signal $S(\omega)$ as the logarithmic derivative of $J_0(\omega)$ with respect to the modulation frequency ω, eqn. (2-3) readily yields

$$S(\omega) = \partial[J_0(\omega)] / \partial(\ln \omega) \propto -kTD(\varepsilon_\omega) . \tag{2-4}$$

This equation represents the basic relation with which the density $D(\varepsilon)$ of states is derived from the MPCS signal $S(\omega)$.

The simple discussion above does not include the contribution from a displacement current produced by the time-varying space charge in the deep localized states. The modulated photocurrent (MPC) induced by the chopped excitation light of the form $\exp(i\omega t)$ consists of two parts; one arises from the thermal emission of electrons and the other from the displacement current produced by the time-varying space charge at the charged states. According to a recent theory [8)9)], the MPC J_ω due to electron transitions through the deep states having a distribution $D(\varepsilon)$ is readily formulated as

$$J_\omega = A\int_{\varepsilon_g-h\nu}^{\varepsilon_{F0}} [E_n(\varepsilon)-i(\gamma-\tfrac{1}{2})\omega]/[E_n(\varepsilon)-i\omega]D(\varepsilon)d\varepsilon\,, \qquad (2\text{-}5)$$

where A is proportionality constant, ε_{F0} is the equilibrium Fermi energy measured from the conduction band edge ε_c, and γ denotes the geometrical factor which represents the conduction of displacement current and ranges from 0 to 1 depending on the junction property. This equation holds good as long as the MPC is measured with a weak subband-gap illumination under an appropriate reverse-bias condition so that the thermal equilibrium state of deep states occupancy is not so significantly disturbed and the effect of carrier recombination is ignored.

It is convenient to introduce the function $f_\omega(\varepsilon)$ defined by

$$f_\omega(\varepsilon) = \{1 + \exp[2(\varepsilon - \varepsilon_\omega)/kT]\}^{-1}\,. \qquad (2\text{-}6)$$

No explanation will be needed for the properties of $f_\omega(\varepsilon)$ since its form is the same as that of the Fermi-Dirac function; however, now the Fermi energy and temperature T are replaced with ε_ω and T/2, respectively. The real part of eqn.(2-5), which corresponds to the in-phase component $J_0(\omega)$ of the MPC measured by the lock-in technique, is then written as

$$J_0(\omega) = A[-(\gamma-\tfrac{1}{2})\int_{\varepsilon_g-h\nu}^{\varepsilon_{F0}} D(\varepsilon)d\varepsilon + (\gamma+\tfrac{1}{2})\int_{\varepsilon_g-h\nu}^{\varepsilon_{F0}} f_\omega(\varepsilon)D(\varepsilon)d\varepsilon]\,. \qquad (2\text{-}7)$$

As shown in Fig.2-1, the frequency-dependent term of $J_0(\omega)$, the second term of eqn.(2-7), arises from the electron transitions through the deep states located in the energy interval between ε_g-$h\nu$ and the energy ε_ω. Namely, defining the MPCS spectrum $S(\omega)$ as $\partial J_0(\omega)/\partial\ln\omega$, we have

$$S(\omega) = \partial[J_0(\omega)]/\partial(\ln\omega) = -A(\gamma+\tfrac{1}{2})kT\int_{\varepsilon_g-h\nu}^{\varepsilon_{F0}} [-\partial f_\omega(\varepsilon)/\partial\varepsilon]D(\varepsilon)d\varepsilon\,. \qquad (2\text{-}8)$$

The integration of eqn.(2-8) can be readily performed according to standard procedures for Fermi-Dirac statistics. The upper limit of the integral ε_{F0} is replaced by infinity since $\varepsilon_{F0}-\varepsilon_{\omega}>>kT/2$ will usually hold, while particular care should be paid to treat properly the lower limit of the integral. When the condition $\varepsilon_{\omega}-\varepsilon_{g}+h\nu>>kT/2$ is satisfied or, in other words, when the modulation frequency ω is substantially smaller than the characteristic frequency ω_c defined by $\omega_c=\nu_n \exp[(h\nu-\varepsilon_g)/kT]$, the lower limit can be replaced by $-\infty$ with practically no loss in accuracy. Then, eqn.(2-8) leads to the relation

$$D(\varepsilon_{\omega}) = -[A(\gamma+\tfrac{1}{2})kT]^{-1}S(\omega)\,. \qquad (2\text{-}9)$$

If the amplitude of the MPCS spectrum is normalized by that measured under uniformly absorbed bandgap light of an identical photon flux, the parameter A in this relation is given by

$$A = \sigma_{opt} / \alpha_{ag}\,, \qquad (2\text{-}10)$$

where σ_{opt} denotes the optical cross-section of the deep state and α_{ag} the absorption coefficient for band-gap light. As described above, to obtain the absolute value of the state density requires the magnitude of the optical cross-section as well as the γ value. Since these are not always known exactly except in some special cases, MPCS alone does not provide fully quantitative information about the state density. This point is a main drawback of MPCS and should be overcome by combining it with other characteristic techniques.

On the other hand, in the modulation frequency region $\omega\cong\omega_c$, the following relation is derived:

$$S(\omega)\,\omega \propto \omega_c\omega / (\omega_c^2+\omega^2)\,. \qquad (2\text{-}11)$$

Equation (2-11) indicates that $S(\omega)\omega$ exhibits a maximum at $\omega=\omega_c$ in the modulation frequency domain. This property is readily used to convert the frequency into the energy scale by relying

on the photon energy:

$$\varepsilon_\omega = \varepsilon_g - h\nu + kT \ln (\omega_c/\omega) . \qquad (2\text{-}12)$$

Similarly, the attempt-to-escape frequency ν_n is estimated from

$$\nu_n = \omega_c \exp [(\varepsilon_g - h\nu) / kT] . \qquad (2\text{-}13)$$

Note that eqns.(2-11) and (2-12) assume energy-independent ν_n for appreciably wide ranges of the state distribution; otherwise the energy scale and the ν_n value are valid only for the states located just at an energy ε_g-hν below ε_c. In turn, if the MPCS spectrum measured with different photon energies hν results in an identical density-of-states distribution in the energy scale, the above assumption might be well justified.

We have focused on the MPC due to electron transitions through the deep states which are empty in thermal equilibrium. The MPC of undoped a-Si:H alloy consists of another contribution, that is the contribution of hole emission from deep states which are filled by electrons in thermal equilibrium. If the MPC due to this process dominates, the corresponding MPCS spectrum will reflect the density-of-states distribution of the deep states above the valence band edge. In this case, however, the constant γ in eqn. (2-9) should be replaced by $-\gamma$, and therefore, if γ is greater than 1/2, the MPCS signal exhibits a different sign from that related to the electron traps. This property can readily be used to identify the origin of the MPCS signal and resulting density of states. The γ value is approximately evaluated from

$$\gamma = \left| \tfrac{1}{2} - J_0(\infty) / J_0(0) \right| , \qquad (2\text{-}14)$$

which is easily derived from eqn.(2-7). The recent phase-shift analysis for the MPC of a-Si:H p-i-n junctions has shown that γ takes a value exceeding 1/2 at temperatures below about 290K[11]. Consequently, it can be stated that the MPCS electron-emission signal possesses a negative

sign, and the MPCS hole-emission signal a positive sign, just as is the case for the DLTS or ICTS signal based upon capacitance transients.

2-2-2. Simulation studies

Simulation studies were made to examine the accuracy of the present MPC spectroscopy, particularly that of the procedure for determining the energy scale. The exact values of the amplitude and phase of the MPC are calculated using eqn.(2-5) as a deep states (D^-), having a

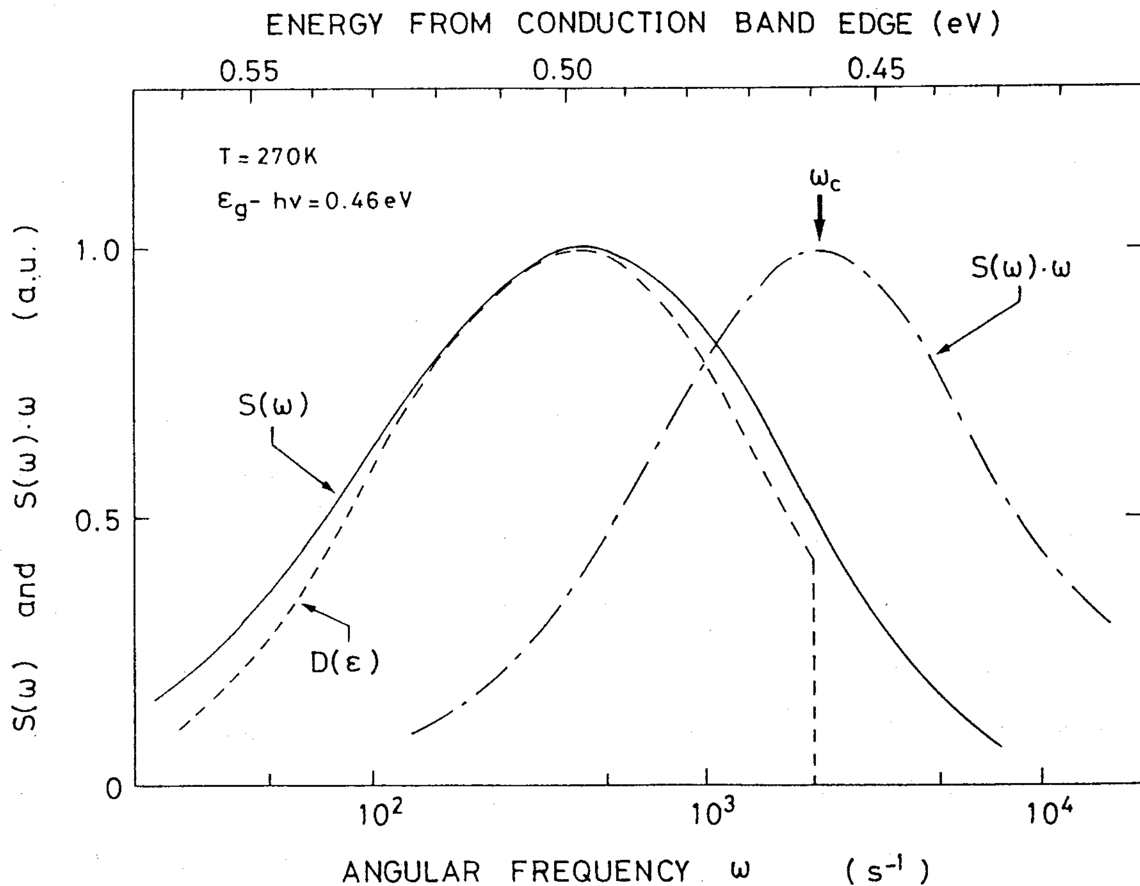

Fig. 2-2. MPCS spectrum $S(\omega)$ plotted against modulation frequency ω calculated for Gaussian deep states distribution $D(\varepsilon)$ with a lower energy cut-off ε_g-$h\nu$ at 0.46eV. The energy scale for the upper horizontal axis is determined by correlating the peak frequency ω_c of $S(\omega)\omega$ with the cut-off energy 0.46eV. Details are described in the text.

peak energy 0.5eV and a standard deviation 0.03eV. The energy ε_g-hν deeper than which the deep states are populated by subband-gap light is set to be 0.46eV. The parameters used for calculation are T=270K, γ=0.65 and $\nu_n=10^{12}s^{-1}$. The MPCS signal S(ω) and the function S(ω)ω are obtained for the calculated amplitude and phase, and shown in Fig.2-2 as a function of the modulation frequency ω. The original deep states distribution D(ε) with a lower cut-off energy, 0.46eV, is also presented in this figure by the dashed line. It is clear that S(ω) reproduces well the original distribution D(ε) in the frequency domain. From the peak frequency of the function S(ω)ω, $\omega_c=2150s^{-1}$, the attempt-to-escape frequency ν_n is determined from eqn.(2-13) to be $8x10^{11}s^{-1}$, which is close to the given value. The energy scale is thus determined either from this ν_n value or more directly following eqn.(2-12), and given by the upper horizontal axis. The deduced peak energy of the deep states is 0.497eV, again being in good agreement with the set value 0.5eV. The accuracy in the reproducibility of the density-of-states distribution generally becomes better for a broader distribution.

2-2-3. Experimental details

The samples employed in this work were p-i-n junction or Schottky barrier photocells consisting of undoped a-Si:H, a-SiGe:H or a-SiC:H alloys having bandgap energies ranging from 1.16eV to 2.01eV. For a-Si:H samples employed in this work, the cell structure was glass/ITO/p a-SiC:H/i (undoped) a-Si:H/ n μc-Si:H/Al. The amorphous and microcrystalline layers were prepared by the r.f. plasma deposition technique from an SiH_4/H_2 (1:9) mixture containing the desired amount of CH_4, B_2H_6 or PH_3. So as to avoid cross-contamination, each layer was formed in a separated individual chamber. For a-SiGe:H and a-SiC:H, the cell structures was glass/SnO_2/undoped a-Si:H, a-SiGe:H or a-SiC:H (0.5-1.5μm)/n-(a-Si:H)(300Å)/Al. Undoped a-SiGe:H and a-SiC:H films were prepared by r.f. plasma chemical vapor deposition from a gas mixture of SiH_4-H_2(1:9) and GeH_4-H_2(1:9) or CH_4 with the desired volume ratios. The substrate temperature during the deposition was 300°C (a-SiGe:H) and 250°C (a-SiC:H). The other deposition parameters such as r.f. power were chosen so as to obtain the best film quality for each Si-to-Ge(Si-to-C) ratio or bandgap energy.

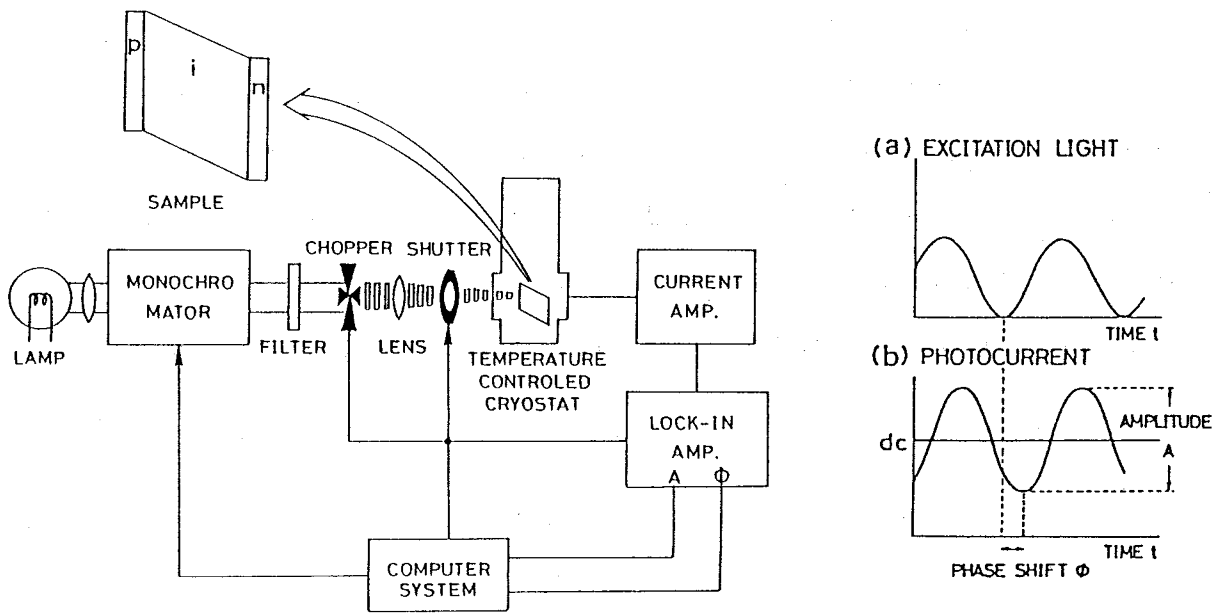

Fig. 2-3. Experimental set-up for MPCS measurement employed in this work.

In Fig.2-3, the experimental set-up for MPCS measurement employed in this work is illustrated. The MPC was measured as a function of the chopping frequency f under a suitable reverse bias, say about -1V, using a two-phase lock-in amplifier with a fast current amplifier. The samples, which were mounted in an evacuated, temperature-controlled optical cryostat, were illuminated with monochromatic light of various fixed photon energies. The incident photon flux was of the order of 10^{14} photons $cm^{-2}s^{-1}$. The chopping frequency f was varied from 0.5Hz to 10kHz, and the amplitude and phase of the subband-gap MPC were simultaneously monitored. To compensate the frequency dependencies of the measurement system as well as the junction property, these values were normalized by the corresponding values measured with uniformly absorbed bandgap light, for which the absorption coefficient is about $2x10^4$ cm^{-1} in this experiment, yielding the in-phase signal $J_0(\omega)$ as a function of the angular frequency $\omega(2\pi f)$ of modulation. The in-phase signal $J_0(\omega)$ was converted into the MPCS signal $S(\omega)$. The data acquisition and data processing were all provided by an ordinary personal computer system.

2-3. Deep localized states in undoped a-Si:H

2-3-1. Density-of-states distribution

In this section, the author describes the MPCS spectra on undoped a-Si:H and discusses the energy location and the nature of the deep localized states, specially the doubly occupied dangling bond (D^-) states [3)6)]. The deduced deep-states density-of-state (DOS) of undoped a-Si:H reveals several pronounced structures including the D^- centre.

Figure 2-4(a) shows the MPCS spectra S(ω) at various temperatures ranging from 260 to

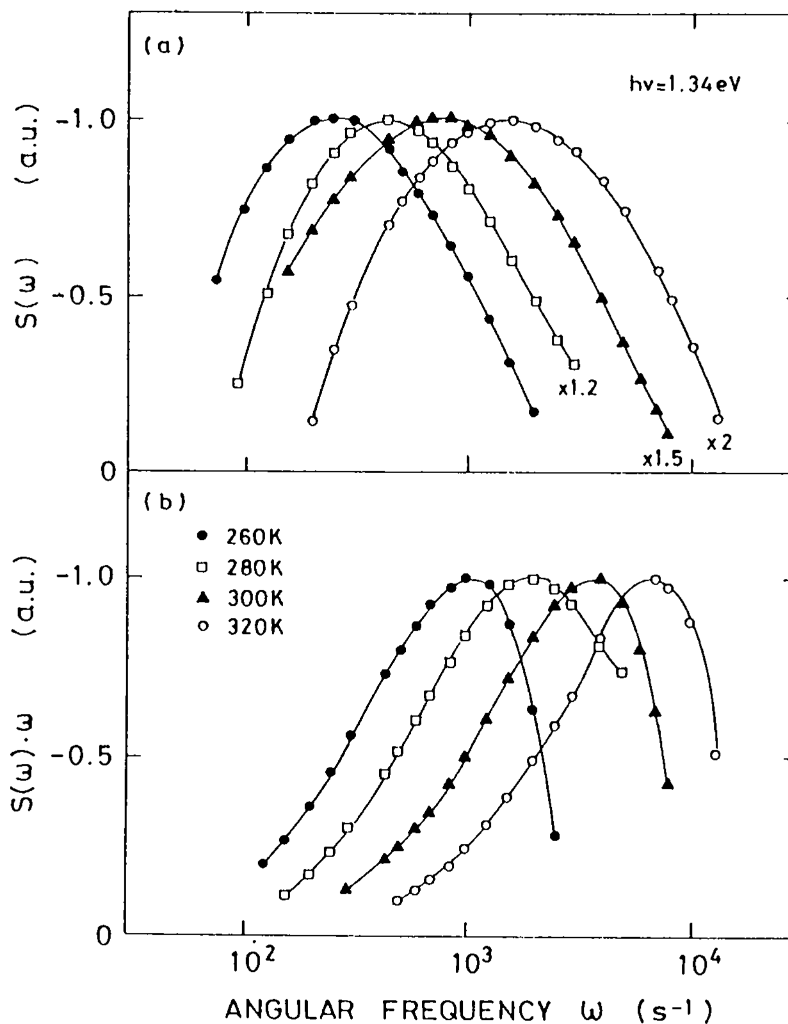

Fig. 2-4. (a) MPCS spectra S(ω) measured on an a-Si:H p-i-n junction at various temperatures. The frequency ω_c at which the function S(ω)ω, shown in (b), attains its maximum corresponds to the energy depth 0.42eV from the conduction band edge.

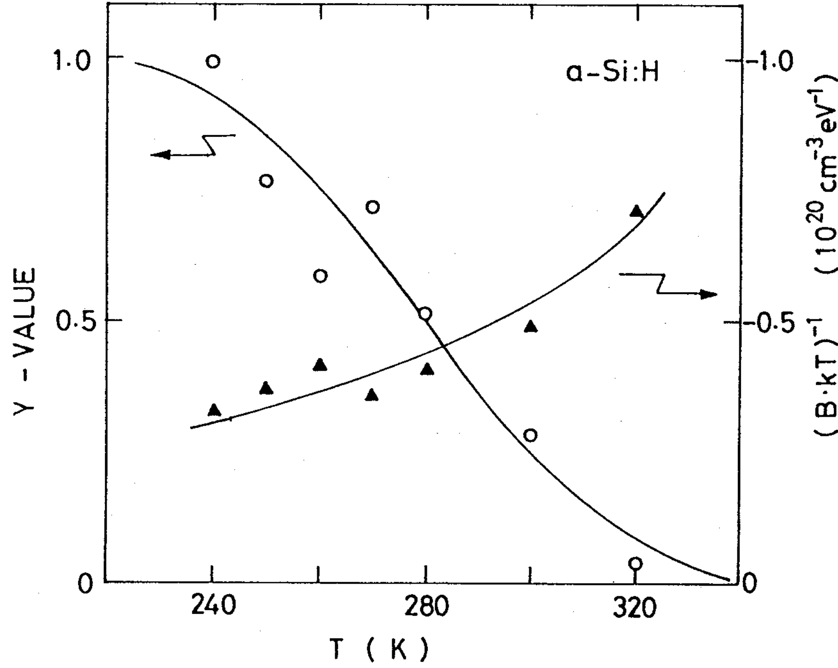

Fig. 2-5. The γ-value estimated with eqn. (2-14) is plotted against measurement temperature. The proportionality factor $(BkT)^{-1}$ relates the DOS $D(\varepsilon_\omega)$ with the MPCS signal $S(\omega)$, eqn. (2-9), is also presented. Here, the optical cross section σ_{opt} of the DB centre is assumed to 10^{-16} cm^2.

320K on undoped a-Si:H deposited at the substrate temperature T_S=180°C. The excitation photon energy hν was chosen to be 1.34eV. Since the band gap energy ε_g is 1.76±0.01eV in this temperature range, deep states located deeper than an energy ε_g-hν =0.42eV from both the extended band edges are populated, and contribute to the MPCS signal. The γ values estimated by eqn. (2-14) is plotted against measurement temperature in Fig.2-5, where the prefactor $(BkT)^{-1}$ in eqn. (2-9) is also given assuming the optical cross section at 10^{-16} cm^2, here $B=-(\sigma_{opt}/\alpha_{ag})(\gamma+1/2)$. Therefore, at least for temperatures below 280K, the γ value is greater than 0.5, so that the sign of S(ω) identified whether the MPCS signal represents electron emission or hole emission. The negative sign of S(ω) then indicates that the signal in Fig.2-4(a) arises from electron emission, which we assign as due to the D^- states. As shown in the figure, the spectrum S(ω) shifts towards the lower frequency region with decreasing temperature. This trend is understood as being a natural consequence of the lowered thermal emission rate with decreasing

temperature.

The function $S(\omega)\omega$, shown in Fig.2-4(b), exhibits a well defined peak as predicted in the previous section, and again shows a reasonable shift with temperature. The modulation frequency, at which the function $S(\omega)\omega$ takes a maximum, gives an estimate of the characteristic frequency ω_C defined in section 2-2. Then, the modulation frequency ω is converted into the energy measured from the conduction band edge ε_C according to eqn.(2-12) for each temperature.

The density-of-states distribution $D(\varepsilon)$ of the D^- centre thus obtained is plotted against the energy depth from ε_C in Fig.2-6. As shown in this figure, the MPCS spectra $S(\omega)$ measured under different conditions, when plotted against the energy scale, give a completely identical

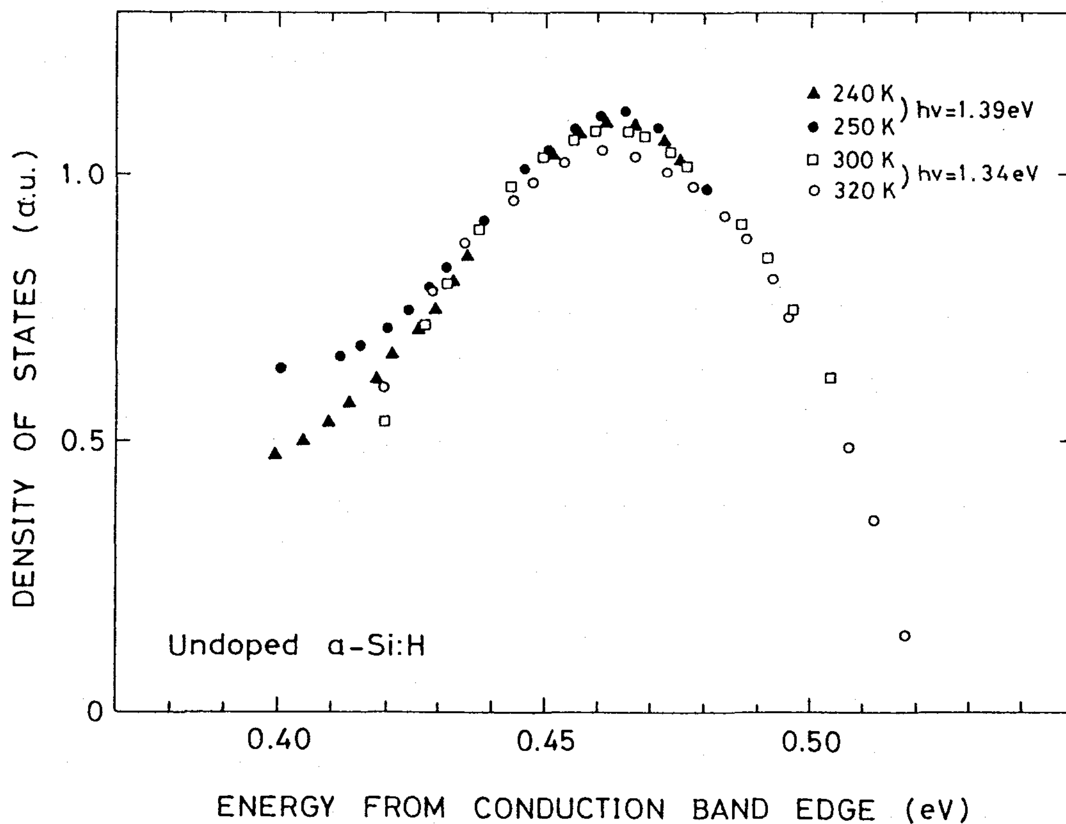

Fig. 2-6. DOS distribution of D^- centre in an undoped a-Si:H determined from the MPCS spectra. Measurements made under different conditions give an identical result.

result, indicating a negligibly small energy dependence of the attempt-to-escape frequency ν_n within the energy rang covered by the measurements. It is found that the D^- centre has a distribution with a near-Gaussian shape centered at an energy about 0.47eV below ε_c with a standard deviation of about 0.04eV. Moreover, the absolute peak magnitude of DOS is evaluated to be about 1.5×10^{17} $cm^{-3}eV^{-1}$ by assuming the optical cross section at 10^{-16} cm^2.

We have applied the present method to undoped a-Si:H prepared under various different deposition conditions. The result shows that the peak energy of the D^- centre is almost identical for each sample and in the range of 0.45-0.56eV depending on the energy band gap, while the s value which represents the width of state distribution is rather sensitive to the total dangling bond (DB) density, varying from 0.33eV to about 0.1eV with decreasing DB density.

In the present gap-state spectroscopy, the energy scale is determined by the energy of subband-gap light which is used to populate the deep states. The probable error in the energy scale then arises from the lattice relaxation energy ε_r involved in the related optical transition. This leads to a correction of the energy scale by $\varepsilon_r/2$. Since ε_r is estimated to be at most 0.1eV for dangling bond trandisions [12)-15)], the best value for the average corrected peak energy of the D^- centre is 0.5eV±12% for undoped a-Si:H with optical band gaps in the range 1.72-1.85eV. The peak energy is consistent with those evaluated by ICTS [2)], ODMR [16)] and PA [13)].

When the measurement is made with a higher photoexcitation energy and lower temperatures, the MPCS signal associated with another electron trap becomes observable in the high-modulation frequency region, as shown in Fig.2-7. The MPCS spectrum of the shallower states (named here as E1 states) is well fitted by the line-shape function of the MPCS for a discrete level, $[\omega\omega_p/(\omega^2+\omega_p^2)]^2$, where ω_p is the peak frequency related to the energy depth ω_{E1} and the attempt-to-escape frequency ν_{E1} by $\nu_{E1}\exp(-\varepsilon_{E1}/kT)$. This indicates that the E1 states have a very sharp distribution in the gap, presumably much less than the f.w.h.m. of the MPCS line-shape function around 1.76kT in energy. The temperature variation of the E1 peak magnitude is consistent with that expected for discrete levels. Concerning the energy position, the procedure used for the D^- centre cannot be immediately applied because of the descrete nature of the E1 states. Instead, assuming a weak temperature dependence of the prefactor ν_{E1}, we roughly esti-

mate the energy ε_{E1} at zero temperature from the Arrhenius plot of the peak frequency ω_p measured in the temperature range from 200 to 250K. The estimated value is ε_{E1}=0.40eV±10%, with a prefactor value of $\nu_{E1} \approx 3 \times 10^{12} s^{-1}$.

As to the origin of the E1 states, we tentatively assign it as the unrelaxed state of the D^-

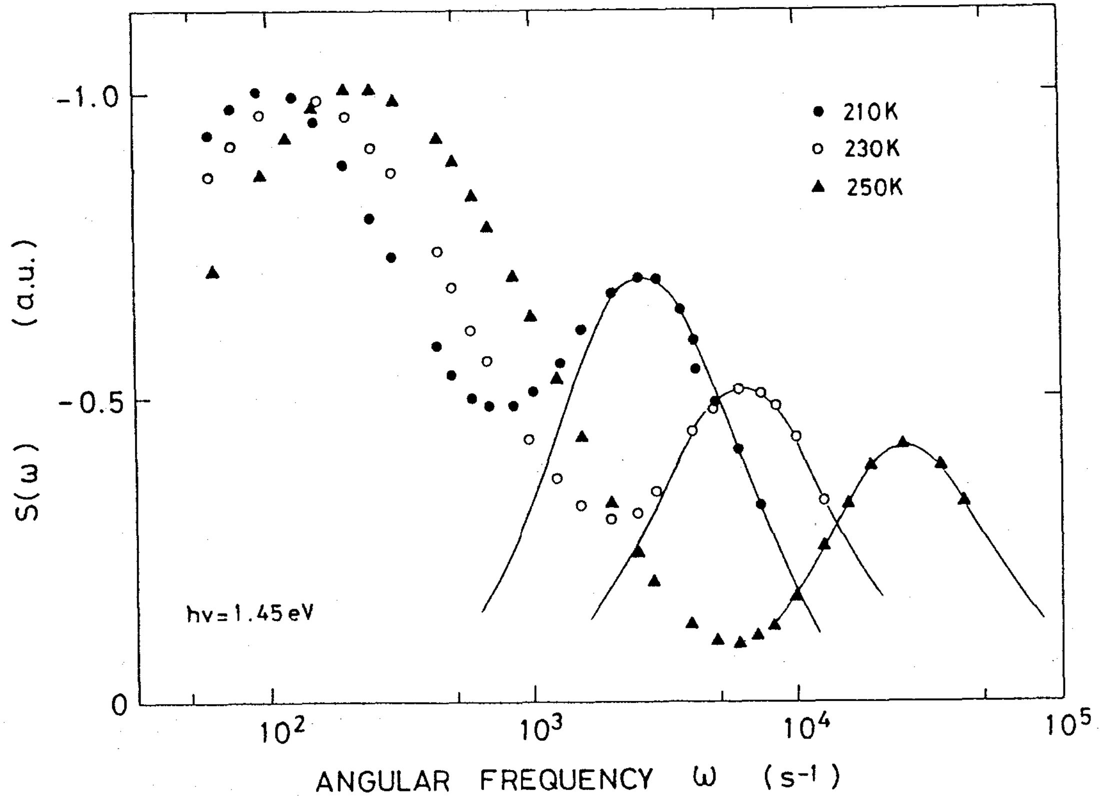

Fig. 2-7. MPCS spectra S(ω) measured on an a-Si:H p-i-n junction at moderately low temperatures. Gap states located deeper than around 0.31eV are populated with non-equilibrium electrons by subband-gap light of energy 1.45eV. The spectra display a broad structure associated with D^- states in the lower modulation frequency region, and a sharp signal characterized by the MPCS line-shape function (solid lines) in the higher modulation region, the corresponding energy depth of which is estimated to be about 0.4eV from the conduction band edge. The MPCS spectra are normalized with the peak magnitudes of the D^- related structure.

centre. Little is known about whether or not the D^- centre has unrelaxed states in the gap; however, the existence of such unrelaxed states is suggested by Street[17]. If the assignment is true, then the E1 states would play an important role in determining carrier transition processes through DB centres, which would be reflected in the temperature dependence of the prefactor of the thermal emission rate of electrons from D^- centres; that is, the attempt-to-escape frequency ν_n introduced in section 2-2-1. This is actually found, and will be discussed in the section 2-3-2.

2-3-2. Attempt-to-escape frequency

Figure 2-8 shows the relationship between the modulation frequency ω_{peak} at the peak

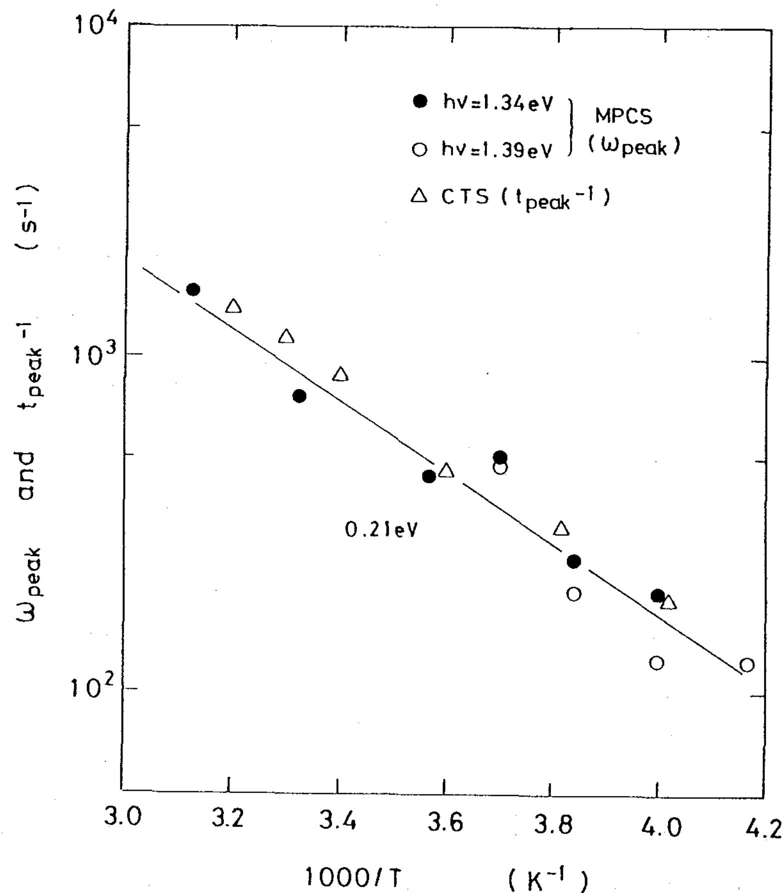

Fig. 2-8. Peak frequency ω_{peak} of the MPCS spectrum associated with the D^- states and inverse time t_{peak}^{-1} of the peak in the CTS spectrum plotted against reciprocal temperature. The slope of the plot gives an activation energy 0.21eV.

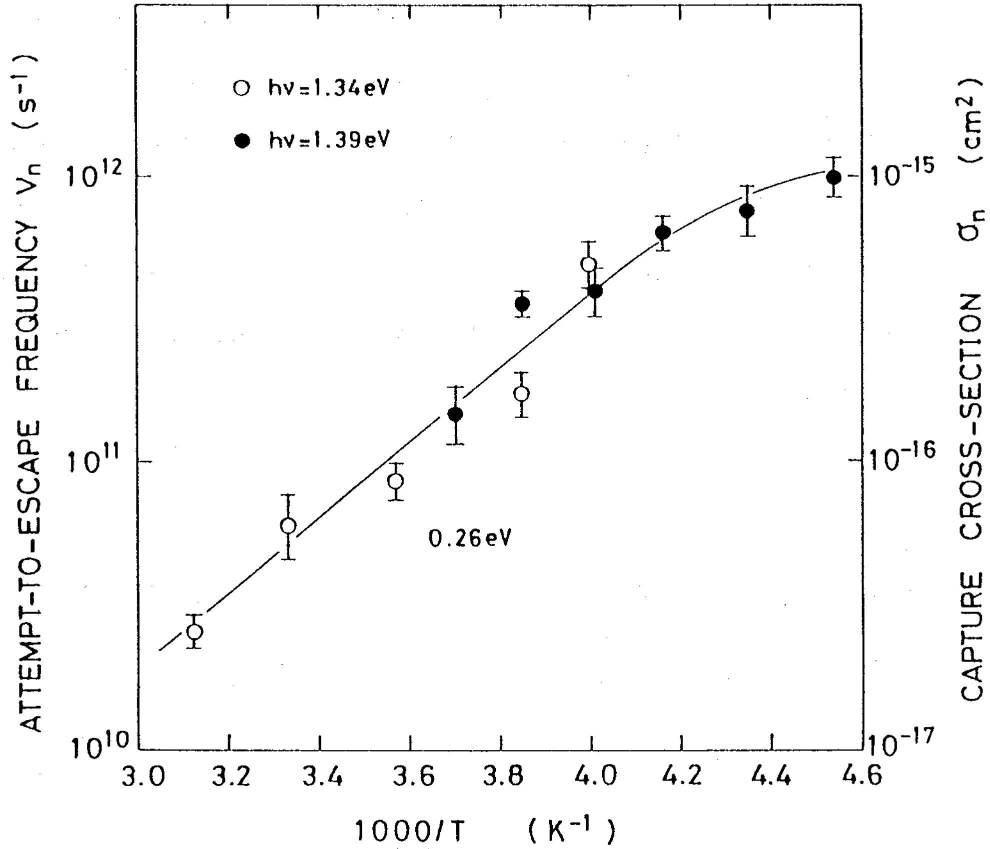

Fig. 2-9. Temperature dependence of the attempt-to-escape frequency ν_n as well as the electron capture cross-section σ_n determined from the peak modulation frequency ω_c of the function $S(\omega)\omega$ according to eqn. (2-13). The negative activation energy 0.26eV is the slope of the raw data without correction for the temperature-shift of the band gap.

position of the MPCS spectrum plotted against reciprocal temperature. For comparison, the time constant t_{peak} which corresponds to the peak position of the CTS (current transient spectroscopy) spectrum [18] measured upon the same sample is also plotted as open triangles. The quantity t_{peak}^{-1} clearly stands for the emission rate of an electron from the peak of the D^- distribution. A quantitative agreement of ω_{peak} and t_{peak}^{-1} then confirms that the MPCS signal really originates from the thermal emission process, and thereby assures us of the plausibility of the analysis for the MPCS signal presented in section 2-2-1.

If the attempt-to-escape frequency ν_n is independent of temperature, the activation energy determined from the slope of the Arrhenius plot in Fig.2-8 gives the peak energy of the D^-

centre. As indicated in the figure, however, the activation energy is about 0.21eV, which is substantially smaller than the peak energy of the D^- centre already settled in fig.2-6. This suggests a strong temperature dependence of the attempt-to-escape frequency ν_n. The magnitude of ν_n is estimated through eqn.(2-13) by using the characteristic frequency ω_c at which the function $S(\omega)\omega$ attains its maximum. Figure 2-9 presents the temperature dependence of ν_n evaluated by assuming a temperature-independent band gap equal to 1.76eV. It is found that at high temperatures ($T \geq 230K$) ν_n increases with decreasing temperature as

$$\nu_n = \nu_{n\infty} \exp(\varepsilon_v / kT) , \qquad (2\text{-}15)$$

where $\nu_{n\infty} = 2\times10^6 s^{-1}$ and ε_v=0.26eV, and then tends to approach a saturated value around $10^{12}s^{-1}$ for $T \leq 230K$.

Since the measurement of ν_n is made over a wide temperature range, the temperature dependence of the energy band gap ε_g may have some influence on that of ν_n, as is easily imagined from eqn.(2-13). Figure 2-10 presents the temperature dependence of ν_n, evaluated by assuming the temperature-shift coefficient of the band gap to be 4.4×10^{-4} eVK^{-1} [19]. It is found in this figure that the raw values of the activation energy ε_v as well as the prefactor $\nu_{n\infty}$ can be corrected to ε_v=0.39eV and $\nu_{n\infty}=1.3\times10^4$ s^{-1}, while the saturated value of ν_n in the low-temperature region becomes around $4.6\times10^{12}s^{-1}$. The peak energy of the D^- centre is basically evaluated from the activation energy stands for that extrapolated to zero temperature, the energy depth 0.6eV may not contradict the room-temperature value of 0.47eV. This, in turn, implies that the depth of the D^- centre from ε_c follows the temperature-shift of the band gap, about 0.13eV for $0 \leq T \leq 300K$.

The attempt-to-escape frequency ν_n may be related to the capture cross-section σ_n by the relation $\sigma_n = \nu_n / N_c \upsilon$, where N_c denotes the effective density of states in the conduction band and υ the thermal velocity. Since $N_c \upsilon$ has a weak temperature dependence like T^2, the result in Fig.2-10 indicates that the capture cross-section σ_n also has a temperature dependence exp(0.39eV/kT), which decreases with increasing temperature. Street[20] observed such unusual

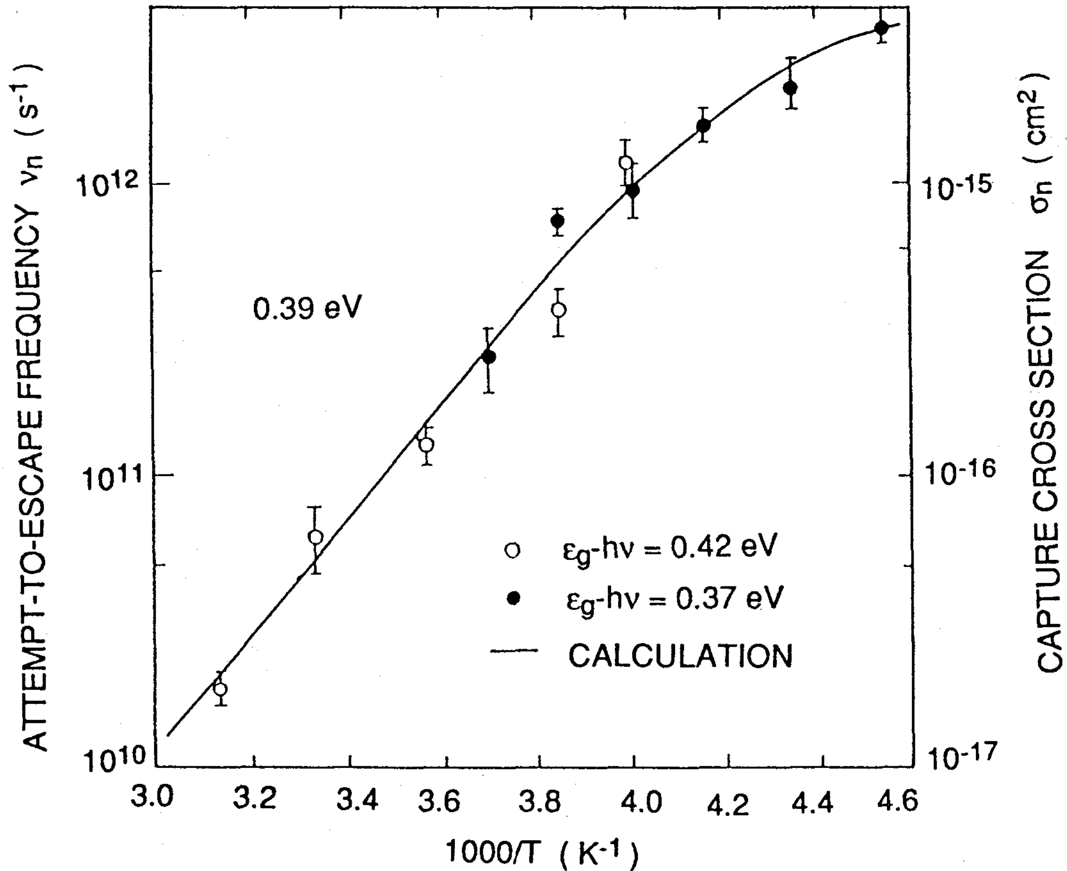

Fig. 2-10. Temperature dependence of v_n evaluated by assuming the temperature-shift coefficient of the band gap to be $4.4x10^{-4}$ eVK^{-1}. The negative activation energy 0.39eV is the slope of the data with correction for the temperature-shift of the band gap.

behavior in undoped a-Si:H, although the temperature dependence was much weaker ($\propto T^{-1.5}$), and Street interpreted it in terms of a capture process involving tunneling through tail states near the DB centres. More detailed work, however, revealed that the tunneling capture does operate for electron capture by positively charge D^+ centres, but not for electron capture by neutral D^0 centre [21]. On this basis, Spear et al. claimed that some of the DB should be in the D^+ state in Xerox undoped a-Si:H. This explanation seems to be applied to our case, since some of the DB centres should be in the D^+ state in a fraction of the i region of the junction. It is noted, however, that the observed MPCS signal is located about 0.5eV below ε_c, which is too shallow [22] to be

assigned to the D^0 centre, converted from D^+ by optical excitation. Therefore, it is unlikely that the unusual behavior of ν_n observed in Fig.2-10 is attributable to the contribution of D^+ centres.

A possible explanation may be then to consider that electron emission from the D^- centres takes place by a two-step process via an unrelaxed state [23] which has a sharp distribution in the gap and is strongly coupled with the lattice. In this case, the jump to the unrelaxed state is followed by either emission into the conduction band or recapture into the ground state. At high temperatures, when thermalization from the unrelaxed state is more likely than a transition into the ground state of the D^- centre, the net rate for electron emission from the ground state is governed by the jump rate to the unrelaxed state, and thus the observed attempt-to-escape frequency ν_n is expressed by [23]

$$\nu_n = R \cdot \exp(\varepsilon_d^* / kT) , \qquad (2\text{-}16)$$

where R denotes the transition rate from the unrelaxed state located at an energy ε_d^* below ε_c to the ground state. On the other hand, in the low-temperature limit where electron emission from the unrelaxed state into the conduction band becomes a rate-limiting process, ν_n is directly related to the attempt-to-escape frequency ν_n^* of the unrelaxed state. If R represents an activated multiphonon process with an activation energy ε_a, eqn.(2-16) suggests that ν_n behaves as $\exp[(-\varepsilon_a+\varepsilon_d^*)/kT]$ at high temperatures. Then, if $\varepsilon_d^*>\varepsilon_a$, the high-temperature portion of the plot of $\ln\nu_n$ against 1/T may have a positive slope, while at low temperatures ν_n tends to exhibit a weaker temperature dependence. These behaviors based on the two-step capture process are consistent with our experimental data in fig.2-10. By equating eqn.(2-15) and (2-16), the energy depth of the unrelaxed state ε_d^* and the pre-exponential factor R_0 of the transition rate R are related to the activation energy ε_v and the prefactor $\nu_{n\infty}$ of the observed attempt-to-escape frequency ν_n as

$$\varepsilon_d^* = \varepsilon_v + \varepsilon_a \cong 0.39\text{eV} + \varepsilon_a \qquad (2\text{-}17)$$

$$R_0 = \nu_{n\infty} \cong 1.3 \times 10^4 s^{-1} . \quad (2\text{-}18)$$

The energy depth given in eqn.(2-17) stands for that extrapolated to zero temperature, while the estimate of R_0 involves an uncertainty of a factor at most 10^2 due to the probable temperature dependence of ε_d^*. Moreover, the attempt-to-escape frequency ν_n^* of the unrelaxed state is estimated from the saturated value of the observed ν_n in the lower temperature region; $\nu_n^* \cong 4.6 \times 10^{12} s^{-1}$.

As demonstrated in the former section, MPCS reveals the present of an electron state (E1) shallower by about 0.2eV than the D^- states. We tentatively assign it as the unrelaxed state of the D^- centre. We can offer some evidence, although it is somewhat circumstantial, for this assignment. The first point is concerned with the identical values of the attempt-to-escape frequency independently eatimated for both states; $\nu_{E1} = 3 \times 10^{12} s^{-1}$ and $\nu_n^* = 4.6 \times 10^{12} s^{-1}$. The two-stage transition model, introduced in this section, assumes a sharp distribution for the unrelaxed state, otherwise the MPCS loses its spectroscopic nature since the DB distribution obtained by this method should reflect that with respect to the unrelaxed state. Actually, the E1 states have a very sharp distribution with width much less than 1.76kT. Moreover, if the activation energy ε_a for the transition R from the unrelaxed state to ground state is neglected, the energy depth of the unrelaxed state ε_d^* at zero temperature is estimated from eqn.(2-17) to be about 0.39eV, which satisfactorily coincides with that of the E1 state, $\varepsilon_{E1} = 0.4 eV \pm 10\%$. The negligible activation energy, then, implies that the transition involves either a tunneling process between vibronic level [24] or a radiative process [23].

Finally, it should be noted that for P-doped a-Si:H, Okushi et al. reported a very small capture cross-section in the range of 10^{-18} to 10^{-19} cm^2 [25], which has a weak temperature dependence, consistent with a multiphonon emission process with weak coupling. The peak of their ICTS spectrum appears in the time range 0.1-1.0 s at room temperature, so that the peak of the D^- centre is placed at about 0.5eV below ε_c. This energy placement is compatible with our present result for undoped a-Si:H, although the specified capture cross-section deviates by more than three orders of magnitude in each experiment. Then, the question arises why the DB centre

possesses a different capture cross-section in undoped and P-doped a-Si:H. This may be understood if we accept that a different capture process operates in both materials; that is, electrons are captured directly into neutral DB centres without involving the two-step capture via unrelaxed states. This difference is likely to be attributed to the nature of the unrelaxed states of the DB centre in undoped and P-doped materials. It is then clear that more extensive work is needed to identify the microscopic structure and nature of the unrelaxed states.

2-3-3. Substrate temperature dependence of deep states

Typical MPCS signals taken on undoped a-Si:H deposited at the substrate temperature T_s=300°C and 150°C by conventional plasma CVD are shown in Figs.2-11 and 2-12.[26] The

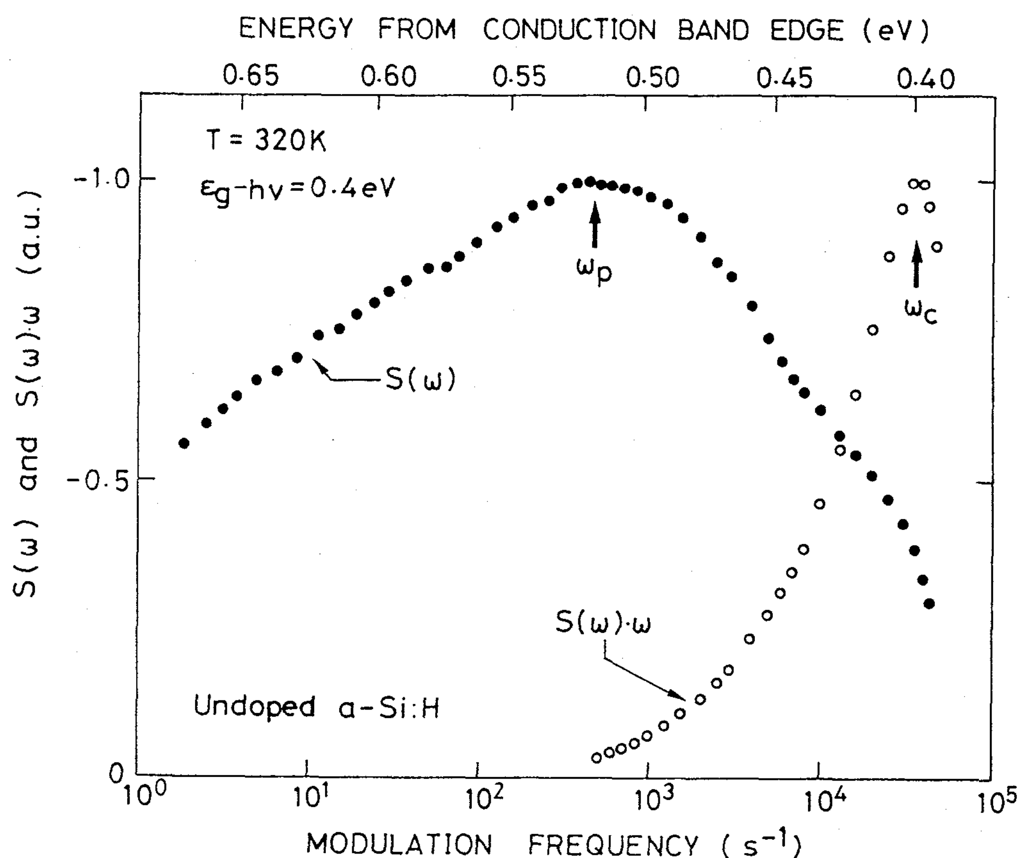

Fig. 2-11. MPCS spectrum of undoped a-Si:H prepared at 300°C by conventional plasma CVD. The signal is assigned as due to doubly occupied dangling bond centre (D^-).

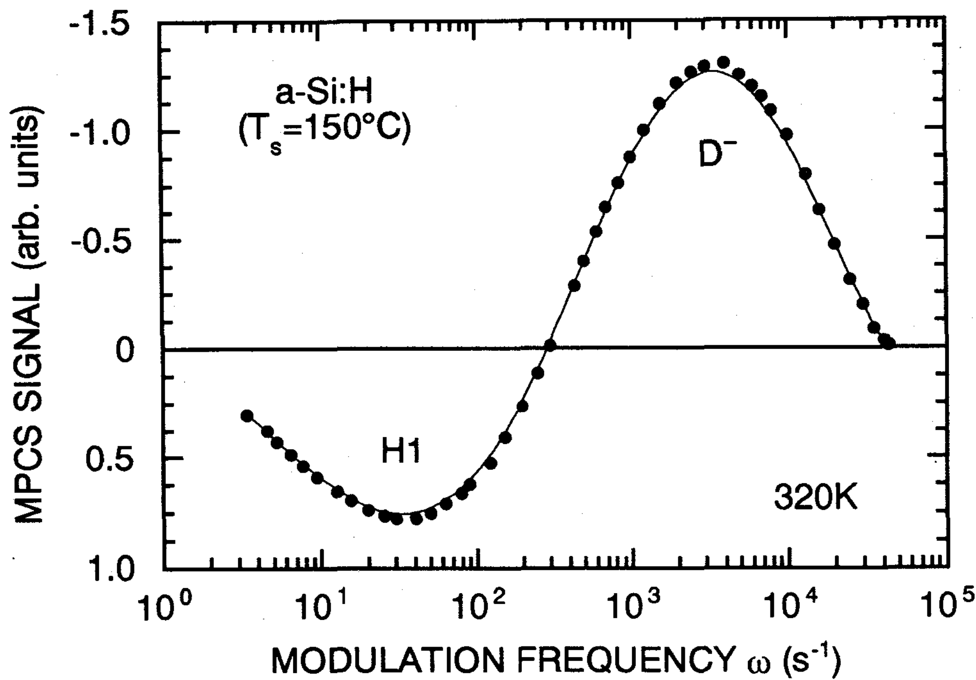

Fig. 2-12. MPCS spectrum of undoped a-Si:H prepared at 150°C. A hole emission signal (H1) is superposed to D^- signal.

MPCS spectrum for T_S=300°C sample exhibits a single broad peak of a negative sign, indicating that the signal arises from an electron trap. The $S(\omega)\omega$ function peak at $\omega_c=3.5\times10^4 s^{-1}$, which corresponds to the energy depth ε_g-hν=0.4eV from the conduction band edge. Utilizing the settled ω_c in eqn.(2-12), the modulation frequency ω is converted to the energy scale, as indicated at the upper horizontal axis. The energy depth of the deep centre is read as about 0.52eV, and the attempt-to-escape frequency $\nu_n=7\times10^{10}s^{-1}$ at 320K. We here tentatively assign this electron state as due to the doubly occupied dangling bond centre (D^-).

For the sample prepared at T_s=150°C, the MPCS signal exhibits two features of opposite signs. This indicates that a hole emission signal is superposed to an electron emission signal due to the D^- centre which dominates the MPCS spectrum in the T_s=300°C sample. An alternative way to determine the energy depth with relying on the excitation photon energy hν is to measure the magnitude of $S(\omega_{peak})$ with varying hν. Since only the states located deeper than ε_g-hν are populated with the subband-gap excitation and can contribute to the MPCS signal, the value of

ε_g-hν at which a sudden decrease in the MPCS signal $S(\omega_{peak})$ occurs may identify the energy depth of the hole trap. Figure 2-13 demonstrates how the magnitude of $S(\omega_{peak})$ varies with the ε_g-hν. It is found that $S(\omega_{peak})$ exhibits an abrupt decrease at a particular value of ε_g-hν, providing an estimate of the energy depth of the hole trap measured from the valence band edge ε_v. Detailed analysis using various different photoexcitation energies reveals that the hole trap centre, named here H1 centre, is located about 0.54±0.03eV above the valence band edge ε_v, and possesses the attempt-to-escape frequency ν_n of about $9\times10^{10}s^{-1}$ at 300K.

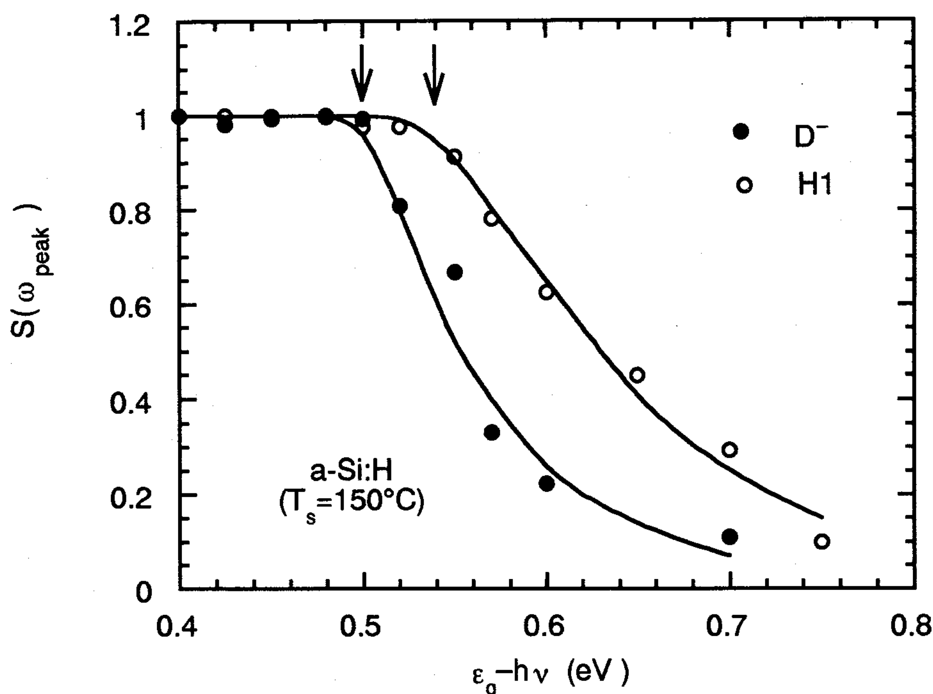

Fig. 2-13. Peak magnitude $S(\omega_{peak})$ of MPCS spectra of D^- and H1 centres plotted against ε_g-hν for undoped a-Si:H prepared at 150°C. The arrows indicate ε_g-hν at which a sharp reduction of the signal takes place, that is the peak energy of the D^- and H1 centres distribution measured from the conduction and valence band edges, respectively.

Figure 2-14 shows the MPCS spectra for undoped a-Si:H prepared at various substrate temperatures. A computer simulation taking into account of the competing contributions from the D^- and H1 centres yields a good fit to the net MPCS spectrum, as shown by the solid line in Fig.2-15. The density of the D^- and H1 centres have been evaluated by integrating the

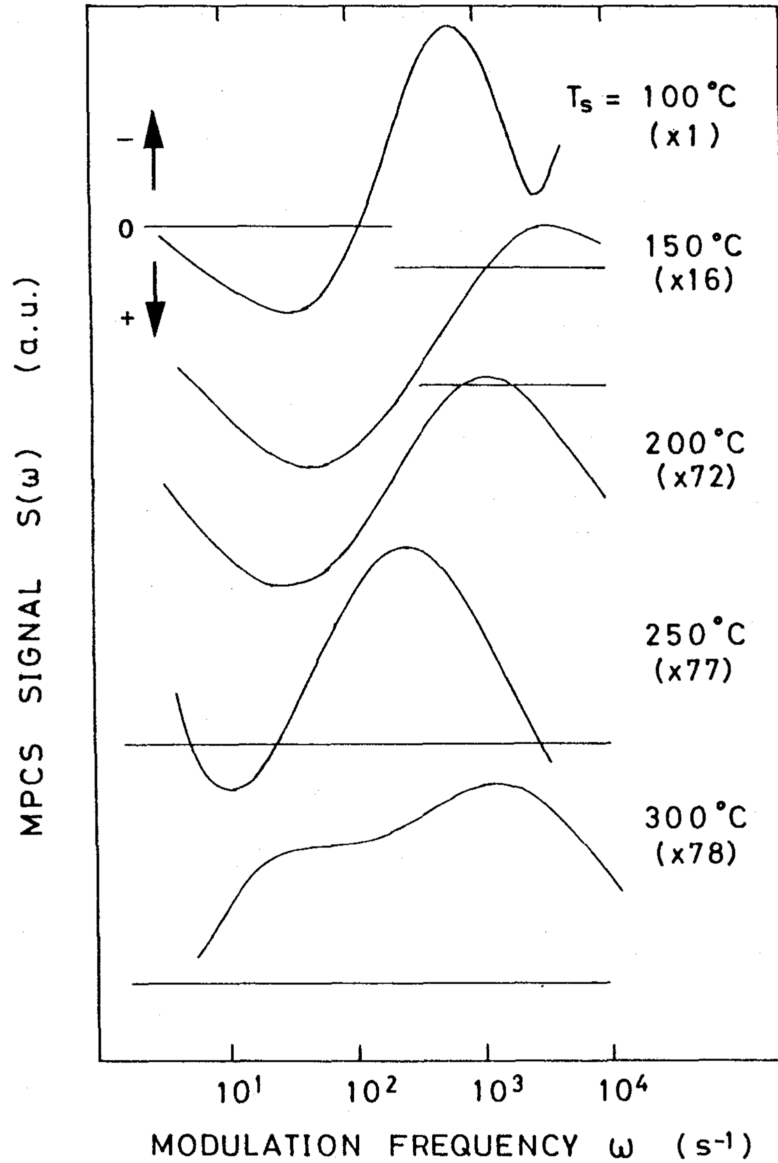

Fig. 2-14. MPCS spectra for the samples prepared at various substrate temperature.

deconvoluted MPCS spectra for the samples prepared at various substrate temperatures. The result is shown in Fig.2-16, where the density scale is given by the density N multiplied by the relevant optical cross section σ_{opt} since σ_{opt} is not definitely known for each centre. The density of the D^- centre takes minimum at around T_S=200°C, while that of the H1 centre monotonically decreases with raising T_s. As indicated in the inset, a good linear relation holds between the

density of the D$^-$ centre and the dangling bond spin density at g=2.0055, confirming that the negative MPCS signal, here assigned as due to the D$^-$ centre, is really associated with dangling bond centre. The origin of the H1 centre has not been yet identified, however, one possibility may be dangling bond defects spatially coupled with each other [27)] or with residual impurities [28)], which are characterized by a negative correlation energy.

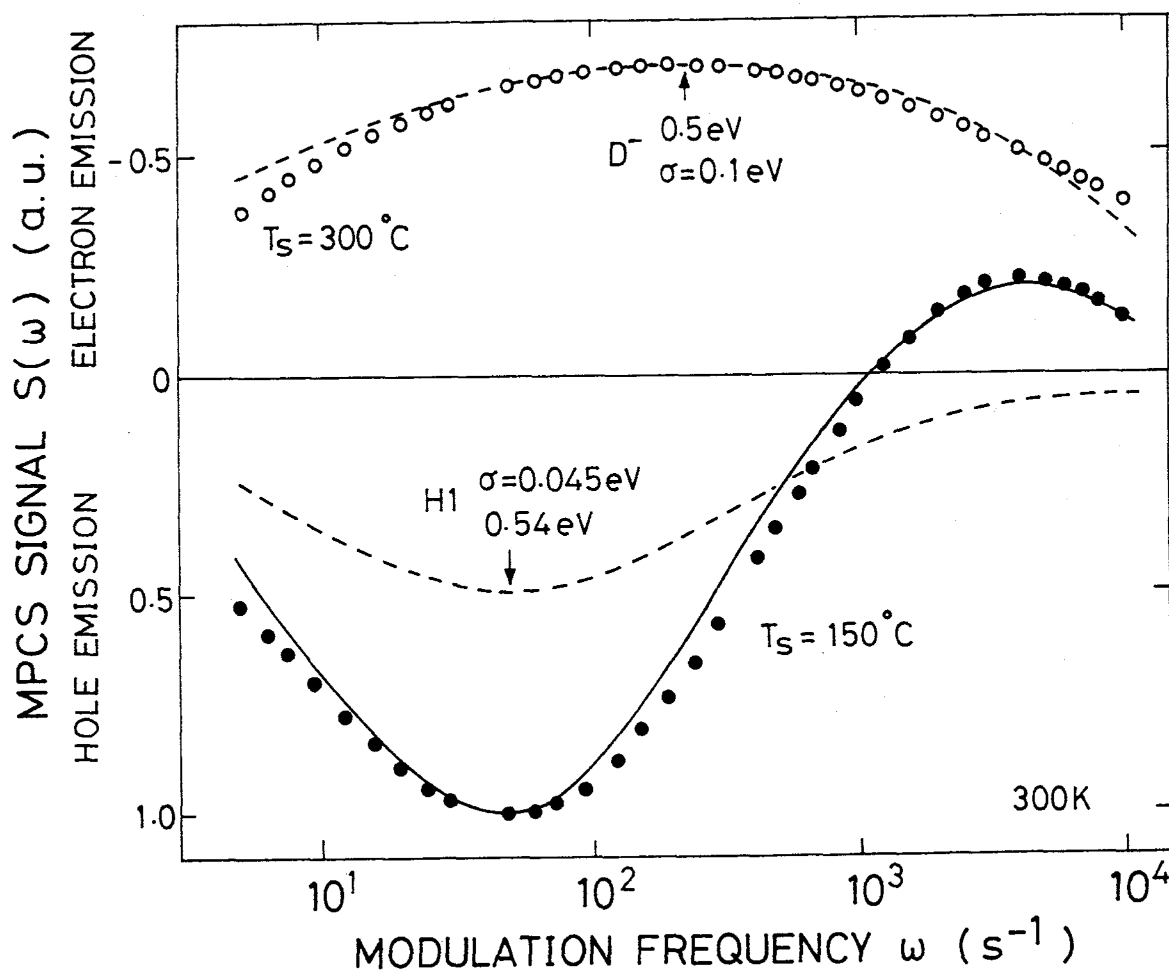

Fig. 2-15. MPCS spectrum of undoped a-Si:H prepared at 150°C. A hole emission signal (H1) is superposed to D$^-$ signal. Solid line indicates theoretical fit to the experimental data.

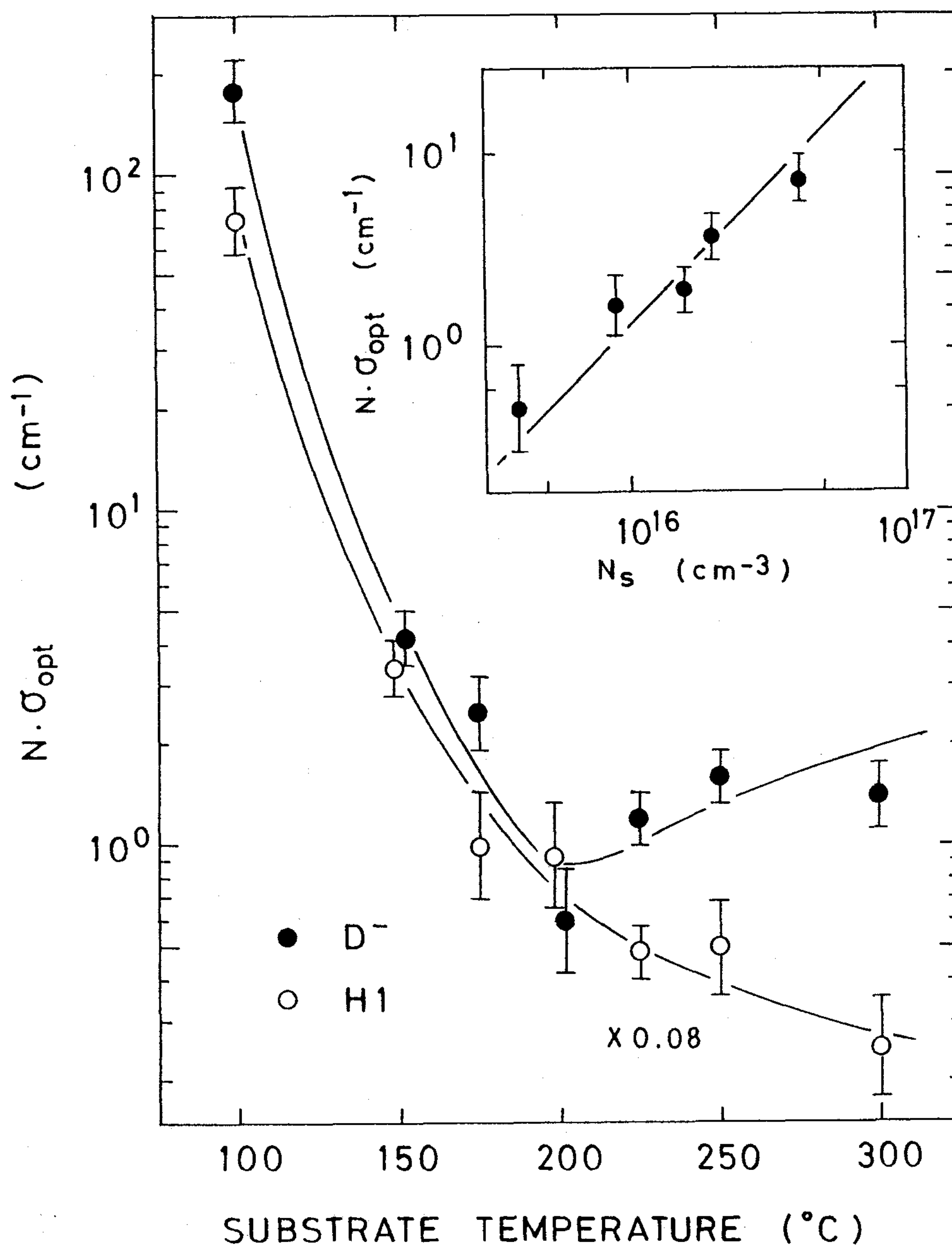

Fig. 2-16. Substrate temperature dependence of D^- and H1 centres. The inset compares D^- centre density with ESR dangling bond spin density.

2-3-4. Light-induced changes

As described in previous section, the modulated photocurrent spectroscopy (MPCS), has revealed two pronounced features in the gap states distribution of undoped a-Si:H, one of which is assigned as due to the doubly occupied dangling bond (D^-) located at about 0.5eV below the conduction band edge. The energy position another deep-lying states (H1 centre) is found to be about 0.54eV above valence band edge, although the origin is not yet identified. We have carried out a systematic investigation on the change in these two deep-lying states upon light-soaking and single carrier injection. In this section, the author presents the experimental results as well as discuss their implications for the role of two kinds of deep-lying centres played in the light-induced phenomena of undoped a-Si:H.

Samples employed in the work were p-i-n junction photocells prepared by conventional plasma CVD with two different substrate temperatures; 150°C and 300°C. The light-induced changes of the MPCS spectrum are shown in Fig.2-17(a) and (b) as a function of the light exposure time for undoped a-Si:H prepared at 300°C and 150°C, respectively. For the light soaking, He-Ne laser (6328Å, 10^{17} photons/scm^2) was used. It is found that upon the short light soaking a dip of a positive sign appears around $\omega=50s^{-1}$ for T_s=300°C sample. The dip progressively grows up with exposure. So far as the MPCS spectra shape is concerned, a similar but less-pronounced change is observed for the sample prepared at T_s=150°C.

The density of the D^- and H1 centres have been evaluated by integrated deconvoluted MPCS spectra for the sample with various light exposure times. The result is shown in Fig.2-18, where the density scale is given by the density N multiplied by the relevant optical cross section σ_{opt} since σ_{opt} is not definitely known each centre. This figure shows that for T_s=300°C sample, in which the equilibrium density of D^- centre is lager than that of H1 centres increase monotonously with exposure time, approximately obeying a 1/3-power law.

On the other hand, T_s=150°C sample, the increase in the D^- density is more extensive than the H1 density in short light exposure times. The different behavior of light-induced change suggests the process of defect conversion from the H1 to D^- centres may operate in addition to the defect creation process.

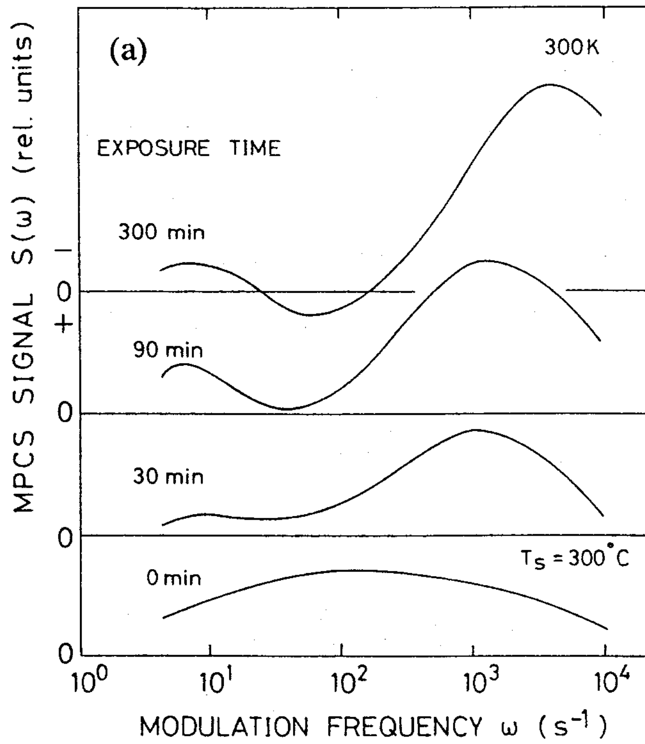

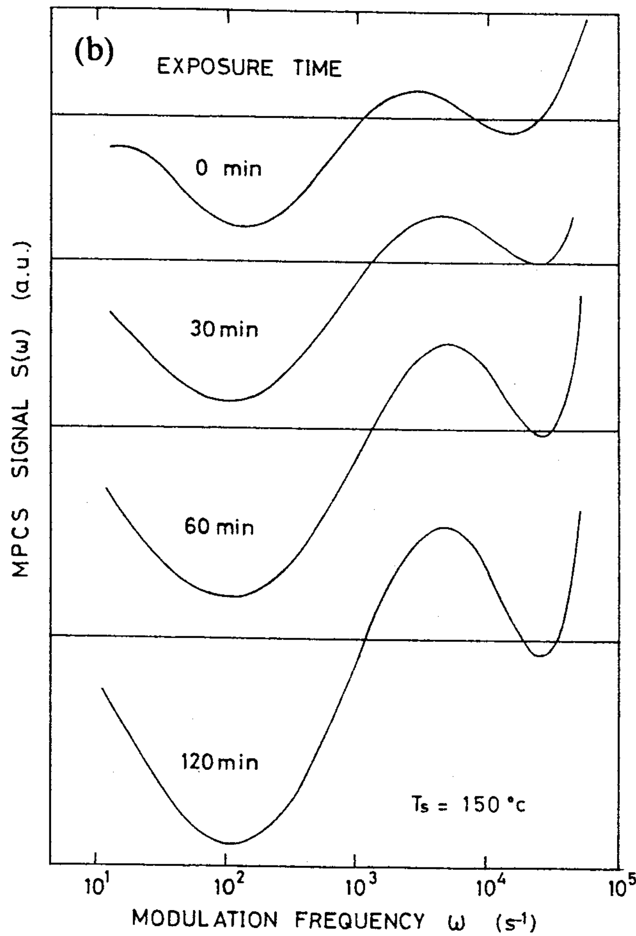

Fig. 2-17. Light-induced changes in the MPCS signals for undoped a-Si:H prepared at (a) T_s=300°C and (b) T_s=150°C, respectively. It is found clearly that the MPCS signal associated with D^- and H1 centres both increase, which indicates a negative and positive sign, respectively.

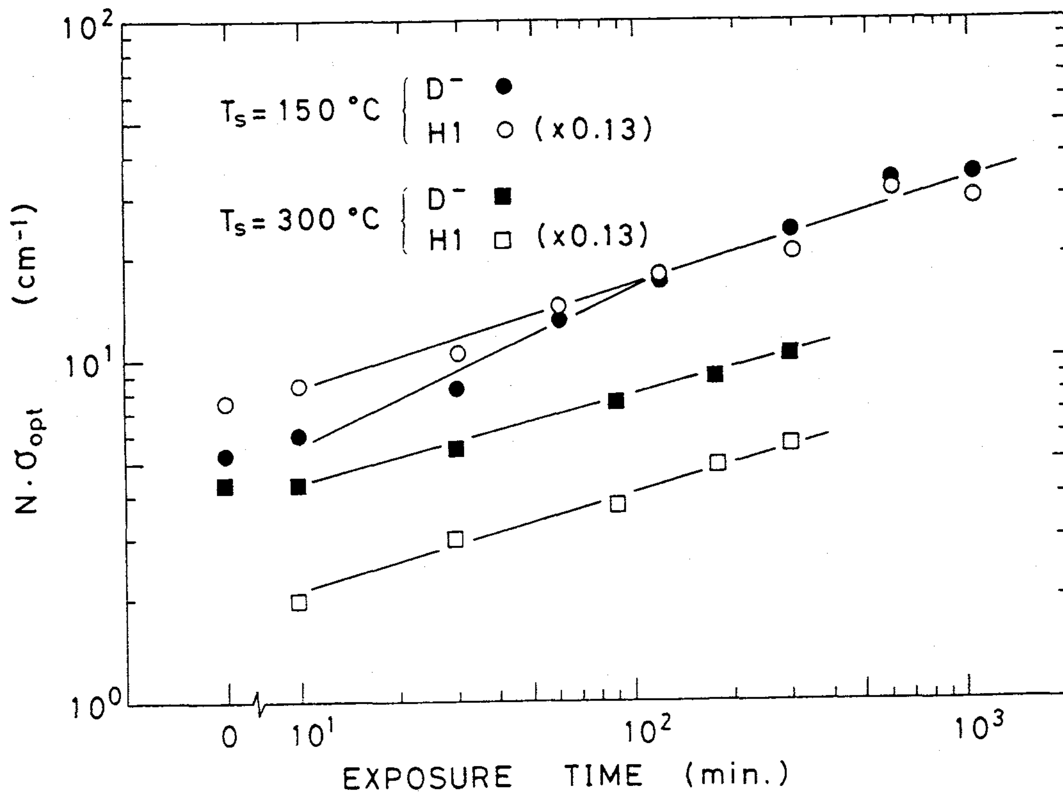

Fig. 2-18. Density of D⁻ and H1 centres as a function of light exposure time.

Change induced by single carrier injection (blue-light illumination on either p- or n- layer) have been also examined on the same sample employed in light-soaking experiments. For single carrier injection, the blue light from the filtered Xe lamp (4000Å, 10^{18} photons/scm^2) was used. The results are summarized in Fig.2-19, where the relative changes in the centre densities before and after the treatments (light-soaking or single carrier injection) are plotted. It is found clearly that the density of both D⁻ and H1 centres exhibits a definite increase differs from each other depending on the original condition of the material and mode of treatments. A more extended increase in the D⁻ centre is observed for H1 centre in their initial states, particularly when being subject to pure hole injection.

The results lead us to a conclusion that the presence of non-equilibrium carriers itself is responsible for the creation of metastable defect centres although carrier recombination may further enhance the creation probability. The bond breaking model associated with Si-Si weak-

bonds is likely to apply to interpret the " carrier-induced defect creation" phenomenon [29]. On the other hand, the different behaviors of the increases in the defect densities found in Fig.2-19 suggests that another process may be also operative in addition to the defect creation process [27][28][30]; that is, "defect conversion" from the H1 to D centres, which is triggered through carrier capture, specifically hole capture. This model can qualitatively explain why the increase in the D centre is more pronounced as compared with that of the H1 centre for the sample prepared at lower temperature, particularly when being subject to pure hole injection. Namely, the H1 centre works as an optional source for the metastable D centres which dominate carrier recombination. It is then clear that further investigation is needed to understand the origin of the H1 centre and the microscopic mechanism of defect inter-conversion process in order to establish a technology for producing highly-stable a-Si:H solar cells.

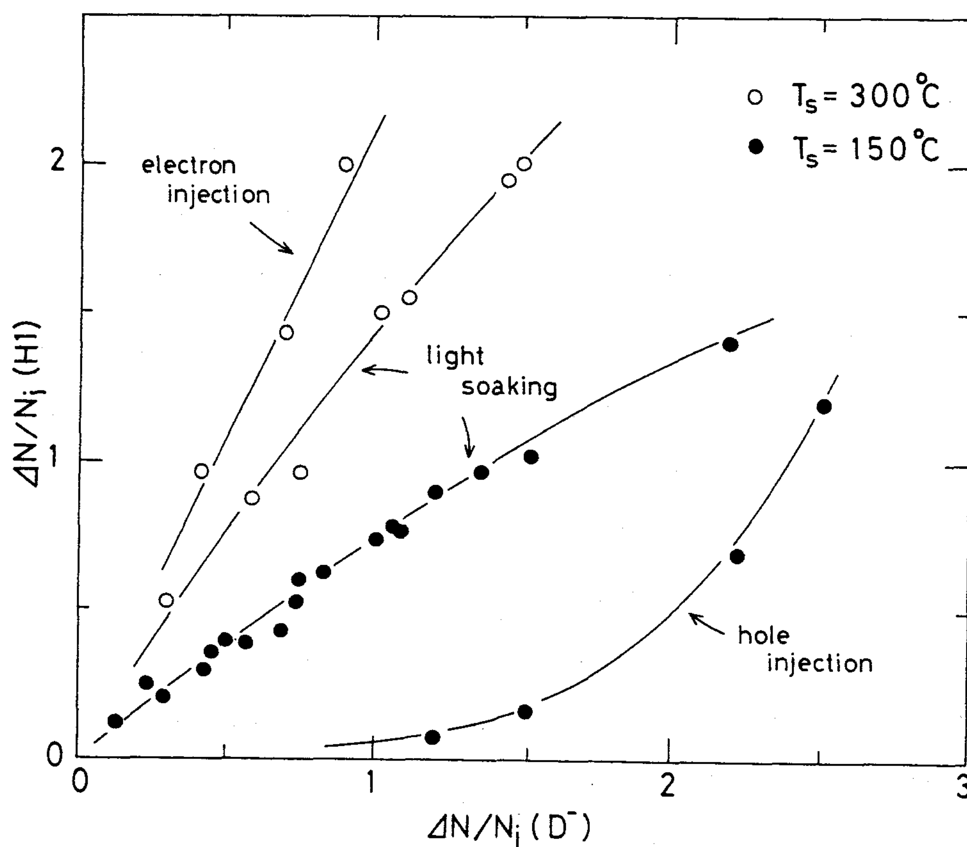

Fig. 2-19. Light and carrier induced changes in H1 and D^- centre densities on undoped a-Si:H prepared at two different temperatures.

2-4. Deep localized states in undoped a-SiGe:H

Extensive studies have been focused on hydrogenated amorphous silicon (a-Si:H), and a pool of experimental data has accumulated so as to allow us to discuss in detail the deep localized states, especially those created by a dangling bond. In contrast, little is known about them in amorphous silicon-germanium (a-SiGe:H) alloys which are the leading candidates for the low band-gap material used in a-Si-based solar cells. The development of a-SiGe:H alloys possessing an electronic quality comparable to a-Si:H is one of the key issues for the realization of high efficiency solar cells. It is clear that the development must be accompanied by a better understanding of deep localized states. In this work, we have carried out a systematic study on the deep localized states in a-SiGe:H alloys of the bandgaps ranging from 1.16eV to 1.68eV, with particular emphasis on those associated with doubly occupied dangling bond (D^-), using modulated photocurrent spectroscopy (MPCS)[3][4].

In this section, the author presents the result of experiments on a-SiGe:H alloys with bandgaps between 1.16eV to 1.8eV (a-Si:H) measured by means of the MPCS. It is shown that the energy of the doubly occupied dangling-bond centres exhibits a systematic shift with the bandgap energy, while the density of the dangling-bond centre gradually increases on decreasing the bandgap. On the basis of experimental data, the author discusses the identity of the dangling bonds in association with carrier transition process through the Si and Ge dangling-bond centres.

2-4-1. Density and distribution of deep states

Figure 2-20 shows the MPCS spectra $S(\omega)$ measured for several samples with different bandgaps. Since our main concern in this section is the evaluation of the state density from the MPCS signal, the excitation photon energy $h\nu$ was carefully chosen for each sample so as to saturate the signal intensity. The γ value could not be exactly evaluated except for a-Si:H with the bandgap 1.8eV and 1.77eV [6], because for a-SiGe:H the lower- frequency part of the main MPCS signal shown in this figure often overlaps with less-pronounced signals of a different sign. The presence of signals of different signs, however, implies that the γ value is at least

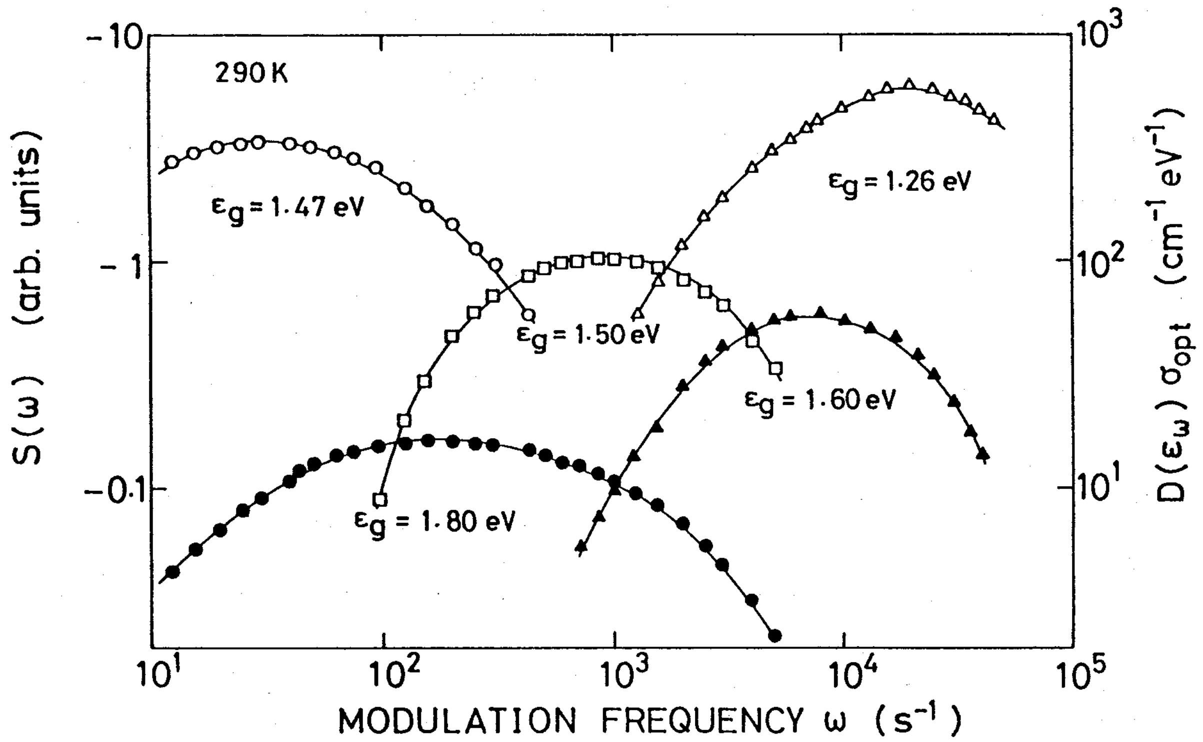

Fig. 2-20. MPCS spectra $S(\omega)$ measured for a-SiGe:H alloys at 290K with various bandgap energies. The vertical axis at right-hand side is scaled to the state density multiplied by the optical cross section, $D(\varepsilon_\omega)\sigma_{opt}$, according to eqn. (2-9) in the text.

greater than 0.5, so that the sign of $S(\omega)$ identifies whether the observed MPCS signal represents electron emission or hole emission. The negative sign of $S(\omega)$ then indicates that the signal in this figure arises from electron emission associated with a certain deep centre of electron-trap nature.

The vertical axis of Fig.2-20 on the right-hand side is scaled to the density of states multiplied by the optical cross section $D(\varepsilon_\omega)\sigma_{opt}$ which is determined from $-S(\omega)\alpha_{ag}/kT(\gamma+1/2)$ as suggested by eqn. (2-9). Since the γ value is not known for a-SiGe:H, we tentatively assumed that γ=0.75 for all the samples. The resulting error in the estimate $D(\varepsilon_\omega)\sigma_{opt}$ may amount to at most ±75%. Integrating the MPCS signals with respect to $kT\ln\omega$ provides the total density of

the deep centres. Figure 2-21 summarizes the total centre density N thus evaluated for a-SiGe:H alloys with various bandgaps ranging from 1.8eV for a-Si:H to 1.16eV. Note that the vertical axis is again scaled to N multiplied by σ_{opt} since the magnitude of σ_{opt} is not known. It is found that $N\sigma_{opt}$ increases by about two orders of magnitude as the bandgap is decreased from 1.8eV to 1.16eV. This trend agrees well with the results from constant-photocurrent measurements (CPM) [31] and the steady-state heterojunction-monitored capacitance method [32][33].

An insight into the origin of deep centres observed by the MPCS measurement may be

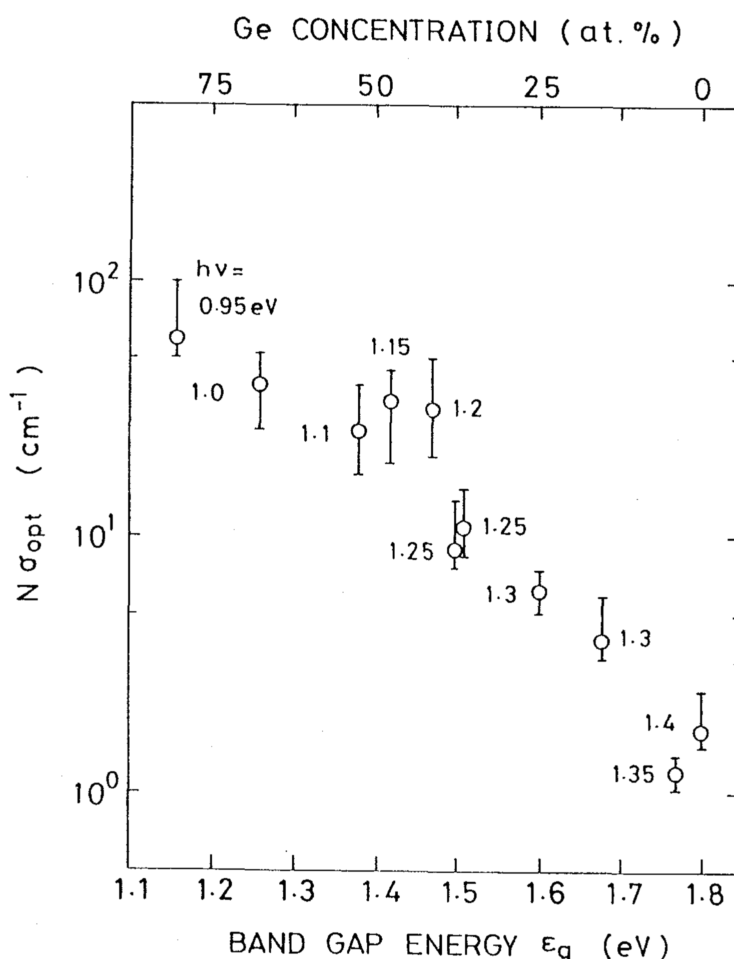

Fig. 2-21. Dependence of the integrated state density N on the bandgap energy. Since the magnitude of optical cross-section σ_{opt} is unknown, the scale on the vertical axis is given for $N\sigma_{opt}$. Numerals given at each data point indicate the excitation photon energy $h\nu$ used in the measurements.

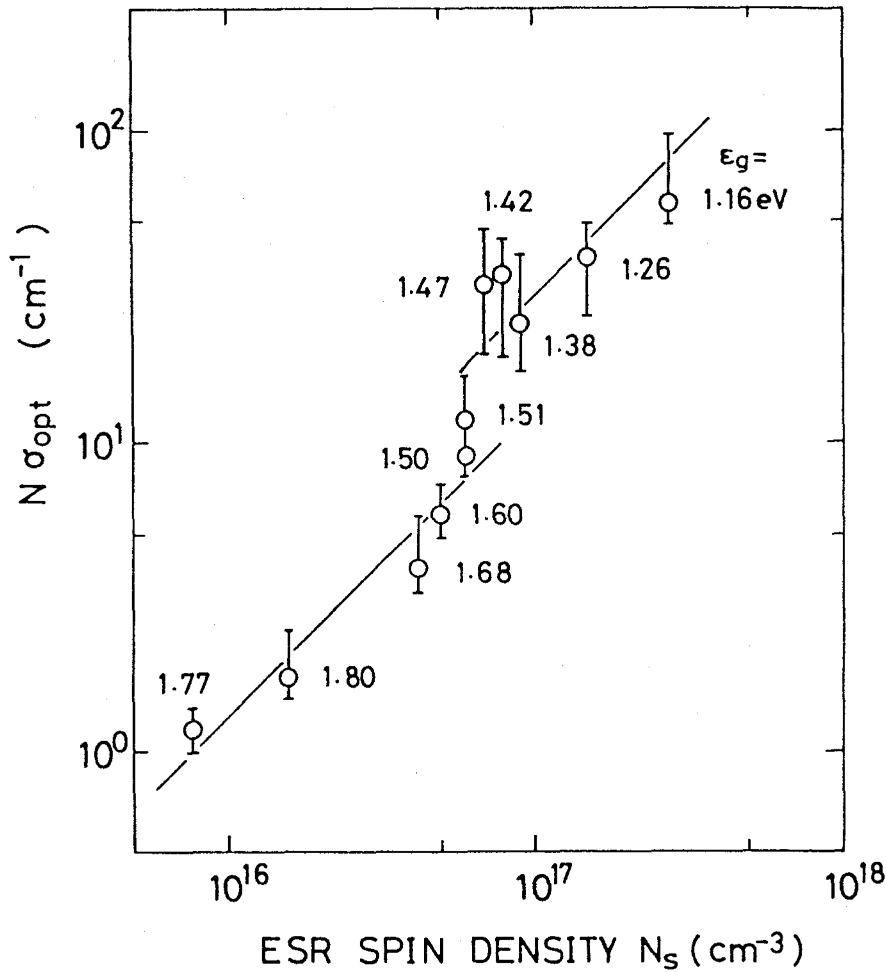

Fig. 2-22. Relation between the integrated state density N and ESR spin density N_s, which correspond to the dangling-bond density. The vertical axis is again scaled to $N\sigma_{opt}$.

provided by comparing the bandgap dependence of the density of deep centres with that of the unpaired spin density evaluated by electron spin resonance (ESR) measurements. The ESR measurements were carried out for thick a-SiGe:H films identical with those used in the MPCS measurement. As is well known, the ESR spectrum exhibits a convoluted signal of resonances from Si and Ge dangling bonds. Without deconvoluting the signal, we here use the total dangling-bond spin density determined by integrated ESR signal. Figure 2-22 compares $N\sigma_{opt}$ with the dangling-bond spin density N_s for a-SiGe:H alloys with bandgaps in the range from 1.8eV to 1.16eV. As found in this figure, good correlation holds between these two quantities, apart from

a discontinuity at the bandgap values around 1.5eV.

The dangling-bond spin density gives a measure of the density of singly occupied neutral dangling bonds, that is the D^0 centre. When an optical transition takes place from the valence band to a particular D^0 centre, the D^0 centre is converted to a doubly occupied dangling-bond D^- centre. The thermal emission of an electron from the D^- centre is detected as a MPCS signal with a negative sign. Thus, the deep centre observed in the present MPCS measurement is assigned as the D^- centre of either Si or Ge dangling bonds. It is suggested from the ESR measurements that, as the Ge concentration approaches about 20-40 at.%, which corresponds to the bandgap energies ranging from 1.64eV to 1.48eV in our case, a sharp switch of the predominant defect occurs from Si dangling bonds to Ge dangling bonds [34)35)]. The discontinuity found in the relation between $N\sigma_{opt}$ and N_s then seems to be attributed to this switch. It may be therefore permissible to assign the deep centre observed in the MPCS for the alloys with ε_g>1.5eV (group I) as originating from Si dangling bonds and that for ε_g<1.5eV (group II) from Ge dangling bonds. If the above assignations are correct, then the discontinuity in the linear relation between $N\sigma_{opt}$ and N_s found in the figure is attributed to the difference between the optical cross-section for Si and Ge dangling bonds, which are estimated to be about 1.3×10^{-16} cm^2 for Si dangling bonds and about 3.0×10^{-16} cm^2 for Ge dangling bonds.

Concerning the a-SiGe:H alloys with ε_g=1.5eV, which are situated in the transition region in Fig. 2-22, both types of dangling bond may coexist with roughly equal densities, so that the deep centre detected in our measurement is hardly identifiable as a Ge or Si dangling bond for such alloys. However, several pieces of evidence are provided in the following sections that the deep centre observed for a-SiGe:H alloys with ε_g=1.5eV arises from Si dangling bonds. This in turn implies that the MPCS signal associated with Ge dangling bonds is located outside the modulation frequency region covered in the present measurement.

Let us return to the MPCS spectra shown in fig. 2-20. As found in the figure, the modulation frequency ω_{peak} at which the peak of the MPCS signal occurs shows a nonmonotonic shift with the bandgap energy; that is it shifts towards the higher-modulation-frequency side as the bandgap is decreased from 1.8eV to 1.6eV, then jumps back to the lower-frequency side for

ε_g=1.47eV and again moves towards the higher-frequency side for ε_g=1.26eV. Since ω_{peak} is related to the peak position of the D^- centre, the observed shifts of ω_{peak} may be attributed to that of the energy depth of D^- centre as long as the attempt-to-escape frequencies do not differ appreciably for different materials.

2-4-2. Energy location of doubly occupied dangling-bond centre

Following the principle of MPCS spectroscopy, the energy depth of D^- centres from the conduction band edge is determined from the S(ω)ω spectrum. For example, Figure 2-23(a) shows MPCS spectra S(ω) measured for a-SiGe:H of 1.5eV bandgap at various temperatures ranging from 270K to 310K. The excitation photon energy is set at 1.2eV. As shown in this

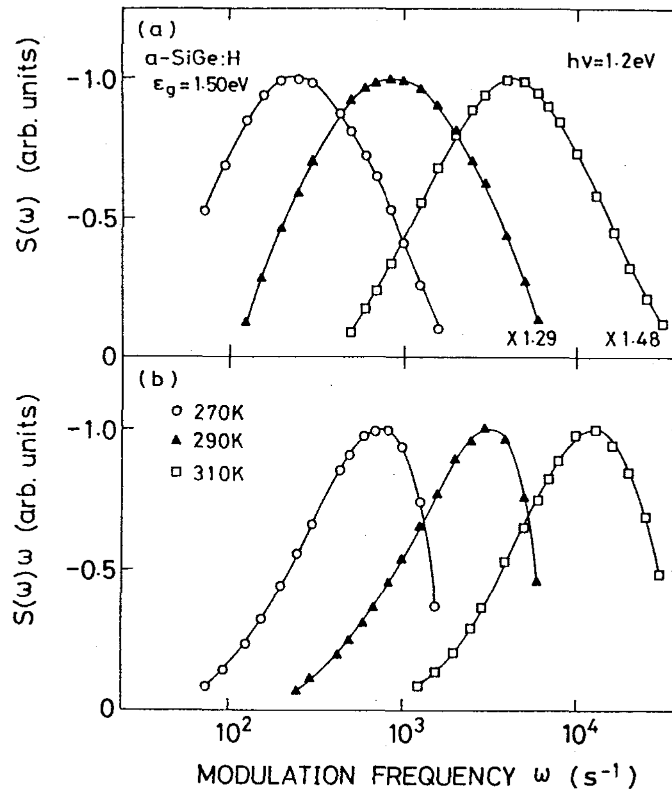

Fig. 2-23. (a) MPCS spectra S(ω) measured on an a-SiGe:H(ε_g=1.5eV; hν=1.2eV) Schottky barrier photocell at various temperatures . The frequency ω_c at the which the function S(ω)ω, shown in (b), attains its maximum corresponds to the energy depth 0.3eV from the conduction band edge ε_c.

figure, the spectrum shifts towards the lower-frequency region with decreasing measurement temperature. This trend is understood as being a natural consequence of the lowered thermal emission rate with decreased temperature. The function $S(\omega)\omega$, shown in Fig.2-23(b), exhibits a well defined peak as predicted in the previous section, which again shows a reasonable shift with temperature. The modulation frequency at which the function $S(\omega)\omega$ is a maximum gives an estimate of the characteristic frequency ω_c defined in section 2-2. Then the modulation frequency ω is converted into the energy measured from the conduction band edge ε_c according to eqn.(2-13) for each temperature. The MPCS spectra $S(\omega)$ measured under different conditions, when plotted against the energy scale, give completely identical results [5]. It is suggested that the D^- centre has a distribution with a near-Gaussian shape centered at (an energy) about 0.33eV below ε_c. The magnitude of the attempt-to-escape frequency ν_n, which is estimated from eqn.(2-13) using the ω_c, is about 5.0×10^8 s^{-1} at 290K.

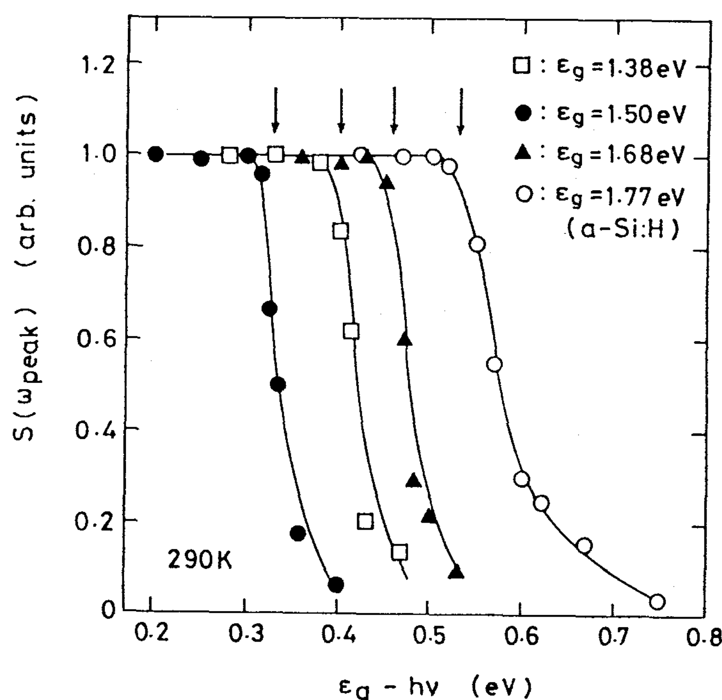

Fig. 2-24. Peak magnitude $S(\omega_{peak})$ of MPCS spectra plotted against ε_g-$h\nu$ at 290K for a-SiGe alloys of several bandgap energies. The arrows indicate ε_g-$h\nu$ at which a sharp reduction of the signal takes place, that is the peak energy of the D^- centre distribution measured from the conduction band edge.

An alternative way to determine the energy depth with relying on the excitation photon energy hν is to measure the magnitude of $S(\omega_{peak})$ with varying hν. Since only the states located deeper than ε_g-hν are populated with the subband-gap excitation and can contribute to the MPCS signal, the value of ε_g-hν at which a sudden decrease in the MPCS signal $S(\omega_{peak})$ occurs may identify the energy depth of the D^- centre. Figure 2-24 demonstrates how the magnitude of $S(\omega_{peak})$ varies with the ε_g-hν for a-SiGe:H alloys with several energy bandgaps. It is found that $S(\omega_{peak})$ exhibits an abrupt decrease at a particular value of ε_g-hν for each sample, providing an estimate of the energy depth of the D^- centre measured from the conduction band edge ε_c. For example, the energy depth of the D^- centre for a-SiGe:H with ε_g=1.5eV is read as 0.33eV, which coincides with that evaluated using the $S(\omega)\omega$ spectrum shown in Fig.2-23.

Identical energy depths were obtained from the above two methods for all the a-SiGe:H alloys employed in this work. The results are summarized in Fig.2-25, where the energy depth of the D^- centre is plotted against the bandgap energy. The energy location of the D^0 centre estimated from phase deconvolution of MPC spectrum [5)] and transient heterojunction-monitored capacitance measurement [33)36)] are also included in this figure. The energy of D^- centres exhibits smooth variations with the bandgap energy, except for the bandgap region near 1.5eV, where an abrupt change of about 0.1eV occurs towards the midgap. If a-SiGe:H contains only one kind of D^- centre, then the abrupt change in the D^- centre energy found between ε_g=1.5eV and 1.47eV may not be accounted for. Eventually the non-monotonic shift of the D^- centre energy is likely to offer an alternative support for our assignment of the origin of the D^- centre; that is, the Si D^- centre for $\varepsilon_g \geq 1.5$eV and Ge D^- centre for $\varepsilon_g < 1.5$eV. It is then suggested that the Ge D^- centre is located deeper by about 0.1eV than the Si D^- centre.

Combining the energies of D^0 and D^- centres yields an estimate of the correlation energy. If centre energies estimated by relying on the photon energy are used, the correlation energy will represent a bare value which differs from the effective correlation energy by the lattice relaxation energy involving dangling-bond transitions. The bare correlation energies are estimated to be about 0.4eV for the Si dangling bonds (group I) and about 0.3eV for the Ge dangling bonds (group II), which correspond to the upper limits of the effective correlation energies. Lattice

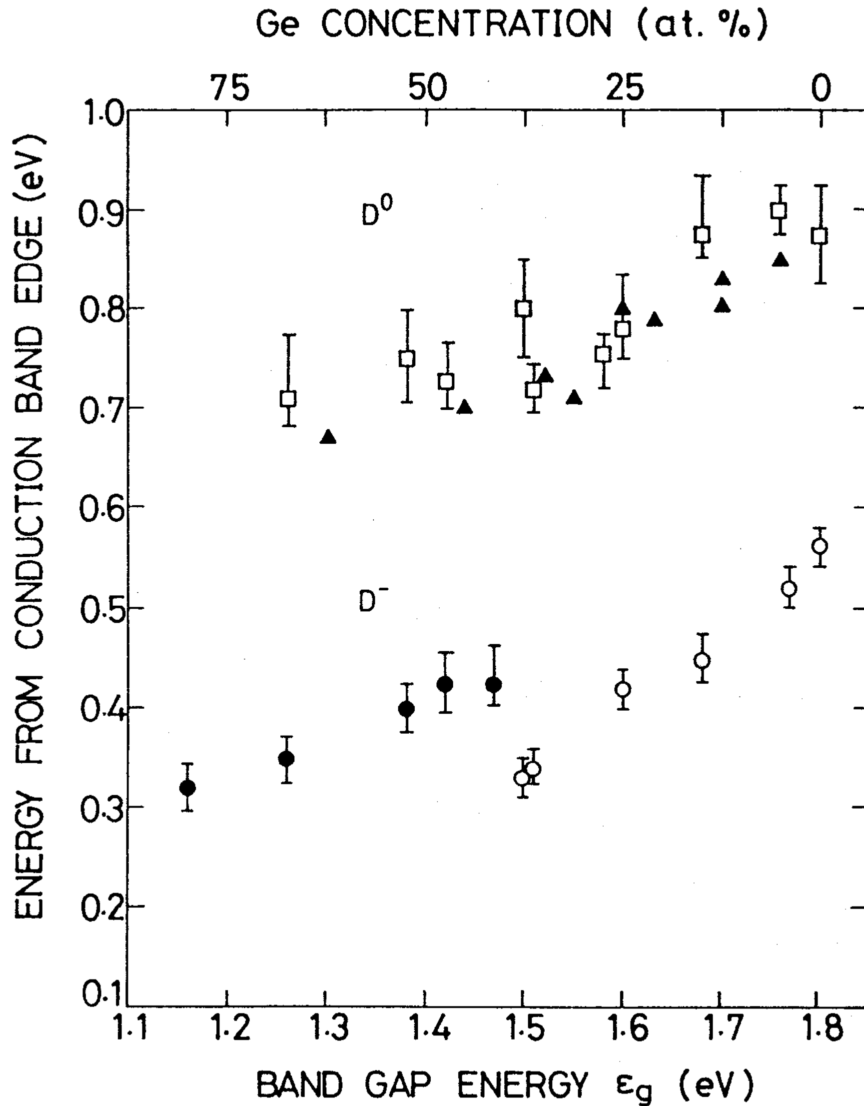

Fig. 2-25. Energy locations of D^- and D^0 centres plotted against bandgap energy for a-Si:H and a-SiGe:H. The D^- centre energy is estimated by the present MPCS measurement, while the D^0 centre energy, determined by the phase deconvolution of MPC and transient transient heterojunction-monitored capacitance measurement are also shown.

relaxation energies are estimated to be about 0.1eV or less for both the D^0-D^- and D^+-D^0 transitions associated with the Si dangling bond [15]. Then an effective correlation energy U_{eff} of about 0.2eV is deduced by combining these values and the bare correlation energy 0.4eV, in good agreement with recent estimates [37][38]. Concerning the Ge dangling bond, the corre-

sponding information is not available; however, if a similar extent of lattice relaxation is assumed, the effective correlation energy is roughly evaluated from the bare correlation energy 0.3eV obtained in the present measurement. The value is found to be about 0.1eV, which is consistent with the result from the analysis of ESR signal of a-Ge:H [39].

MPCS is essentially concerned with the distribution of the thermal emission rate from the D^- centre. In turn, the peak frequency ω_{peak} corresponds to the thermal emission rate $E_n(\varepsilon)$ from the centre of the D^- distribution. If the prefactor of $E_n(\varepsilon)$, that is the attempt-to-escape fre-

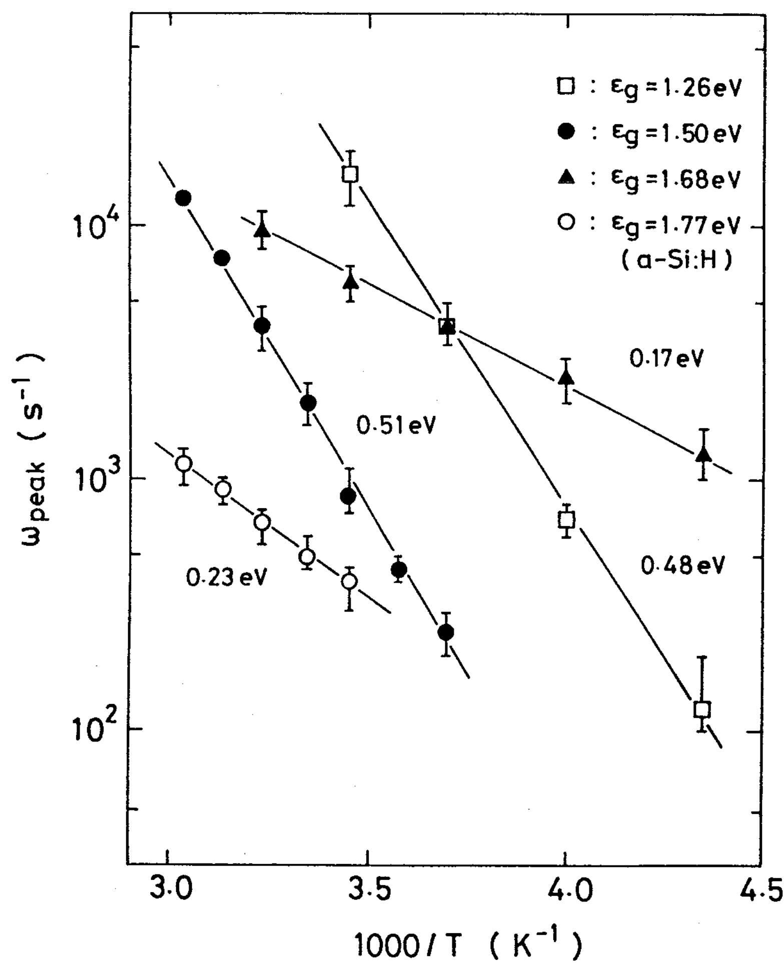

Fig. 2-26. Peak frequency ω_{peak} of the MPCS signal associated with the D^- centre as a function of reciprocal temperature for various bandgap energies. The numerals on the lines indicate the activation energies. The excitation photon energy used in the measurements are described in Fig. 2-21.

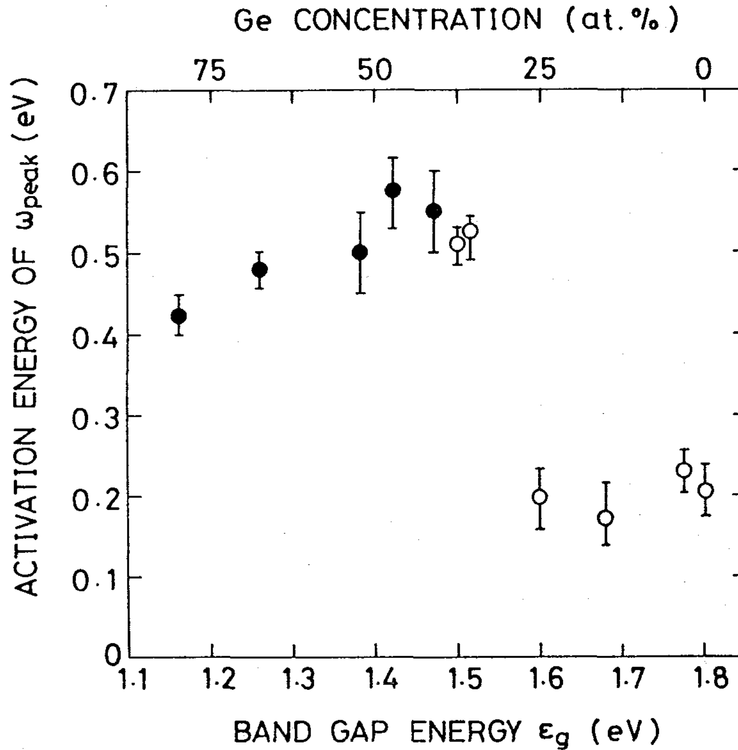

Fig. 2-27. Activation energy of peak frequency of the MPCS signal plotted against the band gap energy ε_g, associated with Si and Ge dangling bond. The excitation photon energy used in the measurements are described in Fig. 2-21.

quency ν_n, is assumed to have a weak temperature dependence such as T^2, the activation energy of $E_n(\varepsilon)$ will give the depth of the D^- centre which is extrapolated to zero temperature. On the basis of this idea, we have examined the temperature dependence of ω_{peak} for a-SiGe:H alloys. Some examples of the results are shown in Fig.2-26. The activation energy is summarized as a function of the bandgap energy in Fig.2-27. As indicated in this figure, the activation energy decreases monotonically for a-SiGe:H with ε_g<1.5eV on decreasing the bandgap energy, which is consistent with the behavior of the D^- centre energy deduced by the optical procedure. On the other hand, it is approximately constant, about 0.20eV, for the a-SiGe:H and a-Si:H having bandgap energies above 1.6eV. The D^- centre energy evaluated by this method differs by about 0.30eV from that estimated by the optical method, suggesting that the attempt-to-escape frequency ν_n has a strong temperature dependence. This point will be discussed in detail in section 2-4-3 in association with the carrier transition process through the D^- centre.

2-4-3. Electron transition process

In order to obtain an insight into the carrier transition process, we have examined the attempt-to-escape frequency ν_n as well as its temperature dependence according to the procedure described in section 2-2. Figure 2-28 shows the magnitude of ν_n measured at 290K. Within the temperature range covered in the present experiment, the observed ν_n for various temperatures fall on a single straight line in an Arrhenius plot, yielding an apparent activation energy $\Delta\varepsilon_v$. The quantity is also included in Fig.2-28. The energy depth of the D^- centre is basically evaluated from the activation energy of $E_n(\varepsilon)/\nu_n$ (in our case ω_{peak}/ν_n). The energy depth deduced by this procedure coincides with that measured by the optical method within a deviation of less than 0.05eV, which can be attributed to the probable temperature dependence of the centre energy. A recent optically detected magnetic resonance measurement reveals a change from Si-like to Ge-like behavior of the quenching signal in the Ge concentration region 20-40 at.% [40]. This observation clearly suggests that the transition from Si to Ge dangling bonds as the dominant non-radiative recombination centre occurs in such a composition range. The abrupt change in both ν_n and $\Delta\varepsilon_v$ found in Fig.2-28 seems to reflect this transition, thus confirming our assignment of the type of the D^- centre.

In Fig. 2-28, it appears that ν_n associated with the Ge D^- centre (ε_g<1.5eV) increases as the bandgap and thus the energy depth of the D^- centre decreases . This behavior of ν_n is reminiscent of the so-called 'energy-gap law' characteristic of the multiphonon emission (MPE) process in the weak-electron-phonon-coupling limit. In accordance to MPE theory in the weak-electron-phonon-coupling limit [41], ν_n is expressed by

$$\nu_n = \nu_0(T)\exp\left(-\gamma_{e-p}\Delta\varepsilon / \hbar\omega_{ph}\right), \qquad (2\text{–}19)$$

where $\Delta\varepsilon$ denotes the energy depth of the D^- centre, $\hbar\omega_{ph}$ is the frequency of phonons involved in the process, γ_{e-p} is a constant related to the strength of the electron-phonon coupling and $\nu_0(T)$ designates the temperature-dependent term including the Bose-Einstein probability function. The broken line in Fig.2-28 shows a theoretical plot calculated from eqn. (2-19), where $\nu_0(T)$ at

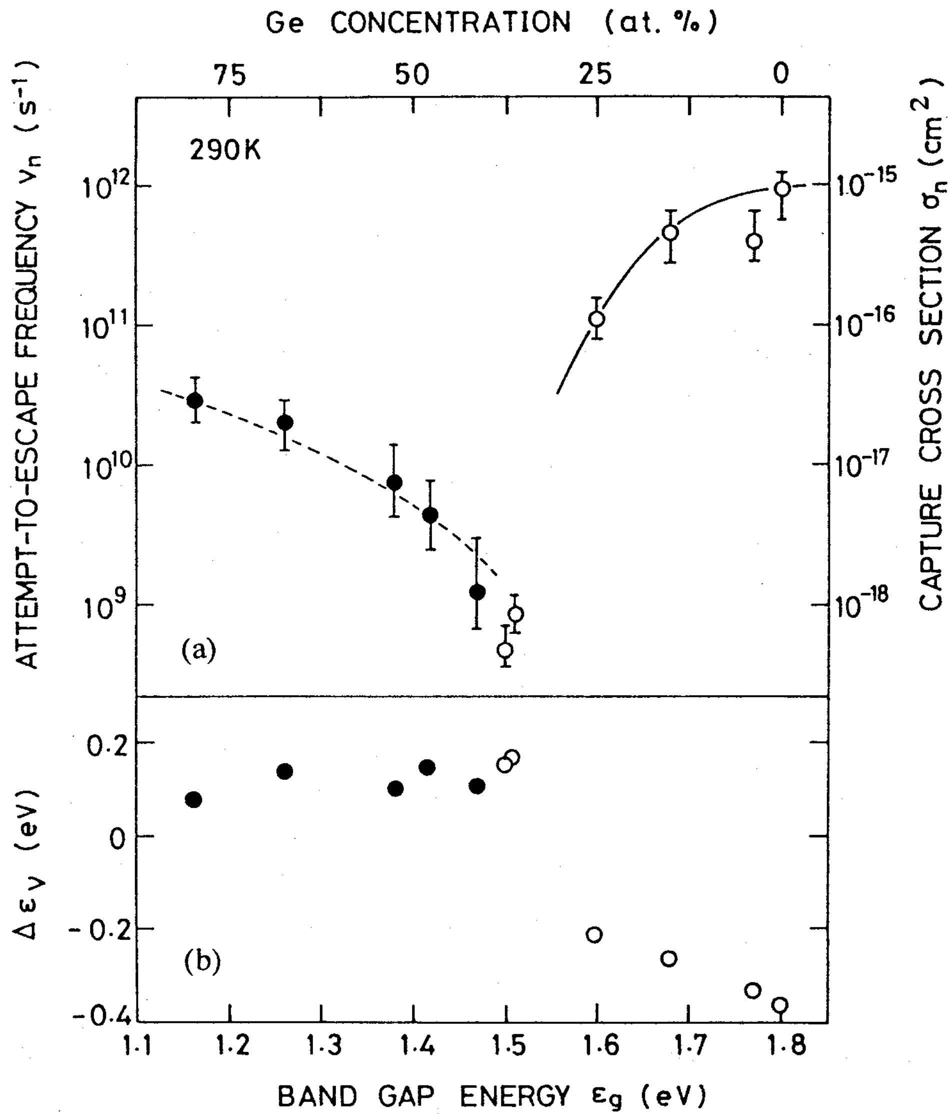

Fig. 2-28. (a) Attempt-to-escape frequency v_n measured at 290K and (b) the activation energy $\Delta\varepsilon_v$ as functions of bandgap energy ε_g for a-Si:H and a-SiGe:H. The open and closed circles identify whether the measured quantities associate with the Si or Ge dangling bonds. The solid and broken curves are theoretical plots of the ε_g dependence of the attempt-to-escape frequency v_n, as described in the text.

290K is chosen at 10^{13} s^{-1}, $\hbar\omega_{ph}/\gamma_{e-p}$=55meV and $\Delta\varepsilon$ is interpolated from the result in Fig.2-25. As found in the figure, the theoretical plot yields a good fit with the experimental data for the Ge D^- centre (ε_g<1.5eV). However, since the phonon frequency should vary with the material composition, the good fit obtained by using a particular value for $\hbar\omega_{ph}/\gamma_{e-p}$ does not immedi-

ately justify the present interpretation of the electron transition. The specific values of the parameters may be less important than the fact that the overall trends of the data are easily accounted for by the expression in eqn. (2-19) based on the multiphonon emission model assuming a weak-electron-phonon-coupling limit. If this interpretation is correct then, as is noted in section 2-4-2, a slight correction may be needed for the energy scaling to the depth of state distribution since ν_n should have a finite energy dependence expressed by eqn. (2-19), although it would be within the experimental uncertainty.

It is not straightforward to explain the anomalous behavior of ν_n and $\Delta\varepsilon_v$ for the Si D^- centre (ε_g>1.5eV); ν_n decreases as the bandgap and thus the energy depth of the D^- centre decreases, and moreover the activation energy $\Delta\varepsilon_v$ takes negative values. One possible explanation may be to consider that electron transitions between the conduction band state and the Si D^- centre take place by a two-stage process via an intermediate unrelaxed state, which is strongly coupled with the lattice [23)42)]. So far as the case for a-Si:H is concerned, this model could satisfactorily account for the anomalous temperature dependence of the observed ν_n, and the existence of an intermediate state has been directly confirmed by MPCS measurement carried out at low temperatures [3)]. Then, following this picture of electron transitions, we shall try to discuss the energy-gap dependence of ν_n observed for Si D^- centre (ε_g>1.5eV). The observed ν_n is expressed as a sum of contributions from the direct and two-stage transition processes [23)42)];

$$\nu_n = \nu_{n,g} + \{R\nu_n^* / [R + \nu_n^* \exp(-\varepsilon_d^* / kT)]\} , \qquad (2\text{-}20)$$

where R denotes the transition rate from the unrelaxed state located at an energy $\varepsilon_d{}^*$ below ε_c to the ground state of the D^- centre, $\nu_n{}^*$ and $\nu_{n,g}$ denote attempt-to-escape frequencies of the unrelaxed and ground states respectively. If the measurement is performed in the temperature region at which $\nu_n{}^*\exp(-\varepsilon_d{}^*/kT) >> R$, then eqn. (2-20) leads to

$$\nu_n = \nu_{n,g} + R \cdot \exp(\varepsilon_d^* / kT) . \qquad (2\text{-}21)$$

It is apparent from this equation that, as long as $R\exp(\varepsilon_d^*/kT) >> \nu_{n,g}$ and the temperature dependence of R is almost negligible, the observed ν_n behaves as $\exp(\varepsilon_d^*/kT)$, in agreement with the present experimental result. Then the activation energy of ν_n corresponds to the energy depth of the unrelaxed state of the D^- centre. Assuming that $\nu_{n,g}=10^8 s^{-1}$, $\nu_n^*=10^{12} s^{-1}$, $R=10^7 s^{-1}$ and $\varepsilon_d^*=0.7\varepsilon_g-0.89$ (eV) in eqn. (2-21) yields a theoretical curve for the ε_g dependence of ν_n, which is plotted as the solid line in Fig.2-28. Excellent agreement is obtained between the experimental and theoretical plots. A small value of $\nu_{n,g}$ yielding a good fit implies that electron transitions between ε_c and ground state of Si D^- centre are dominated by a multiphonon emission process in the weak-coupling limit as in the case of electron transitions for the Ge D^- centre.

The above discussion cannot be immediately applied to the behaviors of the attempt-to-escape frequency found for the alloys with the bandgap energies near 1.5eV. Almost all the experimental results show a discontinuity in the bandgap range between 1.5eV and 1.6eV, although the deep centre detected in the MPCS measurement seems to arise from the Si dangling bonds. As remarked in section 2-4-1, Si and Ge dangling bonds could coexist with roughly equal densities in these alloys, and they have slightly different energy positions. In such a situation, mixing of Si and Ge dangling-bond wavefunctions may take place, leading to a charge transfer between each dangling bond. If the effect is appreciable, then a significant influence should be exerted on the electron transition rate R from the ground state to the unrelaxed state of the Si D^- centre. It is likely that the effect results in a reduction in the transition rate, since the centre of gravity of the electron charge density moves away from the Si D^- site, which then may cause $\nu_{n,g} >> R\exp(\varepsilon_d^*/kT)$ for alloys with ε_g=1.5eV. Consequently, the attempt-to-escape frequency ν_n of the Si D^- centre is governed by the direct emission process ($\nu_{n,g}$) rather than by the two-stage emission process ($R\exp(\varepsilon_d^*/kT)$). The change in the emission process, which would take place at ε_g=1.5eV-1.6eV, thus well explains the discontinuities found in Figs 2-25, 2-27 and 2-28.

On the other hand, the charge-transfer effect should also modify the optical cross section σ_{opt} of the Si dangling bonds; possibly it enhances σ_{opt} because σ_{opt} of the pure Ge dangling

bond seems to be greater than for the pure Si dangling bond by a factor of two as discussed in section 2-4-1. This enhancement would have a close connection with the experimental result in Fig.2-22 in that $N\sigma_{opt}$ for ε_g=1.5eV takes mean values of those expected for the pure Si and Ge dangling bonds.

Finally, it should be noted that our interpretation of the behavior of the attempt-to-escape frequency observed for D^- centres associated with Si and Ge atoms may not be unique, and an alternative explanation could be possible. Effects of deviations from an ideal random alloy of Ge and Si may not be excluded [43], which tend to modify the electronic states of defects and electron transition processes involving them. If, however, our present interpretation is true, the obvious difference between the behaviors of ν_n found for the Si and for Ge D^- centres is attributed to whether an unrelaxed intermediate state is involved in the electron transition process or not. The question then arises why such a difference appears for the Si and Ge D^- centres. To give a clear-cut answer to this question is likely to require extended knowledge of the local environments of Si and Ge dangling bonds in non-ideal random alloys consisting of Si, Ge and H atoms. In the absence of such information, no firm conclusion can be drawn at the present stage of investigation.

Street, Tsai, Stutzmann and Kakalios [44] examined the role of dangling bonds in the transport and recombination of a-SiGe:H alloys by time-of-flight measurements and concluded that the capture cross-section of dangling bonds is not significantly different in a-SiGe:H with Ge concentrations below about 37 at.%. Karg, Kruhler, Moller and Von Klitzing [45] carried out similar experiments in a-SiGe:H alloys with the bandgap energy above 1.5eV (Ge composition x=0.25), and inferred relatively small changes of a factor of two to three in the capture cross-sections. These results obviously contradict our present observation, that is ν_n changes drastically with the Ge concentration. This contradiction may be reconciled if we suppose that the Si dangling bond is a dominant deep trap in a-SiGe:H alloys for Ge concentration below about 37 at.%. It should be noted here that the method of Street et al. deals with a fast decay of photocarriers after a short flash excitation. In this case, if the measurement is performed before the thermalization from the unrelaxed state to the conduction band takes place, the capture

cross-section which they observe may correspond to that of the unrelaxed state of the Si D^- centre. The attempt-to-escape frequency ν_n may be related to the capture cross-section σ_n by the relation $\sigma_n=\nu_n/N_c\upsilon$, where N_c denotes the effective density of states in the conduction band and υ the thermal velocity. On the assumption that $N_c=10^{20}$ cm^{-3} and $\upsilon=10^7$cms^{-1}, the capture cross-section σ_n^* is roughly estimated from the suggested value of ν_d^*. The value thus estimated, around 10^{-15} cm^2, agrees with those evaluated by Street et al.[44] and Karg et al. [45] for a-SiGe:H with the Ge concentration below 37 at.%.

2-5. Deep localized states in undoped a-SiC:H

In this section, the result of experiments on a-SiC:H alloys measured by means of the MPCS technique is presented. Samples employed in this work were Schottky barrier photocells consisting of undoped a-SiC:H alloys having 1.86eV and 2.01eV. The growth temperature was

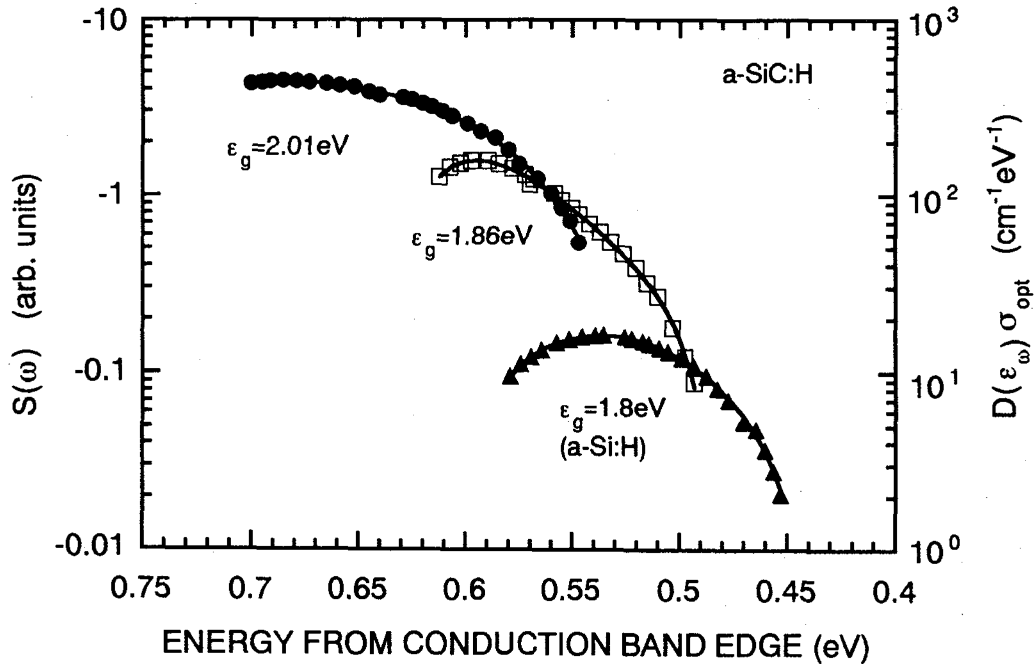

Fig. 2-29. MPCS spectra $S(\omega)$ measured for a-SiC:H alloys at 290K with various bandgap energies. The vertical axis at right-hand side is scaled to the state density multiplied by the optical cross section, $D(\varepsilon_\omega)\sigma_{opt}$, according to eqn. (2-9) in the text.

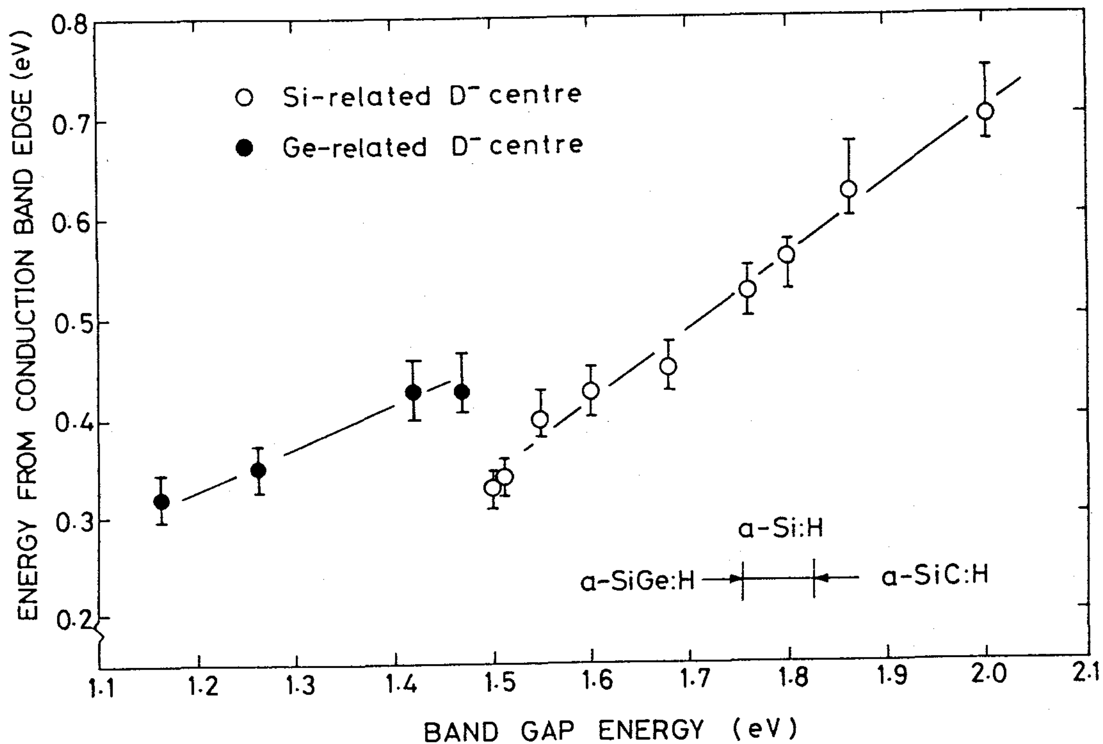

Fig. 2-30. Energy location of Si- and Ge-D^- centres plotted against band gap energy for a-Si alloy systems.

250°C.

The DOS distribution associated with D^- centre for undoped a-SiC:H having the band gap of 2.01eV and 1.86eV are shown in Fig.2-29. The MPCS spectra exhibit a single broad peak of a negative sign, indicating that the signal arises from an electron trap. We here tentatively assign this electron state as due to the doubly occupied dangling bond centre (D^-). The energy location of the D^- centre is summarized as a function of the bandgap energy in Fig.2-30. The energy location of Si-related and Ge-related D^- centres estimated for a-SiGe:H in section 2-4 are also included in this figure. For a-SiC:H alloys, the DOS peak shifts away from ε_C with increasing the band gap. We assign the DOS peak in a-SiC:H of band gap less than 2.01eV as being originated from Si-related D^- centre.

2-6. Mobility-lifetime products

In general, the photovoltaic performance of a-Si based solar cells is essentially governed by the mobility-lifetime products of the photosensitive layer, although the interface property as well as the internal electric field distribution have also significant affects on it. The mobility-lifetime products can be estimated from the bias voltage dependence of the carrier collection efficiency [46].

Figure 2-31 compares the mobility-lifetime products with the density of D^- centre, estimated by the MPCS technique, for a-Si:H and a-SiGe:H alloys. A unique inverse-proportionality stands for these two quantities irrespective of alloy composition, so far as the band gap energy is larger than 1.5eV. An important implication from this result is that dangling bond centre is the dominant recombination centre, while the H1 centre which exists with a consider-

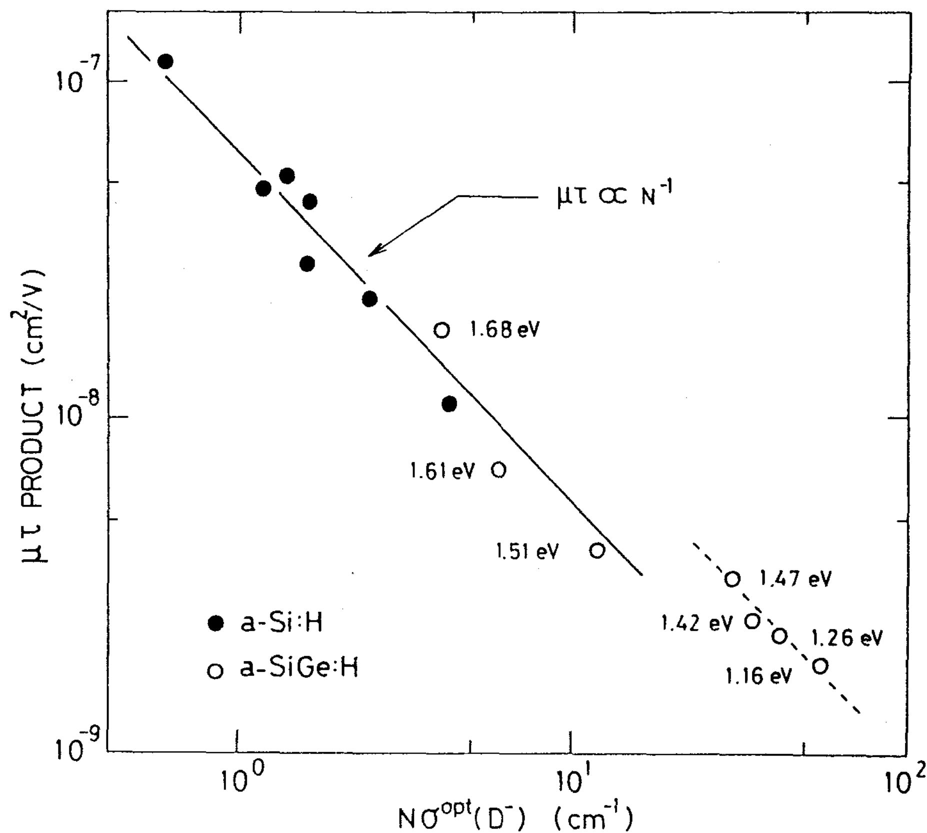

Fig. 2-31. Relation between mobility-lifetime products and MPCS dangling bond centre density for a-Si:H as well as a-SiGe:H alloys of band gap energies indicated in the figure.

able density in a-Si:H prepared at lower temperatures does play only a negligible role in carrier recombination. Concerning a-SiGe:H alloys, the Si dangling bond appears to dominate carrier recombination in the alloys with band gap energies larger than 1.5eV; Ge concentration below about 35 at.%. In turn, the above results indicate that the thermal equilibrium occupation of the Si dangling bonds as well as the capture cross section, presumably of holes, may not largely change with an incorporation of Ge. On the other hand, the discontinuity found between the band gap energies from 1.51eV and 1.47eV is interpreted as due to the switch of dominant recombination centre from Si dangling bonds to Ge dangling bonds. This conclusion is consistent with that reached from the recent ODMR experiments made on a-SiGe:H alloys [47].

2-7. Summary

We have developed a new gap-state spectroscopy (named to MPCS) based upon the frequency-resolved spectrum of subband-gap modulated photocurrent and have investigated the energy location and nature of deep states in undoped a-Si:H by the MPCS. The energy scale is specified by the energy of the subband-gap light which is used to populate the deep states which are normally unoccupied. This spectroscopy enables us to measure simultaneously the gap-state distribution and attempt-to-escape frequency under isothermal condition, as well as to identify whether the observed states are an electron trap or a hole trap.

The result from experiments made on an undoped a-Si:H has led to the conclusion that the peak of the gap-state distribution associated with doubly occupied dangling-bonds(D^-) is located about 0.5eV below the conduction band edge. The analysis for the pre-exponential factor of the thermal emission rate of the electron from the D^- centre suggested that the emission occurs in two stages through unrelaxed states. In addition, two types of defect centre are observed in undoped a-Si:H, one of which is assigned as due to a dangling bond. Upon light soaking, the densities of not only the dangling bonds but also as-yet unidentified defect centre (H1) designate systematic changes, suggesting that these two centres are involved in the photo-induced degradation effects although the dangling bonds may play a central role in carrier recombination.

Moreover, the MPCS has been utilized to investigate the energy location and nature of dangling bonds in undoped a-SiGe:H and a-SiC:H alloys, with particular emphasis on the doubly occupied dangling bond (D^-) centre. It is found that the Ge D^- centre lies by about 0.1eV below the Si D^- centre, while a sharp switch of the predominant deep centres occurs from Si dangling bonds to Ge dangling bonds as the Ge concentration approaches about 35 at.% which corresponds to an optical bandgap energy around 1.5eV. The analysis for the pre-exponential factor of the thermal emission rate of electron from the D^- centre suggests that different electron transition processes are operative for Si and Ge dangling bonds. For a-SiC:H with the band gap less than the 2.01eV, only Si-related D^- centre has been observed. The density-of-states distribution associated with D^- centre is summarized for a-Si:H alloys of various band gaps in Fig. 2-32, where the absolute magnitude of density-of-states is given by using the optical cross-sections estimated at section 2-4, which are $1.3\times10^{-16}cm^2$ for Si dangling bonds and $3.0\times10^{-16}cm^2$ for Ge dangling bonds.

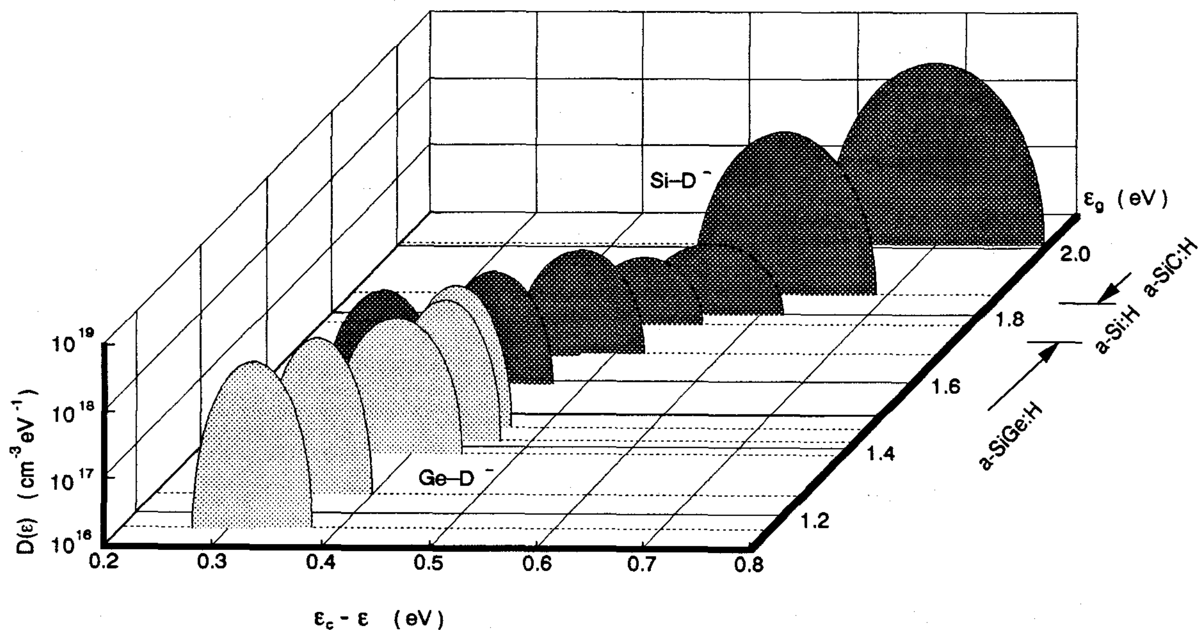

Fig. 2-32. Density-of-states distribution of Si-related D^- centre (▩) and Ge-related D^- centre (▢) in a-Si:H alloys of variou band gaps. Here, the absolute magnitude of density-of-states is given by using the optical cross-sections estimated at section 2-4, which are $1.3\times10^{-16}cm^2$ for Si dangling bonds and $3.0\times10^{-16}cm^2$ for Ge dangling bonds.

References

(1) D. L. Lang, J. D. Cohen and J. P. Harbison, Phys. Rev. B, 25 (1982) 5285.

(2) H. Okushi, Phil. Mag. , B, 52 (1985) 33.

(3) K. Abe, H. Okamoto, Y. Nitta, Y. Tsutsumi, K. Hattori and Y. Hamakawa, Phil. Mag. B, 58, (1988) 171.

(4) Y. Tsutsumi, H. Okamoto and Y. Hamakawa, Phil. Mag. B, 60 (1988) 695.

(5) Y. Tsutsumi, S. Sakata, K. Abe, Y. Nitta, H. Okamoto and Y. Hamakawa, J. Non-Cryst. Solids, 97/98, 1063 (1987).

(6) Y. Tsutsumi, K. Abe, Y. Nitta, H. Okamoto and Y. Hamakawa, Tech. Dig. International PVSEC-3, Tokyo, (1987) 675.

(7) Y. Tsutsumi, K. Uchiyama, H. Okamoto and Y. Hamakawa, J. Non-Cryst. Solids, 114 (1989) 627.

(8) H. Okamoto, H. Kida and Y. Hamakawa, Phil. Mag., B, 41 (1983) 231.

(9) H. Okamoto, H. Kida, H. Kamada and Y. Hamakawa, Phil. Mag. B, 52 (1985) 1115.

(10) H. Oheda, J. appl. Phys., 52 (1981) 6693.

(11) H. Kida, T. Kamada, H. Okamoto and Y. Hamakawa, Solid St. Commun., 59 (1986) 233.

(12) J. Tauc and Z. Vardeny, Phil. Mag. B, 52 (1985) 313.

(13) I. Hirabayashi and K. Morigaki, Phil. Mag. B, 54 (1986) L119.

(14) A. V. Geratos, J. D. Cohen and J. P. Harbison, Appl. Phys. Lett., 49 (1986) 722.

(15) K. Hattori, H. Okamoto and Y. Hamakawa, Philos. Mag. B, 57 (1988) 13.

(16) K. Morigaki, Y. Sano and I. Hirabayashi, Solid St. Commun., 39 (1981) 947.

(17) R. A. Street, Phil. Mag. B, 49 (1984) L15.

(18) H. Kida, K. Hattori, K. Okamoto and Y. Hamakawa, J. appl. Phys., 59 (1986) 4047.

(19) H. Fritzsche, Sol. Energy Mater., 3 (1980) 447.

(20) R. A. Street, J. Zesch and M. J. Thompson, Appl. Phys. Lett., 43 (1983) 672.

(21) W. E. Spear, H. L. Streemers, P. G. LeComber and R. A. Gibson, Phil. Mag. B, 50 (1984) L33.

(21) W. E. Spear, A. C. Hourd and S. Kinomond, J. Non-Cryst. Solids, 77/78 (1985) 607.

(22) P. G. LeComber and W. E. Spear, Phil. Mag. B, 53 (1986) L1.

(23) R. M. Gibb, G. J. Rees, B. W. Thomas, B. L. Wilson, B. Hamilton, D. R. Wight and N. F. Mott, Phil. Mag. B, 36 (1977) 1021.

(24) R. Englman and J. Jortner, Molec. Phys., 18 (1970) 145.

(25) H. Okushi, T. Tokumaru, S. Yamasaki, H. Oheda and K. Tanaka, Phys. Rev. B, 27 (1983) 5184.

(26) H. Okamoto, Y. Tsutsumi, K. Abe and Y. Hamakawa, PVSEC, Sydney (1987) 71.

(27) S. Yamasaki, S. Kuroda and K. Tanaka, AIP Proc., Vol.157 (1987) 9.

(28) D. Adler, in "Semiconductors and semimetals, Vol.21A" ed. by J.I. Pankove (Academic Press, N.Y.,1984), p.291.

(29) M. Stutzmann, Phil. Mag. B, .56 (1988) 63.

(30) H. Yamagishi, H. Okamoto and Y. Hamakawa, Appl. Phys. Lett., 47 (1985) 860.

(31) S. Aljishi, V. Chu, Z. E. Smith, D. S. Shen, J. P. Conde, D. Slobodin, J. Kolodzey and S. Wagner, J. Non-Cryst. Solids, 97/98 (1978) 1023.

(32) H. Matsuura, Jpn. J. appl. Phys., 27 (1988) L513.

(33) H. Matsuura, J. appl. Phys., 64 (1988) 1964 .

(34) A. Morimoto, M. Miura, M. Kumeda and T. Shimizu, Jpn. J. appl. Phys., 20 (1981) L833.

(35) M. Stutzmann, W. B. Jackson and C. C. Tsai, J. Non-Cryst. Solids, 77/78 (1985) 363.

(36) H. Matsuura, Jpn. J. appl. Phys., 27 (1988) L516.

(37) A. V. Gelatos, J. D. Cohen and J. P. Harbison, Appl. Phys. Lett., 49 (1986) 722.

(38) M. Stutzmann, W. B. Jackson, R. A. Street and D. K. Biegelsen,Tetrahedrally-Bonded Amorphous Semiconductors, edited by M.A.Kastner, G.A.Thomas, and S.R.Ovshinsky (Plenum Press, New York, 1987), p.407.

(39) M. Stutzmann, J. Stuke and H. Dersch, Phys. Stat. Sol.(b), 115 (1983) 141.

(40) J. Ristein, F. Finger, W. Fuhs and S. Liedtke, Solid St. Commun., 67 (1988) 211 .

(41) N. Robertson and L. Friedman Phil. Mag. B, 33 (1978) 753.

(42) G. J. Rees, H. G. Grimmeiss, E. Janzen and B. Skarstam, Solid St. Phys., 13 (1980) 6157.

(43) K. D. Mackenzie, J. R. Eggert, D. Leopold, Y. M. Lin and W. Paul, Phys. Rev. B, 31 (1985) 2198.

(44) R. A. Street, C. C. Tsai, M. Stutzmann and J. Kakalios, Phil. Mag. B, 56 (1987) 289.

(45) F. Karg, W. Kruhler, M. Moller and K. Von Klitzing, J. appl. Phys., 60 (1986) 2016.

Chapter 3. CHARACTERIZATION OF SHALLOW LEVEL STATES

3-1. Introduction

In Chapter 2, the author has discussed the nature and the distribution of the deep localized states in undoped a-Si:H measured by the use of modulated photocurrent spectroscopy (MPCS) which is based on the frequency-resolved spectrum of junction photocurrent under subband-gap illumination (1)(2). The energy interval of the deep localized states in a-Si:H observed by the MPCS is between 0.4eV and 0.6eV from both the extended band edges at room temperature. Time-resolved photocurrent spectroscopy (TPCS) on the practical a-Si:H solar cell structure has been used to investigate the localized states lying shallower than the dangling bond states [3], which are located at about 0.5eV from the conduction band edge, because several experimental results have appeared inferring an important role of such states played in determining carrier transport property as well as in the light induced phenomena. The experimental procedure is identical with that in conventional Time-of-Flight measurement [4], while a new analytical procedure has been introduced to extract localized states distribution from photocurrent transients. Shortly speaking, effects of multiple trapping process [4][5] are precisely taken into account, without which deduced density-of-states profile tends to involve a large ambiguity, particularly for the shallower energy region. The complementary use of the modulated-photocurrent spectroscopy (MPCS) [1][6] and the present TPCS [3] permits us to measure separately the electron and hole states in the energy interval between 0.25 eV and 0.6 eV from the conduction and valence band edges at room temperature. This chapter describes an outline of TPCS as well as some details of experimental results on undoped a-Si:H. The density-of-states profile measured on undoped a-Si:H designates a pronounced peak (electron trap) at about 0.35 eV below the conduction band edge, which is about 0.15 eV shallower than the doubly-occupied dangling bond states. A broad bump structure (hole trap) is also found out at around 0.4eV above the valence band edge. At the present stage of investigation, the origin of these newly-observed localized states is not yet identified, however, they appear to be closely linked with the light-induced effects.

3-2. Time-resolved photocurrent spectroscopy (TPCS)

3-2-1. Principle of TPCS

When the p-i-n junction cell consisting of undoped a-Si:H is illuminated with a short pulse of strongly-absorbed light, excess carriers of both types are created close to one electrode of a photocell. Carriers of one sign drift through the cell under an appropriate reverse bias condition and the photocurrent transients flow in the external circuit. Within the context of the multiple-trapping model, neglecting recombination and diffusion of carriers, the linear differential equations for free carrier density induced in the i-th trap level (density N_i) are expressed as

$$\frac{\partial n}{\partial t}=-\mu E\frac{\partial n}{\partial x}+\sum_i [E_i f_i - C_i n(1-f_i)]N_i \tag{3-1}$$

and

$$\frac{\partial}{\partial t}f_i = C_i(1-f_i)n - E_i f_i\,, \tag{3-2}$$

where μ is the free carrier mobility, E the applied field which is assumed to be uniformly distributed across the sample. N_i trapping density, f_i the probability of occupation for i-th trap level, and E_i and C_i are the thermal emission rate and capture rate of the i-trap level, respectively. Since we are interested in the transient response of the system to an impulse at t=0, these equations are to be solved simultaneously by Laplace transforms. When the injected charge density Q_0 is assumed to be low enough that the carrier traps are not saturated, the solution in the Laplace variable "s" domain for transient photocurrent J(t) is

$$\hat{J}(S) = Q_0\, e^{-\hat{W}\frac{\partial}{\partial S}}\cdot\hat{J}_0(S)\,. \tag{3-3}$$

Here, $\hat{W}, \hat{J}_0(S)$ are defined as

$$\hat{W}=\sum_i \frac{SC_i}{S+E_i}N_i \tag{3-4}$$

and

$$\hat{J}_0=\frac{1}{t_{T_0}}\int_0^{t_{T_0}} e^{-u\cdot S}\,du=\langle e^{-u\cdot S}\rangle, \tag{3-5}$$

where t_{T0} is transit time for free carriers. The $\hat{W}$ denotes waiting function in Laplace transform, and $\hat{W}^n$ represents the physical process that carriers experience n-times trapping events. $\hat{J}_0(S)$ describes a current transient in the trap free case.

When we consider the case of a-Si:H alloy in which traps are continuously distributed in the gap, the trap density N_i may be replaced with the localized state density (DOS) $D(\varepsilon_t)$. Therefore, the localized states distribution is deduced approximately from the following equations.

$$D(\varepsilon_t)\cong\frac{1}{CkT}W(t)\times t \tag{3-6}$$

$$\varepsilon_t= kT\,\ln(\nu\, t)\,. \tag{3-7}$$

where k is the Bolzmann constant and ν the attempt-to-escape frequency. Note that eq.(3-6) assumes energy-independent capture-rate C for all traps. Upon this assumption, the determination of localized DOS $D(\varepsilon_t)$ is reduced to the evaluation of waiting-function W(t) from the measured current response. However, if this procedure is to be formally attempted through solving eq.(3-3), the problem becomes exceedingly complex and beyond the scope of realistic characterization.

As an alternative way to approach the problem, we now introduce the cumulant average defined by [7)]

$$\langle e^x \rangle = \exp[\langle e^x \rangle_c - 1] \,. \tag{3-8}$$

For the case of $t >> t_{T0}$, By using the cumulant average, eq.(3-5) is expressed to a good approximation;

$$\hat{J}_0(S) = \exp\left[-\langle u \rangle_c \bullet S + \sum_{m=1}^{\infty} \frac{S^{2m}}{(2m)!} \langle u^{2m} \rangle_c \right] \cong \exp\left[-\frac{t_{T_0} S}{2} + \frac{(t_{T_0} S)^2}{24} \right] . \tag{3-9}$$

Substituting eq.(3-9) into eq.(3-3) yields

$$\hat{J}_0(S) = Q_0 \exp\left[-\frac{t_{T0}}{2} (S - \hat{W}) + \frac{t_{T0}^2}{24} (S - \hat{W})^2 \right] . \tag{3-10}$$

Then, the equation may be solved for $\hat{W}$ in an iterative series, resulting in the final analytical formula connecting the DOS and measured current response;

$$D(\varepsilon_t) = \frac{1}{C\, t_{T0}\, kT} \lim_{k_m \to \infty} \sum_{r=1}^{k_m} B_r \cdot J^{(r)} / Q_0^r , \tag{3-11}$$

where

$$J^{(r)} = \int_0^t J^{(r-1)}(t-u) \bullet J(u)\, du \tag{3-12}$$

$$B_r = 2 \sum_{k=r}^{k_m} \sum_{n=1}^{k} kCr \frac{(2n-1)!!}{n! \bullet 3^{n-1}} (-1)^{r+1} \times \sum_{m_i = 1..\infty} \left[\prod_{i=1}^{n} \frac{1}{m_i} \right] \;;\; \sum_{i=1}^{n} m_i = k \,. \tag{3-13}$$

It is clear from eq.(3-10) that carrier trapping events to infinite times, that is, the multiple trap-

ping effect is fairly taken into account in the present analysis.

3-2-2. Simulation studies

What happens if the analysis is applied to the anomalously dispersive current transients [4)5)8)] associated with exponentially distributed trap states is demonstrated in Fig 3-1, in order to show the usefulness of the present analysis based upon eq.(3-11). In this figure t_T denotes the apparent carrier transit time. For comparison, the $(Jxt)^{-1}$ [9)] for pre-transit regime ($t<t_T$) and Jxt [10)] for post-transit regime ($t>t_T$), which are used in the conventional analysis, are also drawn in this figure [9)]. The density-of-states derived by our analysis appears to reproduce well the original exponential distribution in the entire time domain without dividing it into the "pre" and "post" transit regions.

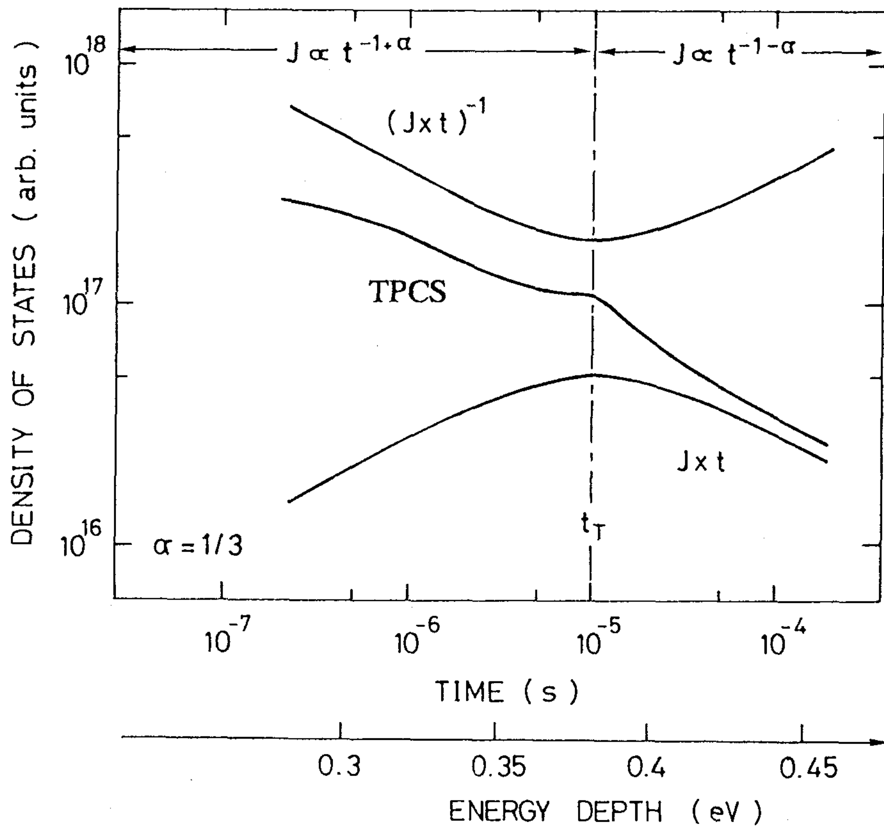

Fig.3-1. Plots of DOS for anomalously dispersive current transients ($\alpha=1/3$) derived from eq.(3.11). Spectra $(Jxt)^{-1}$ for pre-transit regime ($t<t_T$) and Jxt for post-transit regime ($t>t_T$) are also drawn for comparison.

3-2-3. Experimental details

Samples employed in this work were p-i-n or n-i-p junction photocells. The cell structures were glass/ITO/p a-SiC:H/i a-Si:H/n μc-Si:H/Al or glass/ITO/n μc-Si:H/i a-Si:H/p a-SiC:H/Al. The amorphous and microcrystalline layers were prepared by the r.f. plasma deposition technique from a SiH_4/H_2 (1:9) mixture containing the desired amount of CH_4,B_2H_6 or PH_3. The substrate temperatures during the deposition were mainly 250°C. The layer thicknesses were 200Å and 300Å for p and n layers, respectively. The i layer thickness of the p-i-n photocells used in MPCS and TPCS for electron trap were 5000Å and 4.0μm, respectively. The i layer thickness of the n-i-p photocells employed in TPCS for hole transport was 7000Å.

TPCS measurement system is shown in Fig.3-2. Excess carriers were generated by a 300ps flash of light from a N_2 laser of wavelength 337nm. The reverse bias is applied in the form of a pulse by a pulse generator. Then, the photocurrent transients were measured over a time interval from 10^{-8}s to 10^{-3}s, using a 100MHz digital storagescope with a high-gain amplifier. To extract real transport current from the measured current transients, the RC responses of the sample and measuring circuit were also measured. The real-time operation of N_2 laser,

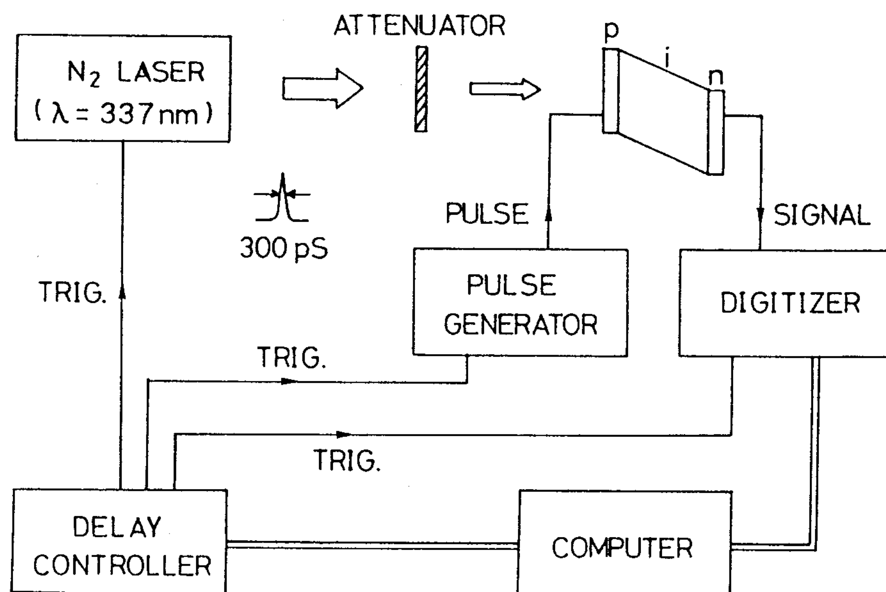

Fig.3-2. TPCS measurement system

delay generator and digital storagescope, and data acquisition and data processing including the CR correction are performed by a personal computer system.

3-3. Shallow level states in undoped a-Si:H

3-3-1 Electron traps

Figure 3-3 shows time resolved spectrum of photocurrent transients, for which raw photocurrent data are compensated with RC response of the sample and measuring circuit, on a p-i-n cell deposited at 250 °C after the end of the illumination pulse of light. The photocurrent was measured over a wide time range with the illumination on p-layer at room temperature. Here the injection charge was 35pC for the electrode area 0.033cm2, and the applied reverse bias -0.5V. In this experiment, the measurement time is short compared to the dielectric relaxation time, say about 30ms, so that the charge separation and a completed transit is likely to occur before local neutralization may take place. The density of states distribution of the electron traps estimated from eq.(3-11), in which J is the photocurrent obtained by subtracting the leak-

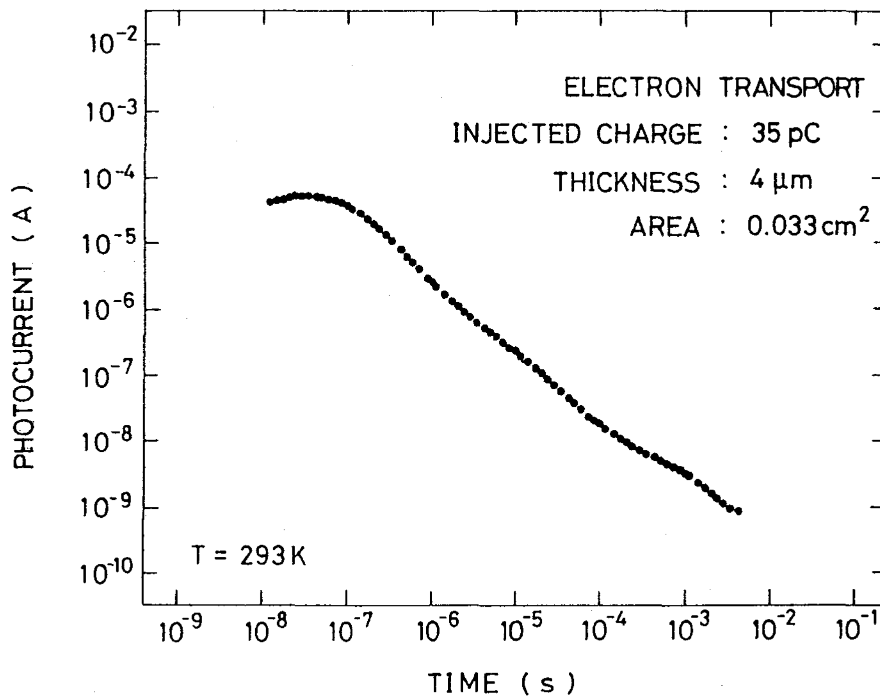

Fig.3-3. Time-resolved spectrum of photocurrent transients for undoped a-Si:H p-i-n cell deposited at 250°C.

age current from the measured photocurrent, is plotted against the inverse time with solids line in Fig.3-4. The broken line in this figure indicates the results of Jxt product. As can be seen in the figure, the shape of the broken line differs substantially from that of the solids line in the shorter region of time. This suggests an importance of correction based upon the multiple-trapping process, which is introduced first in this work.

The figure reveals two distinct DOS structures except an exponential rise toward the conduction band edge; a broad bump at 10^2-10^4 s^{-1} and more pronounced peak at about 10^5 s^{-1}. Also shown in Fig.3-4 is the density of states distribution obtained by MPCS measurement for the sample deposited with the same condition. Since the MPCS is comprised of optical process in forming the non-equilibrium trap occupation, a direct comparison of DOS profiles determined by the MPCS and "pure" electrical TPCS may not be meaningful, nevertheless the results

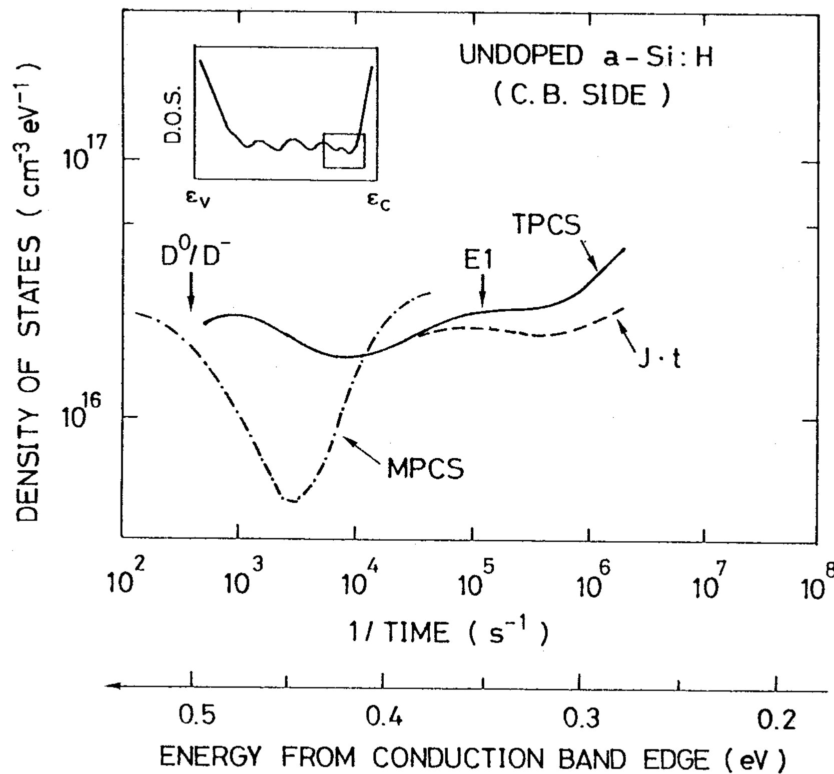

Fig.3-4. DOS distribution of electron trap states determined by eq.(3.11) with solid line. Here ν is assumed to be 10^{11} s^{-1}. The broken line indicates the result of Jxt product. The spectrum obtained by MPCS measurement is also plotted against the energy depth from the conduction band edge (the dash-dotted line).

from these two techniques exhibit an essential agreement on the point, at least, that there exist two DOS structures indicated by arrows in the figure. If we adopt the energy scale determined by the MPCS, which is given in Fig.3-4, the two electron states are located at 0.5eV and 0.35eV below the conduction band edge ε_c. The deeper states are assigned as due to doubly occupied dangling bond states (D^-), while any clear-cut identification is not yet available for the shallower states (named as E1) although the MPCS suggests the possibility of an unrelaxed states of the D^- center [1].

3-3-2. hole traps

We have applied the present method to n-i-p photocell, of which i layer thickness is 7000Å, and have carried out the measurement of the hole transport. The density of states

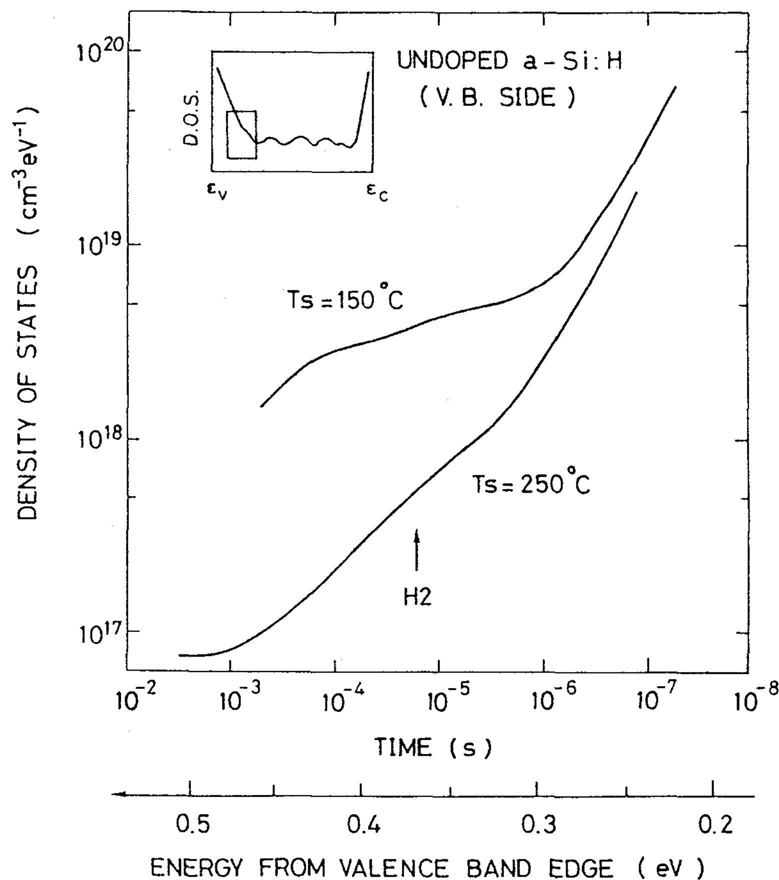

Fig.3-5. DOS distribution of hole trap states for undoped a-Si:H samples deposited at 250°C and 150°C. ν is assumed to be 10^{11} s^{-1}.

distribution of hole traps states obtained is plotted against the time for two undoped a-Si:H samples deposited at different temperatures in Fig.3-5. Just for reference, the horizontal time axis is scaled to energy above the valence band edge by using a similar attempt-to-escape frequency to electron traps. The hole trap DOS reveals an exponential tail of the characteristic slope about 40meV and a shoulder (named as H2) at about 0.4eV above the valence band edge, which becomes pronounce for the sample prepared at a low temperature. The shoulder structure may give a partial contribution to the defect-absorption found commonly in the subband gap absorption of a-Si:H, which is conventionally ascribed to the dangling bond transition.

3-3-3 Density-of-states profile

The gap-states distribution in device-quality a-Si:H deduced from the TPCS technique (solid lines) is schematically displayed in Fig.3-6, with the results from the MPCS technique

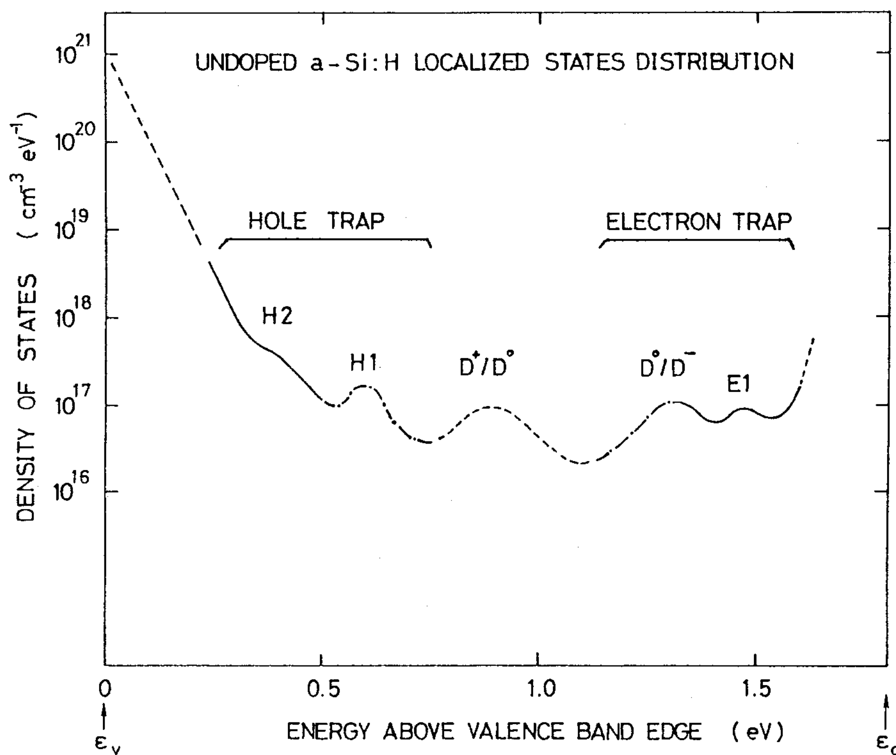

Fig.3-6. Gap-states distribution in device-quality a-Si:H deduced from the TPCS technique (solid lines). The results from the MPCS technique (dash-dotted lines) as well as other related measurements (broken lines) are also shown in this figure.

(dash-dotted lines) as well as other related measurements (broken lines). Besides well known dangling bonds ($D^+/D^0$and D^0/D^-), at least three well-distinguishable deep-lying states (E1, H1 and H2) are observed, of which the origin and nature are poorly understood and await for further investigation in association with impurity and photo-induced metastability effects.

3-3-4. Light-induced changes

In this section, we have examined the effect of light soaking on the deep localized states in undoped a-Si:H by means of the TPCS and MPCS. For the light soaking, the light from a solar simulator (AM1, 100mW/cm^2) was used. The treatment was carried out in the short-circuit condition.

Figure 3-7 shows the TPCS spectra of electron before and after light soaking for 10min on an a-Si:H p-i-n cell deposited at 200°C. The DOS distribution of the electron traps estimated

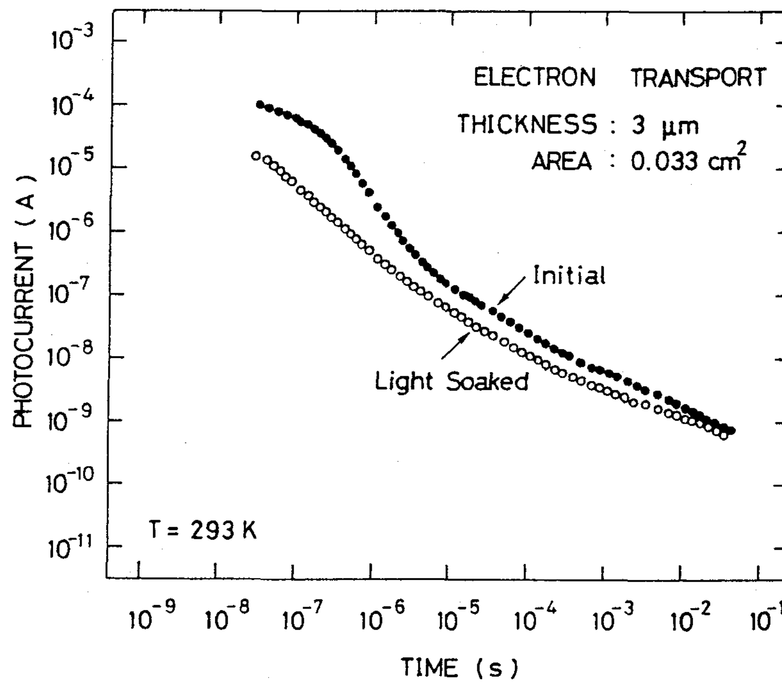

Fig.3-7. TPCS spectra of electron before and after light soaking for 10min on an a-Si:H p-i-n cell deposited at 200°C.

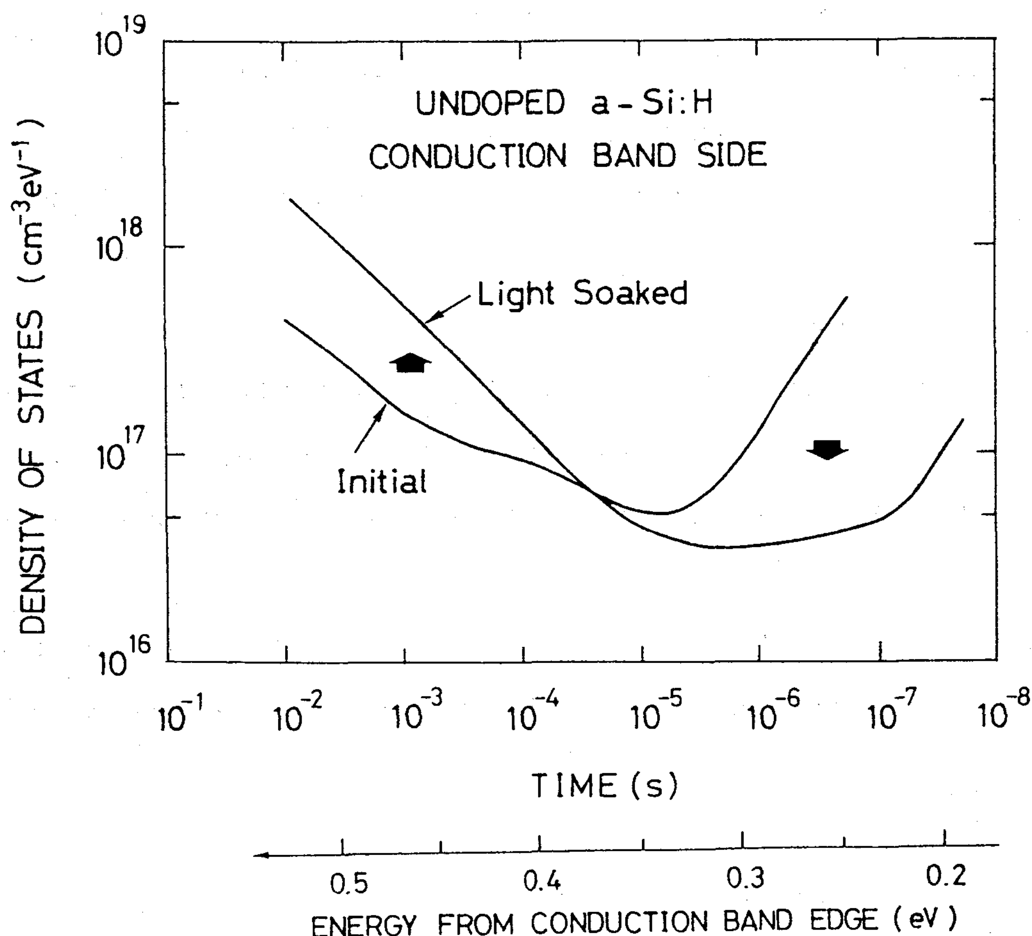

Fig.3-8. DOS distribution of the electron traps estimated from eqn. (3-11) plotted against the time.

from eqn. (3-11) is also plotted against the time in Fig.3-8. Fig.3-8 indicates that the density of deep-states deeper than the energy of about 0.45eV from the conduction band edge ε_c, which is equivalent to 5×10^4 s^{-1} with $\nu_n=10^{-11}s^{-1}$, increases with light-soaking, while that of states shallower than the energy decreases.

Next, we have carried out the light soaking for 30min on n-i-p photocell deposited at 200°C. Figure 3-9 shows change in TPCS spectra with light soaking. The DOS distribution of the hole traps is also shown in Fig.3-10. As can be seen in this figure, a shoulder at about 10^4s^{-1}, which named H2 in previous section, remarkably decreases with light soaking. The change in the density of states observed by the TPCS is summarized in Fig.3-11.

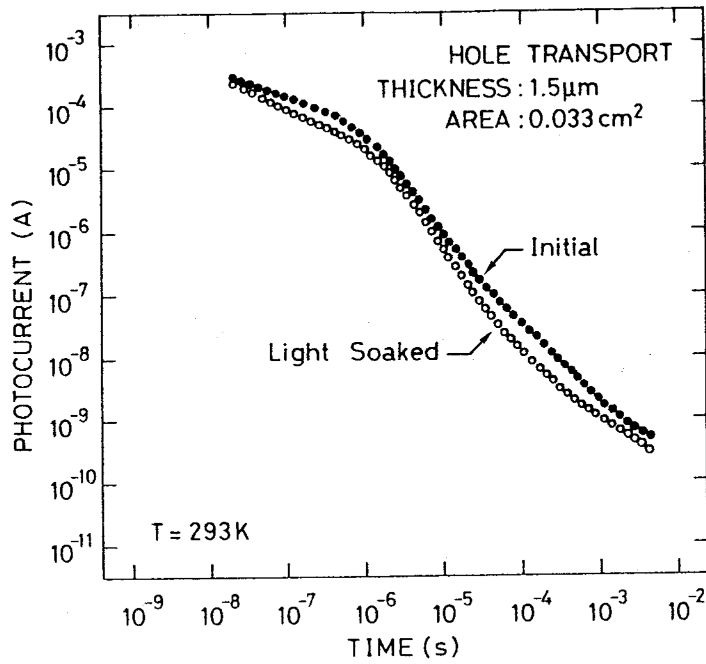

Fig.3-9. Change in TPCS spectra with light soaking

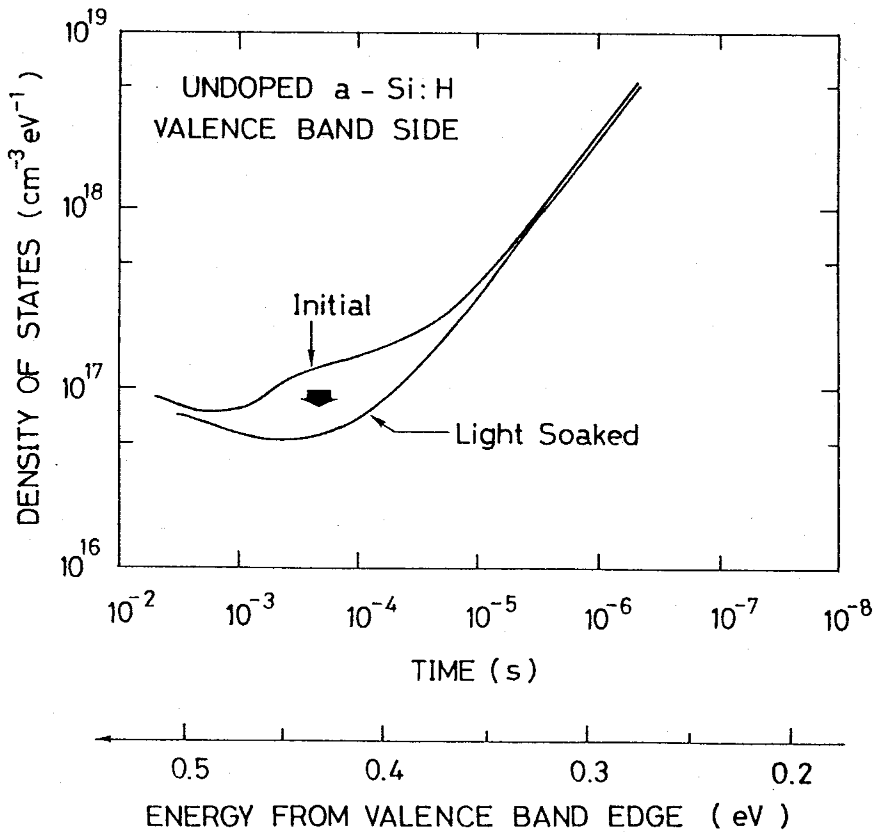

Fig.3-10. DOS distribution of the hole traps

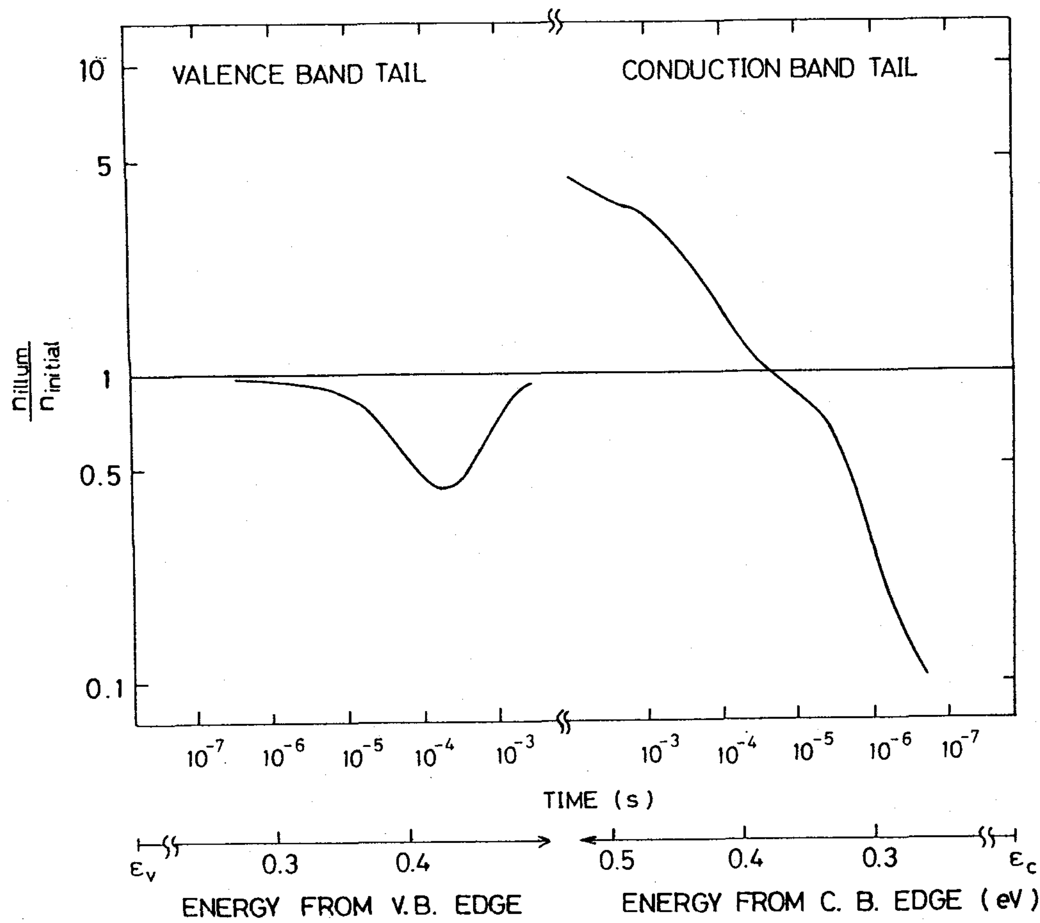

Fig.3-11. Light-induced changes in the density of states observed by the TPCS

The MPCS measurement has also been carried out on the same sample soaked with the light from a solar simulator (AM1, 100mW/cm^2). Figure 3-12 shows the MPCS spectra before and after the light soaking. This figure indicates the increases of two features of opposite sign, which indicate a hole emission signal for a positive sign and an electron emission signal for a negative sign. As described in chapter 2, this implies both the D^- center and H1 center, which are located at about 0.5eV from the conduction band and about 0.54eV from the valence band respectively, are created by the light soaking.

These observations clearly suggest creation of two kind of defect centers (D^- and H1) and disappearance of shallower states, which may be due to Si-Si weak bond, are involved in the light-induced effect. The bond breaking model associated with Si-Si weak bonds [13)14)] is likely to be applied to interpret these results.

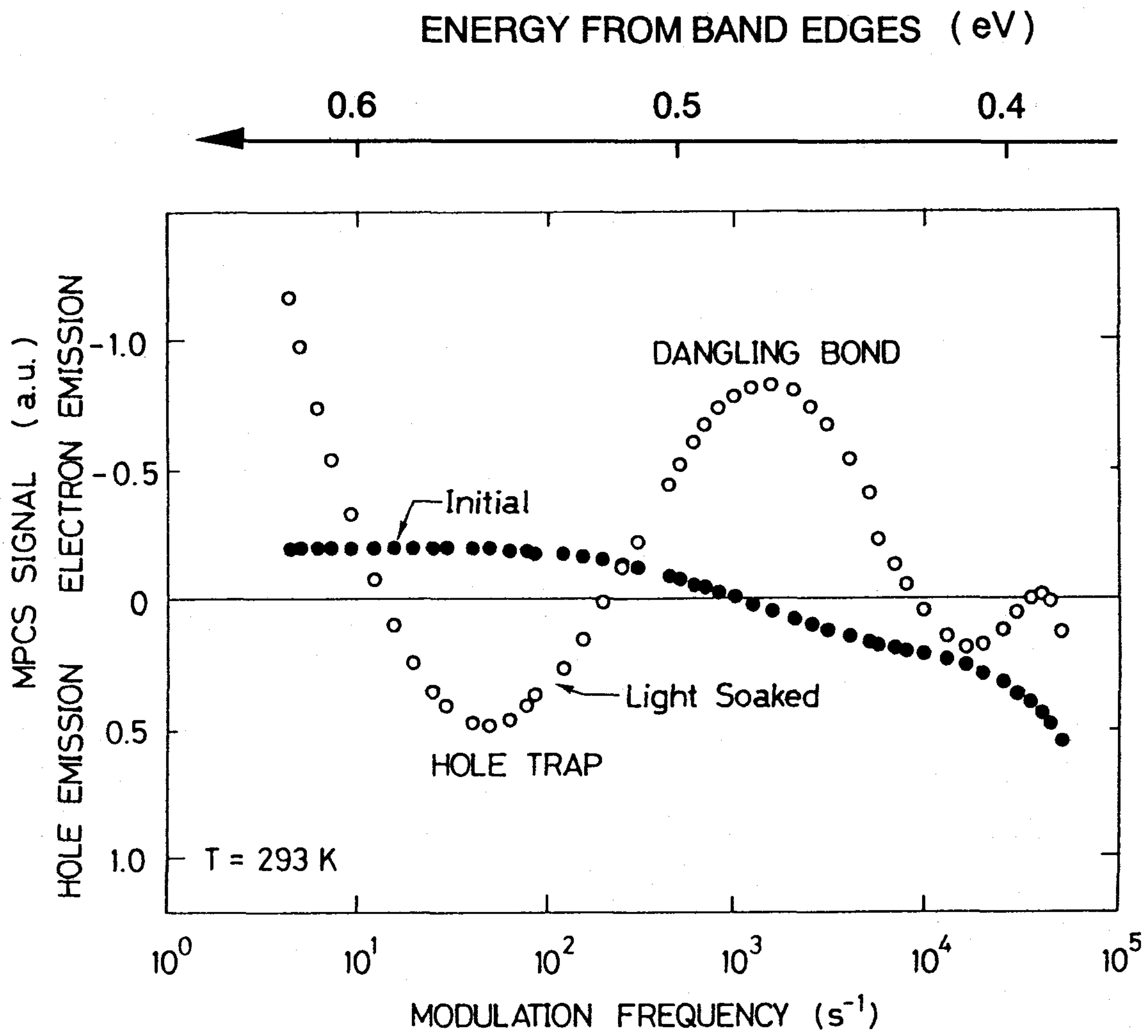

Fig.3-12. MPCS spectra before and after the light soaking.

3-4. Summary

We have applied the time-resolved photocurrent spectroscopy with a new analytical procedure to device-quality undoped a-Si:H. The TPCS analysis is proven successful to extract localized states distribution from photocurrent transients, irregardless of "pre" and "post" transit time regimes. The electron trap states at about 0.35eV below the conduction band edge and the hole trap states at 0.35-0.45eV have been observed. The origin of these newly-observed trap states has not yet been identified, however, they appear to be closely linked with carrier transport property as well as the light-induced effects.

References

(1) K.Abe, H.Okamoto, Y.Nitta, Y.Tsutsumi, K.Hattori and Y.Hamakawa, Phil. Mag. B, 58 (1988) 171.

(2) Y. Tsutsumi, K. Abe, Y. Nitta, H. Okamoto and Y. Hamakawa, Tech. Dig. International PVSEC-3, Tokyo, (1987) 675.

(3) Y. Tsutsumi, K. Uchiyama, H. Okamoto and Y. Hamakawa, Techical Digest of the International PVSEC-5, Kyoto (1990) 809.

(4) T.Tiedje and A.Rose, Solid St. Commun., 37 (1980) 49.

(5) J. Orenstein and M. Kastner, Solid St. Commun., 40 (1981) 85.

(6) Y. Tsutsumi, H. Okamoto and Y. Hamakawa, Phil. Mag. B, 60 (1988) 695.

(7) R. Kubo, J. Phys. Soc. Japan, 17 (1962) 1100.

(8) J. M. Marshall, Rep. Prog. Phys., 46 (1983) 1245.

(9) J. M. Marshall, J. Non-Cryst. Solids, 77/78 (1985) 425.

(10) G. F. Seynhaeve, R. P. Barclay, G. J. Adriaenssens and J. M. Marshall, Phys. Rev. B, 39 (1989) 10196.

(11) C. E. Nebel and G. H. Bauer, J. Non-Cryst. Solids, 114 (1989) 600.

(12) G. Schumm, K. Nitsch and G. H. Bauer, Phil. Mag. B, 58 (1988) 411

(13) I. Hirabayashi, K. Morigaki and S. Nitta, Jpn. J. Appl. Phys., 19 (1980) L357.

(14) J. I. Pankove and J. E. Berkeyheiser, Appl. Phys. Lett., 37 (1980) 705.

Chapter 4. OPTICAL ABSORPTION NEAR BAND EDGES

4-1. Introduction

Previous chapters have described the nature and the energy distribution of the localized deep states related to defects in a-Si:H alloys. This chapter presents optical absorption spectra of amorphous silicon alloys, through which information about localized band-tail states is to be extracted. The time-of-flight transient photocurrent technique 1) are often used to study the density-of-states (DOS) distribution in the band tail states of a-Si:H alloys. Quantitative information on DOS in mobility gap can also be deduced from simple optical absorption spectrum. The optical absorption spectra of a-Si:H alloys have been determined by a variety of techniques such as the transmission method, constant photocurrent method (CPM) [2)], photoacoustic spectroscopy (PAS) [3)] and photothermal deflection spectroscopy (PDS) [4)]. Although the conventional transmission method has been widely employed to determine the Tauc optical gap, it is difficult to measure the spectrum in a low optical-absorption region of $\alpha<10^3 cm^{-1}$ for the thin films of about $1\mu m$, which includes important information for the understanding of a-Si:H alloys and actually varies with the thermal history and preparation conditions. Subband-gap absorption spectroscopy, in particular PDS and CPM, have attracted considerable attention over the last few years, because both techniques are quite easy to implement and therefore very suitable as monitoring tool for process optimization. In this work, PDS technique have been used to study the localized tail-states distribution in a-Si:H alloys.

In this chapter, the author presents the optical absorption spectra of various a-Si:H alloys measured by the PDS and the conventional transmission methods. It is shown that the optical absorption spectra varies systematically with material composition and details of preparation conditions and/or thermal history.

4-2. Outline of photothermal deflection spectroscopy (PDS)

Before commencing the description of the experimental results, the author will briefly give the outline of PDS experiment. The experimental setup employed in this work is shown in

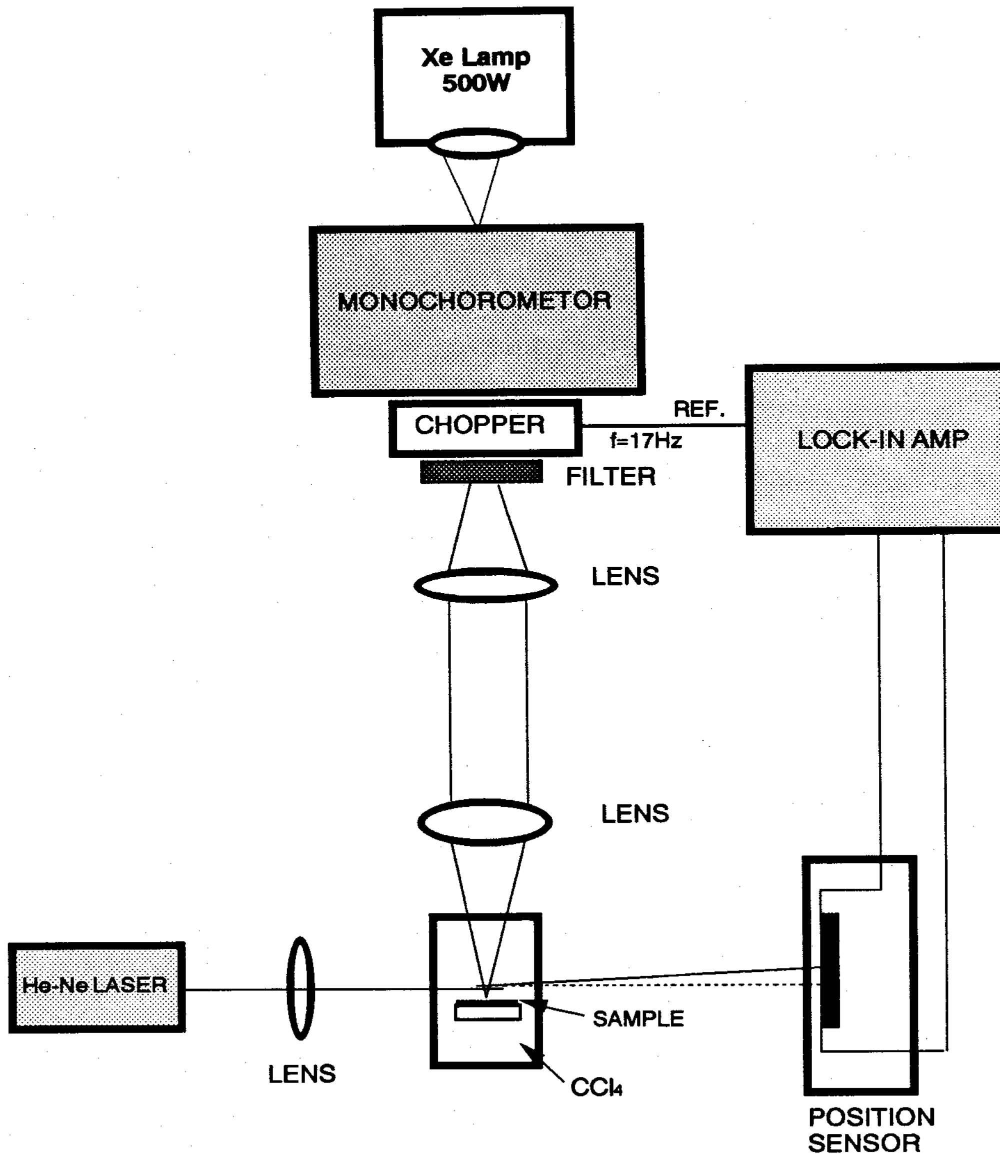

Fig. 4-1. PDS measurement system.

Fig.4-1. In the experiment, two light sources are used; a pump for heat generation and a probe for measuring the gradient of index of refraction. The pump light from 500W Xe lamp focused on the slit of a monochromator was mechanically chopped at 17Hz. A He-Ne laser with 4mW/ cm^2 was used as the probe beam. The deflection of the probe beam is measured by a position sensor. The output of the position sensor are connected by 50Ω terminator and fed into the (A-B) input of a lock-in amplifier. The amplitude of the PDS signal is then averaged and normalized to the incident light intensity.

When an intensity-modulated pump light is absorbed by a material (a-Si:H alloy), periodic heating will occur, as shown in Fig.4-1. The heat from the absorbing material flows into the surrounding medium (CCl_4) causing a corresponding modulation in the index of refraction near the material surface. A probe beam (He-Ne laser) essentially grazing the material will experience a periodic deflection synchronous with the intensity modulation. The amplitude and phase of this periodic deflection can be measured with a position sensor and a differential ac synchronous detection scheme. Thus, if the wavelength of the pump light is varied, the deflection of the probe beam becomes a measure of the optical absorption spectrum of the material of interest.

According to Jackson et. al. [4], the PDS signal S is related to the optical absorption coefficient α by

$$S \propto n^{-1} \cdot (\partial n / \partial T) \cdot I_{inc} \cdot [1 - \exp(-\alpha d)] \tag{4-1}$$

or

$$S = S_{sat}[1 - \exp(-\alpha d)]$$

for a thin film, where n is the refractive index of the surrounding medium (CCl_4), I_{inc} is the incident power of the pump light at a given wavelength λ, $\alpha=\alpha(\lambda)$ denotes the absorption coefficient and d is the film thickness of sample. The factor S_{sat} depends on geometrical parameters.

The samples employed in this work were undoped hydrogenated amorphous silicon alloys prepared on Corning 7059 glass by r.f plasma chemical vapor deposition. The substrate temperature T_s for a-Si:H was varied in the range 100-250°C. The T_s was fixed at 300°C and 250°C for a-SiGe:H and a-SiC:H alloys, respectively. For a-Si:H samples deposited at 100°C, isochronal annealing was carried out at different temperatures (100 to 400°C) for 2 hours in a vacuum (cooling rate less than 1°C/min).

4-3. Optical absorption spectra in a-Si:H alloys

A typical optical absorption spectrum of a-Si:H alloy, which was measured by the use of

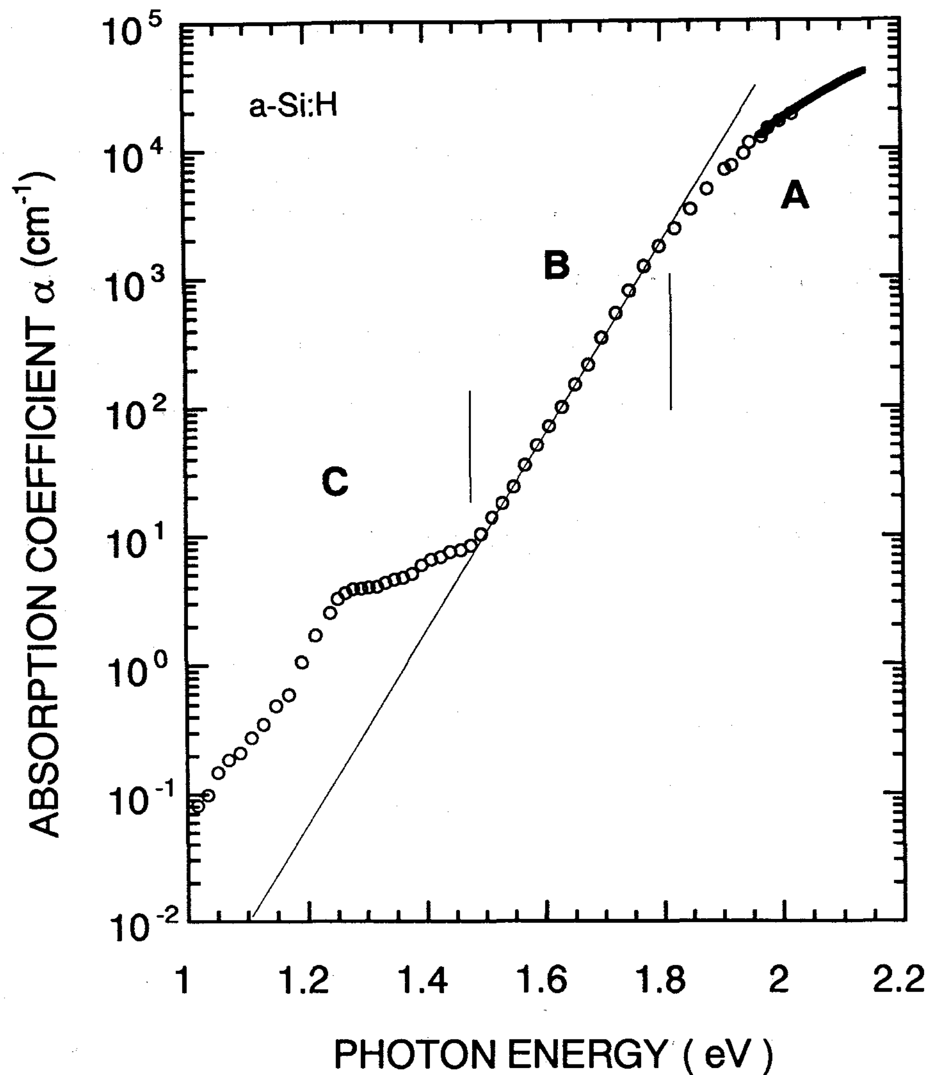

Fig. 4-2. A typical optical absorption spectrum of a-Si:H alloy, which was measured by the use of PDS and optical transmission techniques (solids line).

PDS and optical transmission techniques, is shown in Fig.4-2. As generally described by Tauc [5] and shown in Fig.4-1, the optical absorption spectrum of a-Si:H alloy can be roughly divided into the three regions of the extended-to-extended state transition region A ($\alpha > 10^3 cm^{-1}$), the exponential band tail-to-extended state region B ($10^1 < \alpha < 10^3 cm^{-1}$) and the defect-to-extended state region C ($\alpha < 10^1 cm^{-1}$).

The optical transition of A corresponds to the electron excitation from the valence band to

the conduction band. This region of a-Si:H alloys is usually described as Tauc expression:

$$(\alpha h\nu)^{1/2} = B_0(h\nu - E_g) , \tag{4-2}$$

where $h\nu$ is the photon energy, E_g is the "Tauc optical gap" and B_0 is a constant including the momentum matrix element squared and the density-of-state scale factor.

The region of B can be described by the equation

$$\alpha = \alpha_0 \exp (h\nu / E_u) , \tag{4-3}$$

where E_u is the Urbach characteristic energy, and α_0 is usually a function of it. The exponential region corresponds to transitions from the valence-band tail in the band gap, which is nearly twice as broad as the conduction band tail [1]), to the extended states in the conduction band. It is now widely accepted that these transitions are characterized by the same matrix elements as the extended-to-extended transitions, which means that the optical absorption spectra reflect the DOS distribution. E_u gives therefore a direct measure of the DOS of the localized valence band-tail states. The weak absorption region of C is attributed to the deep states in the mid-gap mostly originating from the defect and impurities.

4-3-1. Optical absorption tails in a-Si:H

Figure 4-3 shows the optical absorption spectra of undoped a-Si:H deposited at different substrate temperatures measured by PDS and conventional transmission methods. Figure 4-4 and 4-5 show the Urbach energy E_u and the content of bonded hydrogen [H], respectively, as a function of the substrate temperature T_s. [H] was measured by FTIR method. It is found that the E_u decreases with increasing T_s up to 230°C, beyond which it turns to increase. On the other hand, [H] decreases monotonically with increasing T_S. In undoped a-Si:H, where the characteristic energy of the conduction band tail is much smaller than that of the valence band tail, the Urbach energy E_u simply reflects the valence band-tail. The valence band is in thermodynamic

equilibrium during growth, so that valence band-tail corresponds to the characteristic energy of the valence band-tail states which are frozen-in during cooling from the growth temperature. The result shows that the characteristic energy of the valence band-tail states in the device-quality a-Si:H is about 54meV, which strongly depends on the substrate temperature.

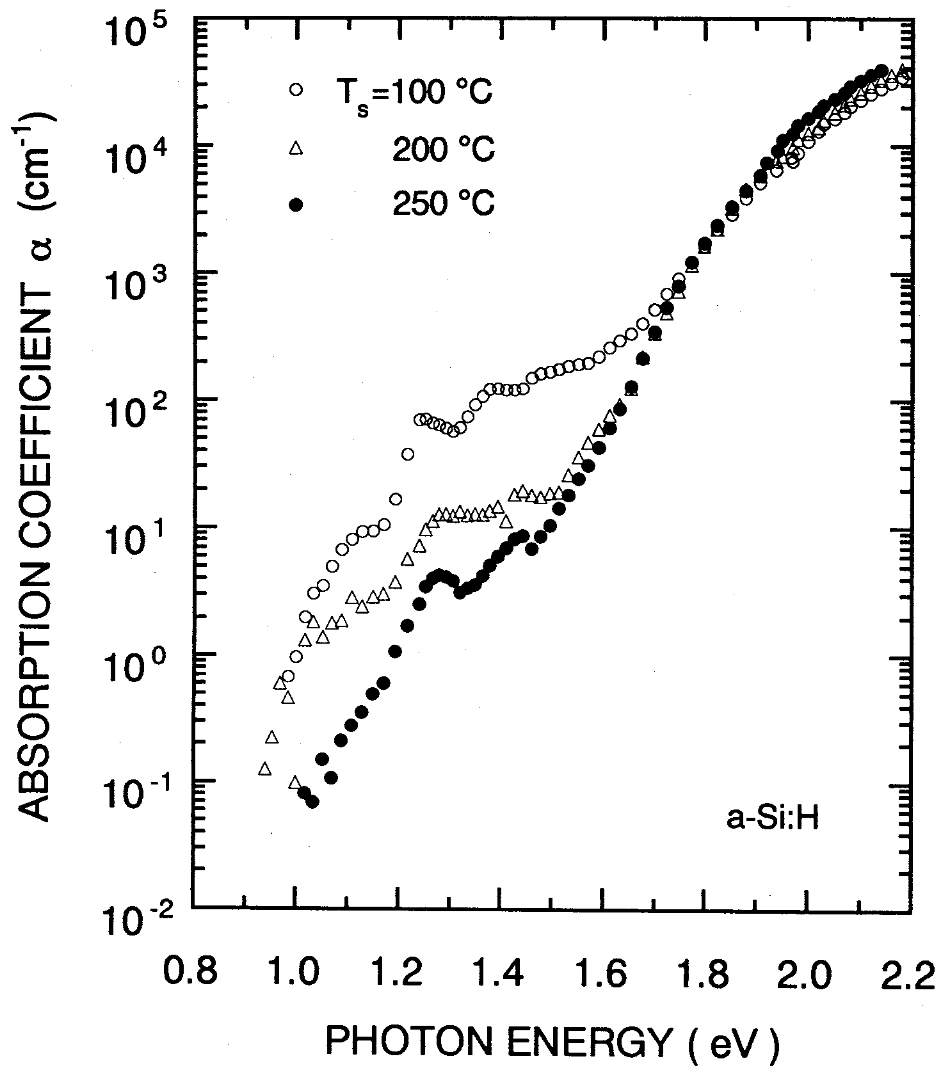

Fig. 4-3. Optical absorption spectra of undoped a-Si:H deposited at different substrate temperatures measured by PDS and conventional transmission methods.

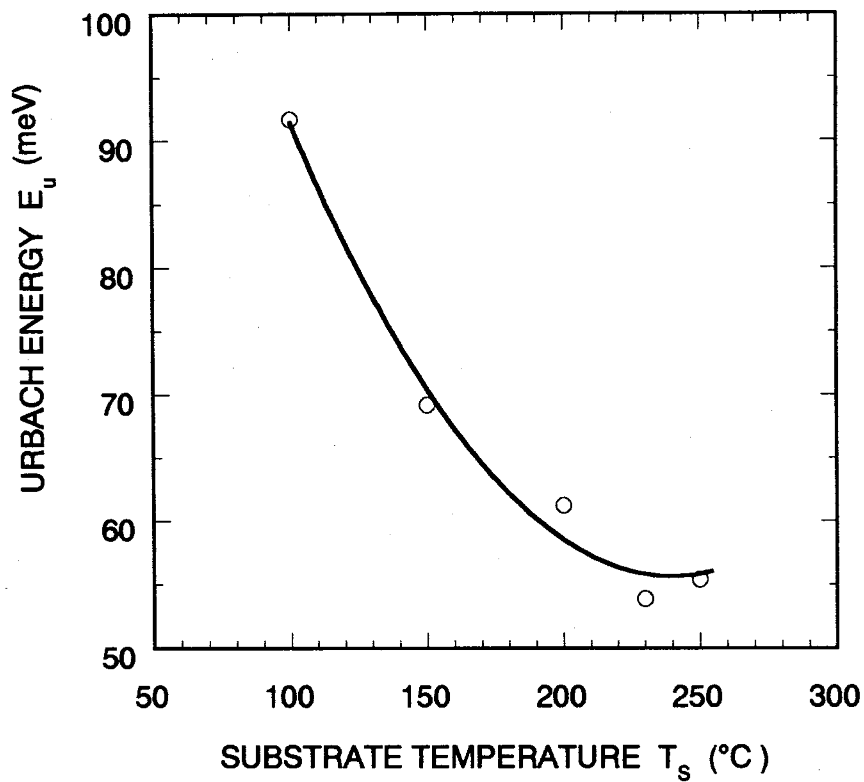

Fig. 4-4. *Urbach energy E_u as a function of the substrate temperature T_s.*

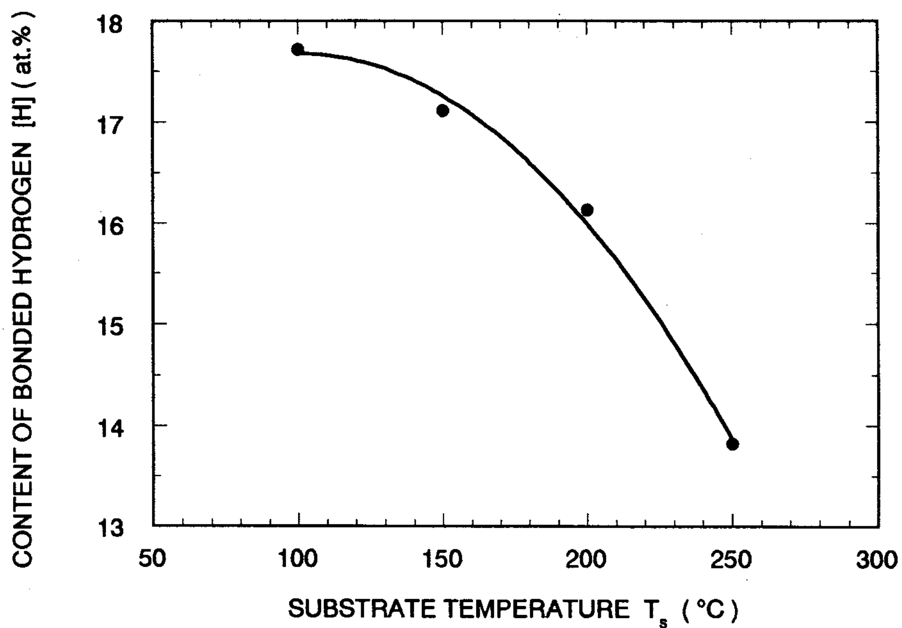

Fig. 4-5. *Content of bonded hydrogen [H] as a function of the substrate temperature T_s.*

Figure 4-6 shows the optical absorption spectra of undoped a-Si:H (deposited at 100°C) annealed at various temperatures T_a. Figure 4-7 and 4-8 shows E_u and [H] as a function of the annealing temperature T_a. As shown in the figure, the E_u decreases monotonically with increasing T_a for annealing conditions in the present study, while the [H] remains almost constant, about 17.8 at.%. The reduction of E_u might be accounted for in terms of thermal reconstruction of local bonding structures presumably mediated by hydrogen migration.

From these results, it is evident that the slope of the exponential edge depends on the

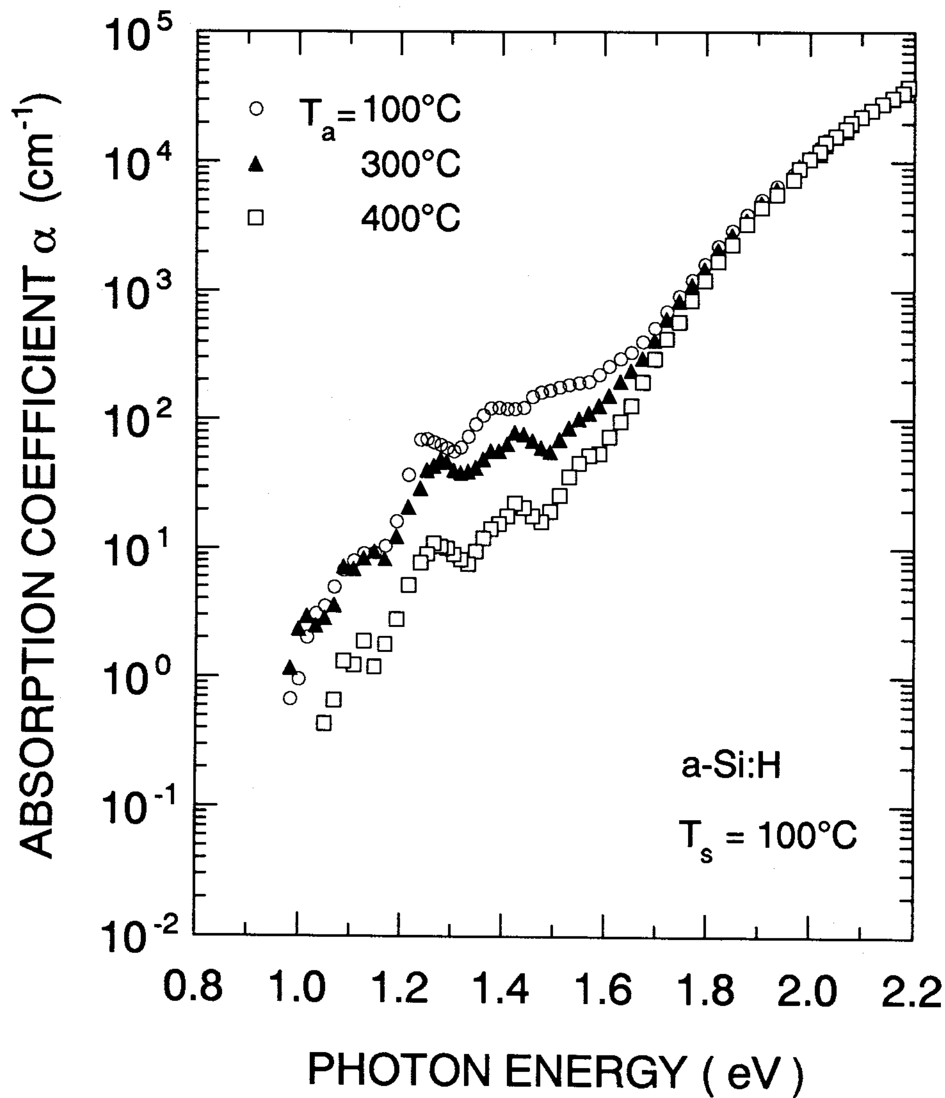

Fig. 4-6. Optical absorption spectra of undoped a-Si:H (deposited at 100°C) annealed at various temperatures T_a.

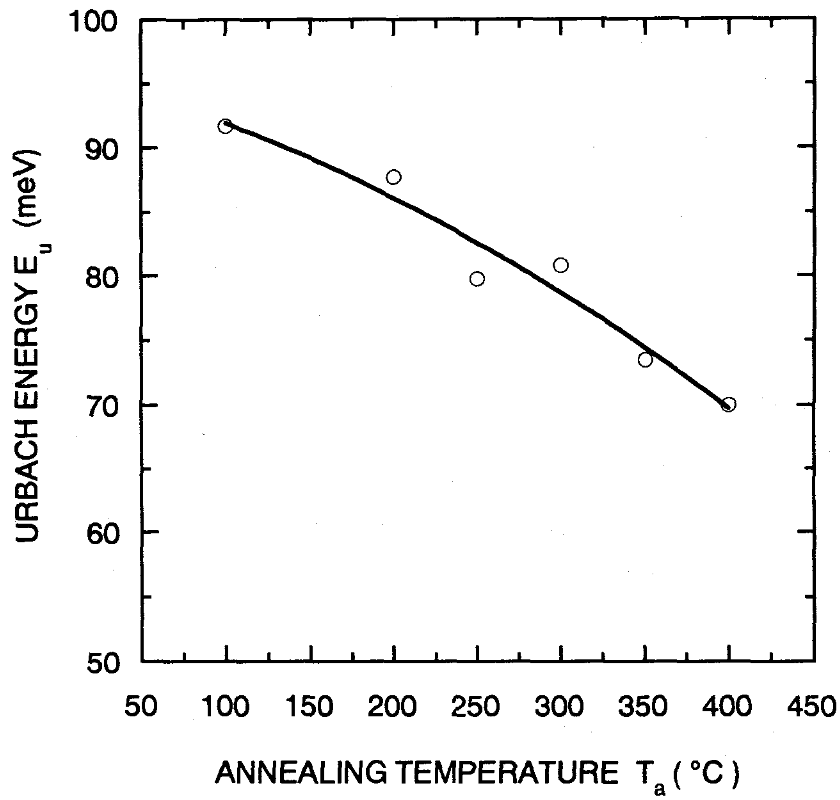

Fig. 4-7. E_u as a function of the annealing temperature T_a.

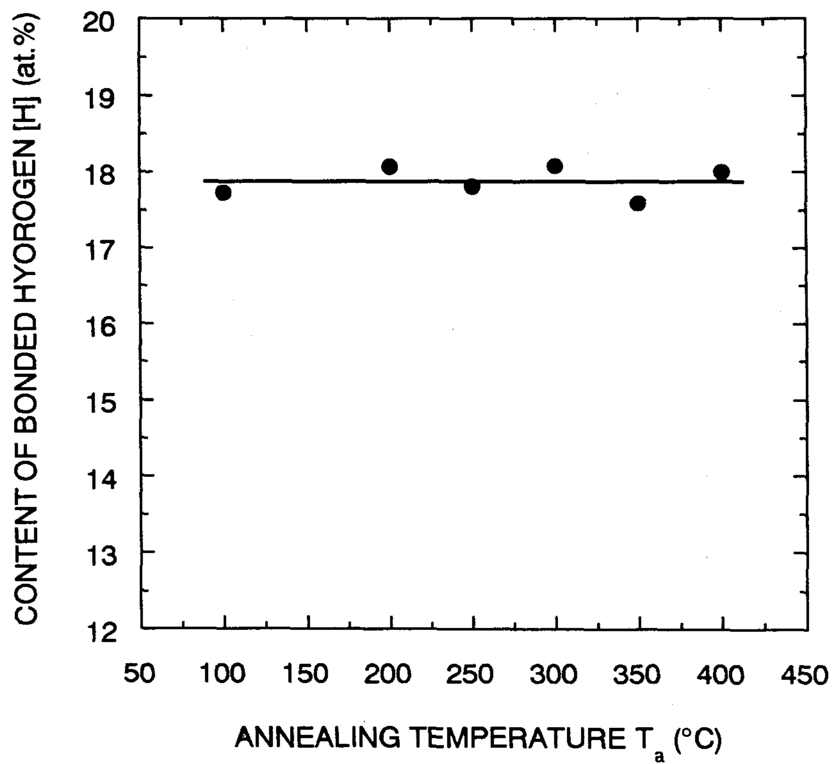

Fig. 4-8. [H] as a function of the annealing temperature T_a.

substrate temperature as well as the annealing temperature. As the weak absorption (C region), which is equivalent to the number of defects, increases, the Urbach edge broadens. The number of defects can be estimated by separating the subband gap defect absorption from the exponential band-tail absorption. The excess optical absorption $\Delta\alpha(h\nu)$ due to localized defect state absorption is given by

$$\Delta\alpha(h\nu) = \alpha(h\nu)_{meas} - \alpha_0 \exp(h\nu / E_u) \qquad (4\text{-}4)$$

The integrated absorption strength N_a give a rough estimation of the defect density the following relation ;

$$N_a = A\int \frac{\Delta\alpha(h\nu)}{h\nu} d(h\nu), \qquad (4\text{-}5)$$

where A is a proportionality constant, which is $7.9x10^{15}$ $cm^{-2}eV$ obtained according to the

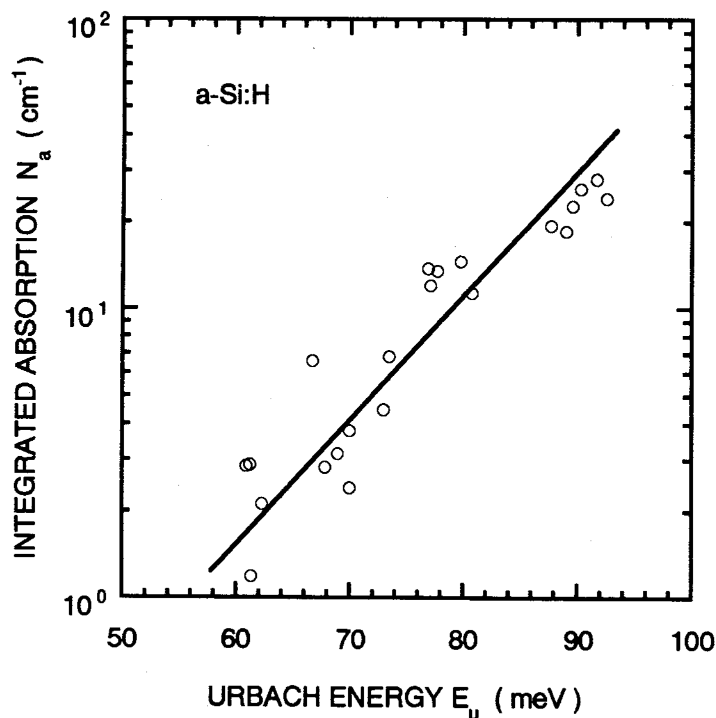

Fig. 4-9. N_a of various a-Si:H plotted against E_u.

model proposed by Jackson and Amer [4]. To test the degree of correlation between the width of the band-tail and the number of defect, N_a of various a-Si:H is plotted as a function of E_u in Fig. 4-9. A strong correlation is found to hold between these two magnitudes, suggesting that the band tails, at least same specific portion of them, may provide the "pool" of the dangling bond defects [6].

4-3-2. Optical absorption tails in a-SiGe:H and a-SiC:H

The optical absorption spectra of a-SiGe:H and a-SiC:H having the band gap energies ranging from 1.02eV to 2.08eV have been measured by the present method. The optical absorption spectra are summarized for a-Si:H alloys (a-Ge:H, a-SiGe:H, a-Si:H and a-SiC:H) of various band gaps in Fig. 4-10. Figure 4-11 shows E_u as a function of the band gap energy E_g. For

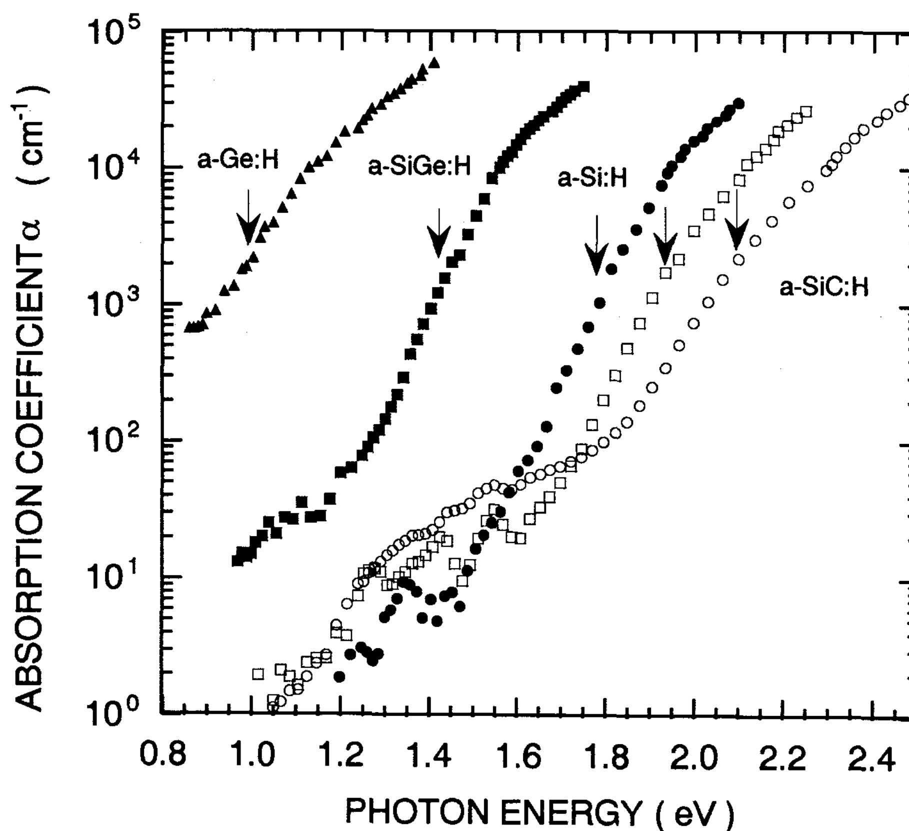

Fig. 4-10. Optical absorption spectra of a-Si:H alloys (a-Ge:H, a-SiGe:H, a-Si:H and a-SiC:H) of various band gaps

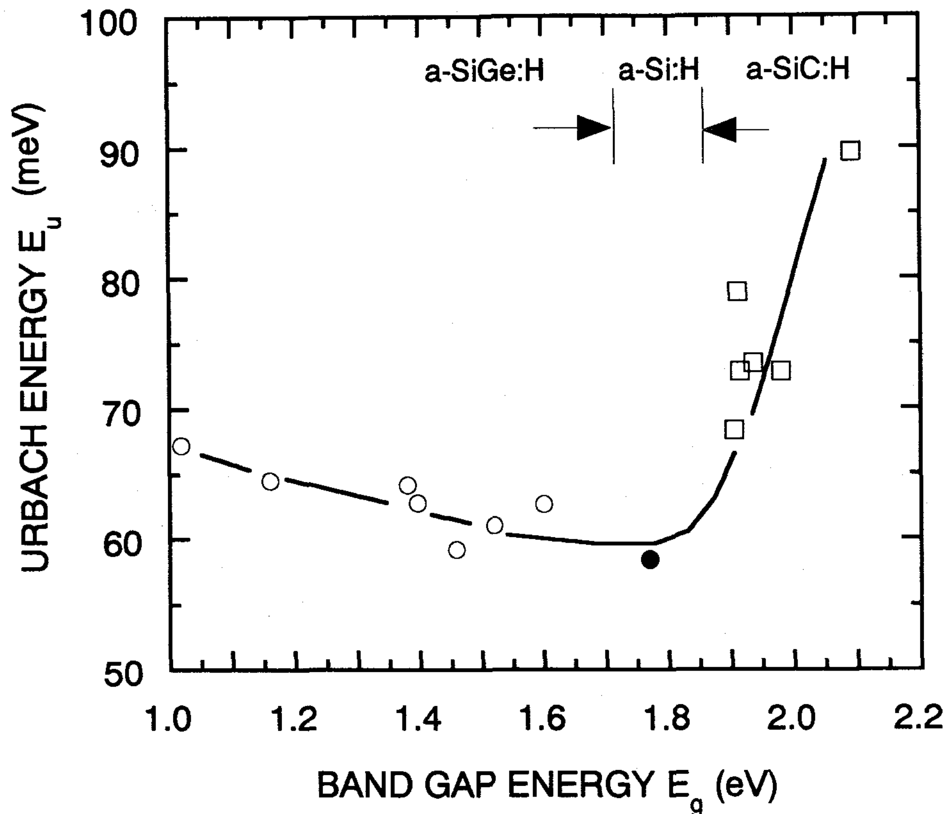

Fig. 4-11. E_u as a function of the band gap energy E_g.

the a-SiGe:H, the E_u slightly increases with decreasing the band gap energy from 1.8eV (a-Si:H), while weak absorption region increases with decreasing the band gap. On the other hand, the E_u of a-SiC:H alloys remarkably increases with increasing the band gap. The result is likely to due to the effect of alloy-induced disorder.

4-4. Summary

We have measured the optical absorption spectra of various a-Si:H alloys by the use of the PDS and conventional transmission methods and estimated the valence band tail states from the Urbach energy E_u. The result indicates that the characteristic energy of the valence band tail states strongly depends on the growth temperature, annealing temperature and alloying with Ge and C.

References

(1) T. Tiedje and A. Rose, Solid State Commun., 37 (1981) 49.

(2) M. Vanecek, J. Kocka, J. Stuchlik, Z. Kozisek, O. Stika and A. Triska, Solar Energy Materials , 8 (1983) 411.

(3) S. Yamasaki, H. Okushi, A. Matsuda, H. Oheda, N. Hata and K. Tanaka, J. Appl. Phys. Jpn., 20 (1981) L665.

(4) W. B. Jackson, and N. M. Amer, Phys. Rev. B, 25 (1982) 5559.

(5) J. Tauc, Amorphous and Liquid Semiconductors, edited by J. Tauc (Plenum Press, London and New York, 1974) p.159.

(6) Z. E. Smith and S. Wagner, Phys. Rev. B, 32 (1985) 5510.

CHAPTER 5. BAND-EDGE STATES AND CARRIER TRANSPORT PROPERTIES

1. Introduction

Electric fields applied to semiconductors alter the optical absorption spectrum in the vicinity of the fundamental absorption edge. For crystalline materials, the electroabsorption (EA) effect is well identified as arising from a field-induced mixing of the unperturbed one-electron Bloch functions occurring selectively near the originally vertical allowed transitions 1). The field-induced mixing is equivalent to spreading sharp vertical transitions over a finite range of initial and final momenta. Incorporating static disorder yields analogous but more profound effects, and provided that it is sufficiently extensive, gives rise to an apparent break-down of momentum selection rule, as is often relied to explain optical features of amorphous semiconductors [2)]. Since the disorder- and field-induced effects both operate in a competitive manner, any simple description of the EA spectrum is not possible for amorphous semiconductors. In this sense, EA spectroscopy has long been believed to be less informative for such materials in comparison to its successful utilization for studying band structures of crystalline counterparts [1)].

The situation has been changed by a recent finding of polarization-dependent EA spectra in some classes of amorphous semiconductors including hydrogenated amorphous silicon [3)]. The EA signal exhibits much larger strength when the field **F** is applied parallel to the polarization vector **e** of the light than **F** perpendicular to **e**. Understanding of the anisotropy would offer a new possibility for extracting details of the band-edge structure of amorphous semiconductors.

We have developed a low-field EA theory in which the effects of disorder are incorporated in the context of a site-disordered tight-binding (TB) model. We reached the conclusion that the polarization-dependent EA effect arises essentially from a field-induced change in the matrix element for optical transitions involving localized states near the band edge, so that it surveys as an indicator for the degree of disorder in amorphous semiconductors [4)]. In accordance with the theoretical result, we propose a new method for evaluating the carrier mean

free path and the mobility in the vicinity of band edge [5)6)]. In this chapter, the author presents an outline of the polarized EA technique as well as the result of experiments on various a-Si:H alloys. It is shown that the mobility varies systematically with material composition and details of preparation conditions and/or thermal history, although the range of variation is not so significant (less than 20%) so long as the materials studied in this work are concerned.

5-2. Polarized electroabsorption (EA) effects

Electric fields applied to semiconductor alter the optical absorption spectrum (EA effect) in the vicinity of the fundamental absorption edge, which arises from the field-induced mixing of the unperturbed one-electron wave functions [1)]. If the case of low-field limit is concerned, the EA response $\Delta\alpha$ is ascribed to the field-induced redistribution of joint density of states of initial and final states for the direct transition edge of crystalline materials. The same is valid for the EA effect associated with extended band states in amorphous semiconductors, while the feature of amorphous semiconductor manifests itself in an optional EA effect involving localized states near the band edge. The transitions between localized states are essentially forbidden in the sense that they are non-vertical in space. In the presence of external fields, an "indirect" transition would occur between localized states via extended intermediate states due to the finite field-induced coupling between localized and extended states, resulting in an increase in optical absorption. It could then be easily imagined that the strength of such an EA signal depends on the angle θ between the electric field **F** and the polarization of light **e**, whereas any polarization-dependence may vanish upon spatial averaging for the EA component common to crystalline materials. Finally, the total EA signal $\Delta\alpha(E;F,\theta)$ observed in amorphous semiconductors is represented in terms of the sum of the disorder independent term and the polarization-dependent "amorphous" term $\Delta\alpha^{(a)}(E;F)$ as,

$$\Delta\alpha(E;F,\theta) = \Delta\alpha^{(c)}(E;F) + \Delta\alpha^{(a)}(E;F) \cdot \cos^2\theta , \qquad (5\text{-}1)$$

where E denotes the photon energy. Both the EA signals appear in the Tauc optical region at

which main optical transitions may switch from those involving localized states to those between extended sates, and their signal intensities scale quadratically with the applied field F (lowest non-vanishing perturbation). Since localized states near the band edge giving rise to $\Delta\alpha^{(a)}(E;F)$ component are produced by structural disorder, the ratio $\Delta\alpha^{(a)}/\Delta\alpha^{(c)}$ should be tied with the degree of disorder in the materials, which is consequently related to the carrier mean free path and mobility near the band edge. In this section, the author presents an outline of the polarized EA theory, which is verified by means of the microscopic quantum mechanical theory based upon time-dependent Green's function procedure, as well as the experimental procedure.

5-2-1. Model and formulation

The electron system of our present concern is modeled by a two-band simple TB Hamiltonian, which consists of a regular nearest-neighbor transfer term, a site-diagonal disorder term, and a steady electric potential term with a field F applied in the $\mathbf{e}_\beta$ direction.

$$H = H^c + H^v , \tag{5-2}$$

$$H^\mu = V_\mu \sum_{i,j} |\mu i\rangle\langle\mu j| + \sum_i (v_i^\mu + eFx_i^{(\beta)}) |\mu i\rangle\langle\mu i| . \tag{5-3}$$

Here, μ (μ=c or v) denotes band index; conduction band or valence band. The notation $|\mu i\rangle$ expresses the Wannier state associated with site i belonging to the band m. The regular transfer term defines the $\varepsilon_{\mathbf{k}}^{\mu}$ dispersion-relation of the virtual crystal system. The imaginary part of the dielectric constant for the light polarization in the $\mathbf{e}_\alpha$ direction is generally written in terms of the one-particle Green's function;

$$\varepsilon_2(E) = \frac{2\pi e^2}{\hbar}\int_{-\infty}^{\infty} dt \exp\left[-\frac{E}{i\hbar}t\right] S(t) , \tag{5-4}$$

with

$$S(t) = -\left(\frac{\hbar^2}{mE}\right)\frac{2}{\Omega}\left\langle \mathrm{Tr}\left[p_\alpha g^c(t) p_\alpha g^v(-t)\right]\right\rangle$$

$$= -\hbar^2 \frac{2}{\Omega}\sum_{\mathbf{kq}}\left\langle \frac{\partial}{\partial k_\alpha} g^c_{\mathbf{kq}}(t) \frac{\partial}{\partial q_\alpha} g^v_{\mathbf{qk}}(-t)\right\rangle, \tag{5-5}$$

where E denotes photon energy, W sample volume, and <•••> indicates the ensemble average over a distribution of random site-energy v_i^μ, which is here assumed to be a Gaussian with a variance W_μ^2. Note that the momentum matrix element is taken into account in the form of d/ dk_α operator. $g^\mu(t)$ represents the one-particle Green's function;

$$g^\mu(t) = \frac{1}{i\hbar}\exp\left[\frac{H^\mu}{i\hbar}t\right]. \tag{5-6}$$

If the site-diagonal disorder variable v_i^μ has no statistical correlation for μ=c and v, the average in eqn.(5-5) is reduced to the product of averaged Green's functions. Solving an equation of motion for the averaged Green's function with the cumulant expansion procedure [7] leads to

$$\left\langle g^\mu_{\mathbf{kq}}(t)\right\rangle = \frac{1}{i\hbar}\,\delta_{\mathbf{kq}(\perp)}\,\delta(k_\beta - q_\beta + \frac{eF}{\hbar}t)\,\exp\left[\Gamma^\mu_{\mathbf{k}}(t)\right], \tag{5-7}$$

with

$$\Gamma^\mu_{\mathbf{k}}(t) = \frac{W_\mu^2}{2}\left(\frac{t}{i\hbar}\right)^2 + \frac{1}{i\hbar}\int_0^t d\zeta\left[1 + W_\mu^2\left(\frac{\zeta}{i\hbar}\right)^2\right]\varepsilon^\mu_{\mathbf{k}\perp}\left[k_\beta + \int_\zeta^t A^\mu(\zeta)d\zeta\right], \tag{5-8}$$

and

$$A^{\mu}(t) = \frac{eF}{\hbar}\left(1 + \frac{3}{2}W_{\mu}^{2}\left(\frac{t}{i\hbar}\right)^{2}\right), \tag{5-9}$$

within the context of the "small-time" approximation [8]. It follows an easy-to-handle form of the function S(t) in eqn.(5-5);

$$S(t) = \frac{2}{\Omega}\sum_{\mathbf{k}} \frac{\partial}{\partial k_{\alpha}}\Gamma_{\mathbf{k}}^{c}(t)\, \frac{\partial}{\partial k_{\alpha}}\Gamma_{\mathbf{k}}^{v}(-t)\, \exp\left[\Gamma_{\mathbf{k}}^{c}(t)+\Gamma_{\mathbf{k}}^{v}(-t)\right]. \tag{5-10}$$

5-2-2. Low-field EA effects

We focus on the field-induced change in $\varepsilon_2(E)$ in the low-field limit, which becomes valid for $eFa \ll (E_X/\langle V\rangle)^{1/2}W$, where a denotes an average interatomic spacing, E_x the energy gap of the given virtual-crystal system, and $\langle V\rangle=(V_C+V_V)/2$. In this limit, $\Gamma_{\mathbf{k}}^{\mu}$ in eqn.(5-8) may be written to a good approximation;

$$\Gamma_{\mathbf{k}}^{\mu}(t) = \left(\frac{t}{i\hbar}\right)\varepsilon_{\mathbf{k}}^{\mu} + \left(\frac{t}{i\hbar}\right)^{2}\frac{W_{\mu}^{2}}{2} + \left(\frac{t}{i\hbar}\right)^{3}\frac{W_{\mu}^{2}}{3}\varepsilon_{\mathbf{k}}^{\mu}$$

$$- \frac{(eF)^{2}}{24}\frac{\partial^{2}\varepsilon_{\mathbf{k}}^{\mu}}{\partial k_{\beta}^{2}}\left(\frac{t}{i\hbar}\right)^{3} + i\frac{7}{24}(eF)W_{\mu}^{2}\frac{\partial\varepsilon_{\mathbf{k}}^{\mu}}{\partial k_{\beta}}\left(\frac{t}{i\hbar}\right)^{4}. \tag{5-11}$$

Then, $\varepsilon_2(E)$ in the presence of an electric field is readily calculated via eqn.(5-10), yielding three dominant terms of which the latter two terms describe the field-induced change in $\varepsilon_2(E)$;

$$\varepsilon_2(E; 0) = I_0(E)\,, \tag{5-12}$$

$$\Delta\varepsilon_2^{(c)}(E;F) = \eta_F I_3(E) , \tag{5-13}$$

$$\Delta\varepsilon_2^{(a)}(E;F) = \frac{49}{24}(W_c W_v)^2 \eta_F \left(\cos\theta_{\alpha\beta}\right)^2 I_7(E) , \tag{5-14}$$

$$\eta_F = \frac{(eF)^2}{24}\frac{\partial^2 \varepsilon_{\mathbf{k}}^{cv}}{\partial k_\beta^2} = \frac{(eFa)^2}{12}\left(V_c+V_v\right), \tag{5-15}$$

$$I_n(E) = (-1)^{n+1}\frac{4\pi e^2}{\hbar}\left(\frac{V_c V_v}{V_c+V_v}\right)a^2\int_{-\infty}^{\infty} dt \exp\left[-\frac{E}{i\hbar}t\right]\left(\frac{t}{i\hbar}\right)^{n+1}$$

$$\times\frac{2}{\Omega}\sum_{\mathbf{k}}\exp\left[\Gamma_{\mathbf{k}0}^{cv}(t)\right], \tag{5-16}$$

and

$$\Gamma_{\mathbf{k}0}^{cv} = \left(\frac{t}{i\hbar}\right)\varepsilon_{\mathbf{k}}^{cv} + \left(\frac{t}{i\hbar}\right)^2\frac{W_c^2+W_v^2}{2} + \left(\frac{t}{i\hbar}\right)^3\frac{W_c^2\varepsilon_{\mathbf{k}}^c - W_v^2\varepsilon_{\mathbf{k}}^v}{3} , \tag{5-17}$$

where $\theta_{\alpha\beta}$ denotes the angle between **F** and **e**, $\varepsilon_{\mathbf{k}}^{cv}=\varepsilon_{\mathbf{k}}^{c}-\varepsilon_{\mathbf{k}}^{v}$, and the isotropic parabolic band-edge is assumed to have an effective mass $\hbar^2/2V_\mu a^2$. The second term $\Delta\varepsilon_2^{(c)}(E;F)$ has a perfect coincidence with the "third-derivative" EA term well known in crystalline materials [9], while the presence of disorder manifests itself in the third term $\Delta\varepsilon_2^{(a)}(E;F)$ which varies with the polarization angle as $\cos^2\theta_{\alpha\beta}$.

As is easily read from eqns.(5-10) and (5-11), the anisotropic "amorphous" term arises

in principle from the field-induced change in the transition matrix element, whereas the disorder independent term originates from the field-induced redistribution of electron-states involved in optical transitions. A set of simple equations (5-12)-(5-14) offers a visual interpretation of the polarization-dependent EA effects 3) observed for materials in which structural disorder is likely significant. For $\Delta\varepsilon_2$ or $\Delta\varepsilon_2/\varepsilon_2$ spectrum, a single positive peak appears to occur near the Tauc optical region, decaying with algebraic functions as $|E-E_x|$ away from the peaks. More quantitative aspect will be discussed in the next section, particularly on the polarization angle dependence of the EA signal amplitude.

5-2-3. Quantitative aspects of EA effects

Our prime interest in this work is to extract from the polarization-dependent EA effects, information about band-edge parameters such as mean-free paths ℓ_μ at the relevant band edges (ℓ_v and ℓ_c at the valence and conduction band edges respectively).

$$\bar{\ell}_\mu = \ell_\mu/a = 4\pi\left(V_\mu/W_\mu\right)^2 . \tag{5-18}$$

For this purpose, it would be convenient to express the amplitude ratio of the field-parallel ($\theta_{\alpha\beta}=0$) and field-perpendicular ($\theta_{\alpha\beta}=\pi/2$) EA peaks in terms of unknown parameters ℓ_μ alone;

$$\Delta\alpha_{\parallel}/\Delta\alpha_{\perp} \cong \Delta\varepsilon_{2\parallel}/\Delta\varepsilon_{2\perp} = 1 + \Delta\varepsilon_2^{(a)}/\Delta\varepsilon_2^{(c)}$$
$$= 1 + \frac{98}{3}\pi^2\left(\sqrt{\bar{\ell}_c}+\sqrt{\bar{\ell}_v}\right)^{-4} . \tag{5-19}$$

Here, a probable variation of the refractive index with photon energy and/or electric field is ignored, as is also the minor difference in the EA peak position between the field-parallel and field-perpendicular cases

Also formulated with ℓ_μ alone is the normalized average dipole-matrix element squared

$R^2(E)$, introduced by Jackson et al. [10];

$$R^2(E) = \frac{N\hbar}{2\pi e^2} I_0(E) / \frac{2}{\Omega} \int_{-\infty}^{\infty} dt \exp\left(-\frac{E}{i\hbar}t\right) \sum_k \exp\left[\Gamma^c_{ko}(t)\right] \sum_k \exp\left[\Gamma^v_{ko}(-t)\right]$$

$$= 8\pi^{3/2} a^2 \left(\ell_c \ell_v\right)^{5/4} \left(\sqrt{\ell_c} + \sqrt{\ell_v}\right)^{-5} \times \left[1 + 2\pi\left(\sqrt{\ell_c} + \sqrt{\ell_v}\right)^{-2}\right] \qquad (5\text{-}20)$$

for the Tauc optical region. Here, $N=\Omega/a^3$. Precisely speaking, $R^2(E)$ has a finite energy-dependence, particularly when going away from E_X. However, it would be safe to regard $R^2(E)$ as a constant given in the above equation since the energy-dependence turns out to be not so substantial in the spectral region of interest here. It is worthwhile noting that the average dipole matrix element, $R^2(E)$, amounts to 10.1Å^2 in the limiting case of $\ell_\mu >> a$, that is encountered in ordered crystal systems. This number is in an excellent agreement with that observed near the direct-transition edge for crystalline silicon [10].

Equations (5-19) and (5-20) suggest that measuring the EA oscillation amplitude, which we denotes $\Delta\varepsilon_2^{(a)}/\Delta\varepsilon_2^{(c)} \cong \Delta\alpha^{(a)}/\Delta\alpha^{(c)}$, permits us to determine the separated values of ℓ_c and ℓ_v if we rely on the experimental result 10Å^2 for the normalized average dipole-matrix element squared for the Tauc optical region [10]. Once the mean free path is achieved, it can be translated into carrier mobility near the band edge via an approximate relation [11].

$$\mu \approx 0.072 \times [\ell(\text{Å})]^2 \, (\text{cm}^2/\text{Vs}), \qquad (5\text{-}21)$$

when we take a=2.35 Å [12]. Note that this expression is valid for the mean free path in the range $1 < \ell/a < 6$, otherwise the mobility depends both on the magnitude of transfer energy V as well as on temperature.

5-2-4. Experimental details

Figure 5-1 illustrates the experimental set-up of the polarized EA measurement. Sinusoidal electric fields F modulated with a frequency f, were applied parallel to the sample surface with the use of evaporated Al coplanar contacts spaced by 0.3mm. The sample, of thickness around 1μm, was illuminated with monochromatic light through a polarizer, with which the light polarization angle θ was rotated with respect to the field direction. The intensity of the transmitted light T was kept constant for each polarizer angle to exclude possible effects of light intensity on the EA signal. The transmission T and its field-induced change ΔT were monitored by using a Si-photodiode and a lock-in amplifier tuned to twice the field-modulation frequency. The modulation frequency f was set above 0.1 kHz so that the thermal effects due to Joule

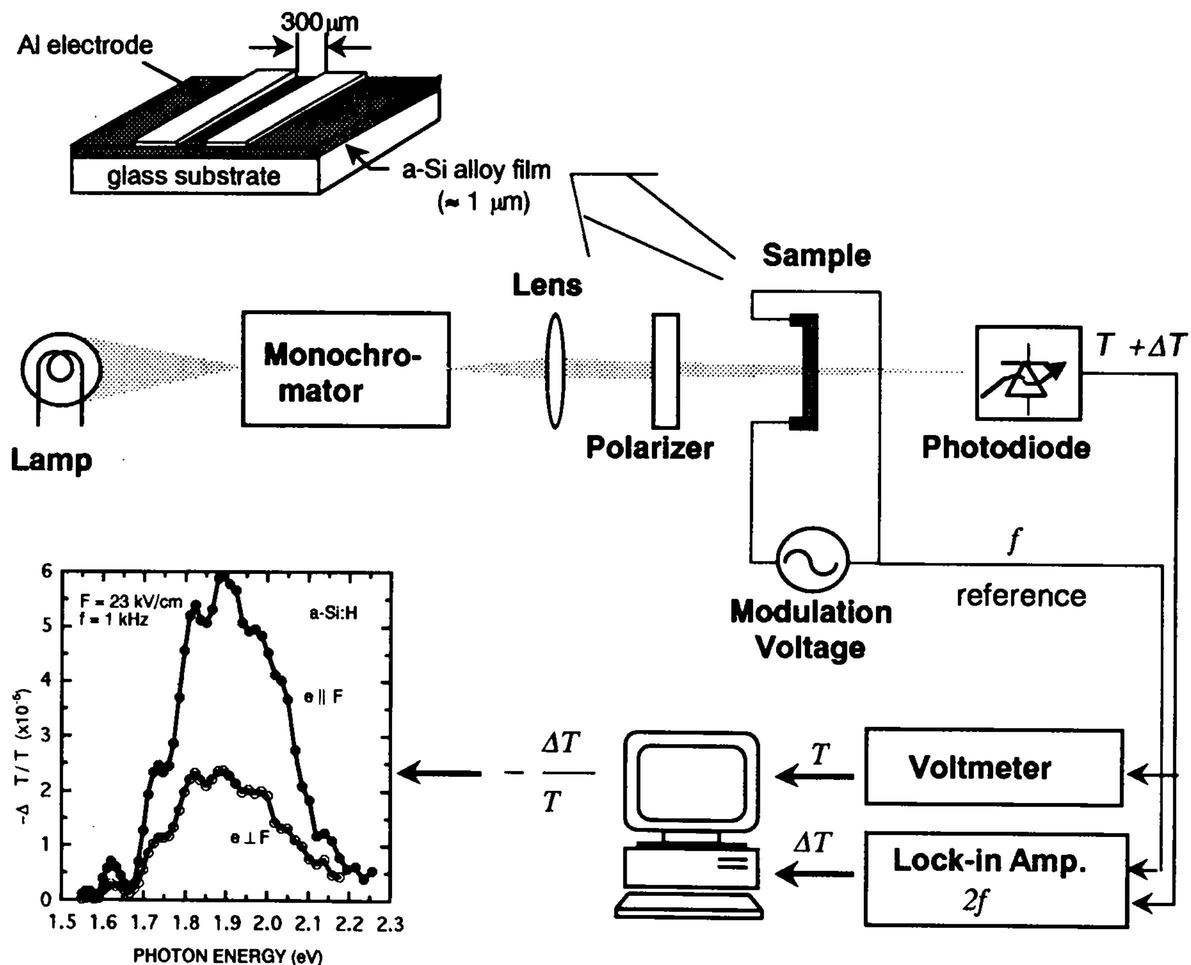

Fig. 5-1. Schematic view of experimental set-up, with a typical -ΔT/T spectrum of undoped a-Si:H.

heating can be well eliminated, which was ensured by a signal intensity being independent on the modulation frequency for f >0.1 kHz.

Also shown in Fig.5-1 is a typical $-\Delta T/T$ spectrum of undoped a-Si:H measured under the condition F=23 kV/cm, f=1 kHz. The field-induced change in the absorption coefficient $\Delta\alpha$ of our central concern is given by a standard relation

$$\Delta\alpha=-(1/d)(\Delta T/T) \tag{5-22}$$

where d is the film thickness.

The samples employed in this work were undoped hydrogenated amorphous silicon alloys prepared by r.f plasma chemical vapor deposition from SiH_4/H_2 mixture including desired amount of GeH_4 (a-$Si_{1-x}Ge_x$:H alloys; x=0-52 at.%) or CH_4 (a-$Si_{1-x}C_x$:H alloys; x=0-10 at.%). The deposition temperature T_d for a-Si:H was varied in the range 100-250°C with keeping the deposition rate at around 2.5 Å/sec, while it was fixed at 300°C for a-SiGe:H and 250°C for a-SiC:H. The content of bonded hydrogen [H], which is measured by FTIR method, decreases monotonically from 17.8 at.% to 13.8 at.% as T_d increases from 100°C to 250°C. For a-Si:H samples deposited at 100°C, isochronal annealing was carried out at different temperatures (100 to 400°C) for 2 hours in a vacuum (cooling rate less than 1°C/min). Any change was not detected in the hydrogen content in the materials for a series of annealed a-Si:H samples. The polarized EA measurement was applied to these four sets of a-Si:H alloys.

5-3. General feature of polarized EA

Typical EA spectra $\Delta\alpha$ of undoped a-Si:H (Tauc optical band gap; Eg=1.77 eV) at room temperature are shown in Fig.5-2, where the absorption spectrum measured by means of standard transmission and photothermal deflection spectroscopy (PDS) techniques is also given for comparison. A broad EA peak occurs near the Tauc optical gap (indicated by an arrow), while the signal intensity appears to be larger in the case of $F \parallel e$ than $F \perp e$. Figure 5-3 (a) shows the electric field dependence of $\Delta\alpha$ signal intensity. It is found that $\Delta\alpha$ increases proportionally

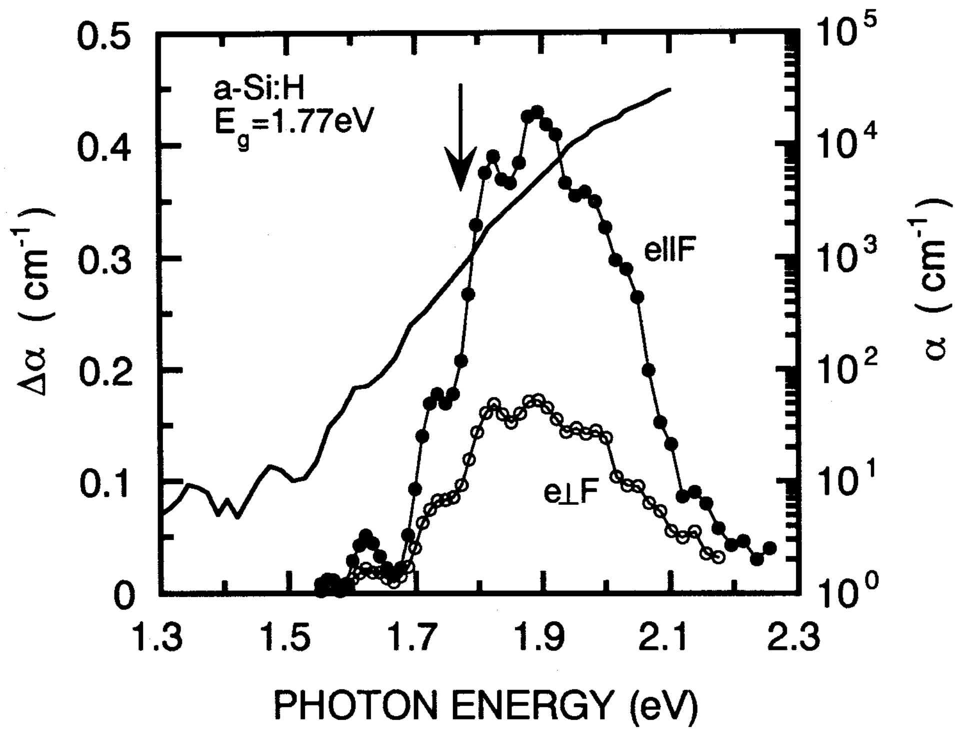

Fig. 5-2. EA spectrum $\Delta\alpha$ of a-Si:H (Eg=1.77 eV), where the absorption spectra α has been measured by means of standard transmission and PDS techniques.

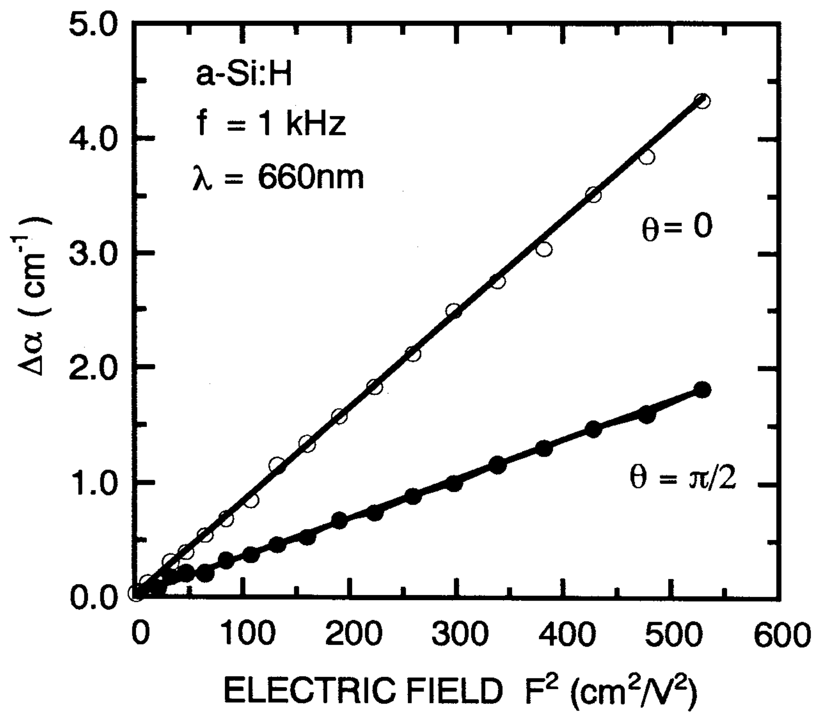

Fig. 5-3 (a). $\Delta\alpha$ of a-Si:H near peak energy of EA signal plotted against electric field F^2, where θ=0 for F//e and $\theta=\pi/2$ for F⊥e.

with the square of applied electric field. Shown in Fig.5-3 (b) is the frequency-dependence of $\Delta\alpha$ signal intensity near the peak energy of the polarized EA signals. As found in this figure, the both EA signal intensities are constant for f>0.1kHz, while they tend to decrease for f>3kHz due to the limitation of the voltage source used in the present experiment. This indicates that the modulation frequency of 1kHz may be sufficiently high to minimize thermo-modulation effects. The polarization dependence of $\Delta\alpha$ for undoped a-Si:H is demonstrated in Fig.5-4, where $\theta=0$ and $\pi/2$ refer to F‖e and F⊥e, respectively. These behaviors are fully consistent with those suggested from the theoretical prediction described in previous section.

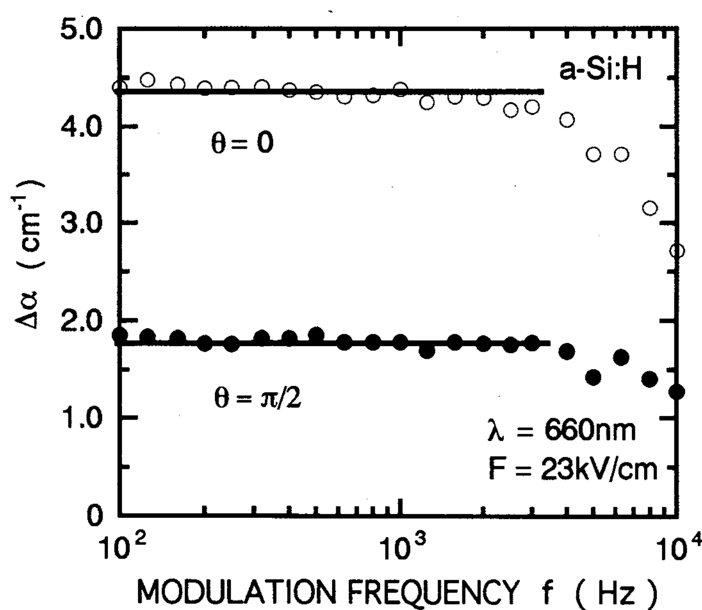

Fig. 5-3 (b). Frequency-dependence of $\Delta\alpha$ near peak energy of the polarized EA signal.

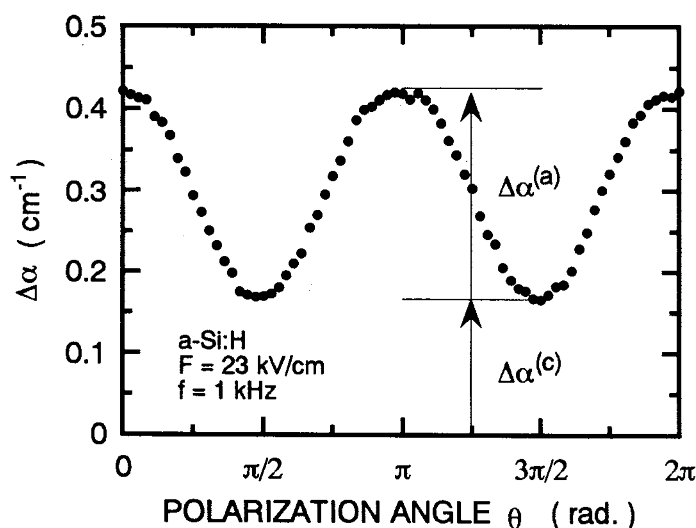

Fig. 5-4. Polarization-angle dependence of $\Delta\alpha$ for undoped a-Si:H, where $\theta=0,\pi$ for F‖e and $\theta=\pi/2$ for F⊥e.

5-4. Structural disorder and carrier mobility

Carrier mobility is one of the fundamental physical quantities which have great impacts on the device performance. In this regard, the knowledge of the carrier mobility is indispensable for the refinements of material processing as well as device design. However, for amorphous semiconductors including amorphous silicon alloys which are of great interest, no simple means have been available for the direct measurement of the free carrier mobility, instead it is conventionally deduced from the temperature dependence of the TOF drift mobility. In this section, the author describes the mean free path and the free carrier mobility near the band edge measured by polarized electroabsorption (EA) spectroscopy and presents how its magnitude is influenced by material composition, preparation conditions and/or various treatments after preparation.

5-4-1. Effect of deposition temperature in a-Si:H

Figure 5-5 shows the ratio $\Delta\alpha^{(a)}/\Delta\alpha^{(c)}$ read from the data as in Fig.5-4 as a function of the

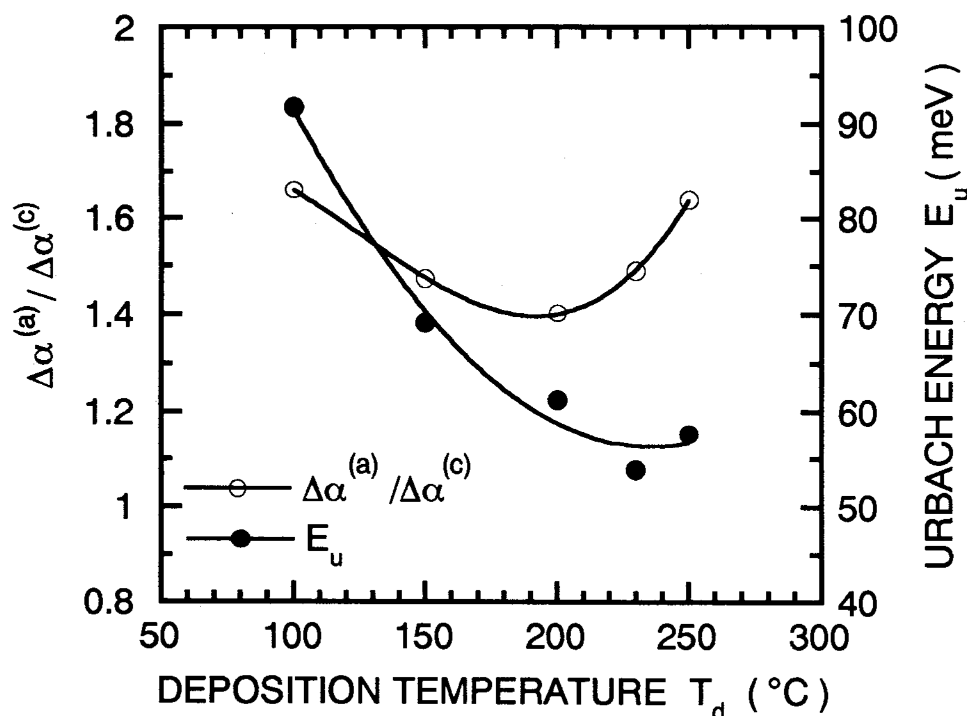

Fig. 5-5. Ratio $\Delta\alpha^{(a)}/\Delta\alpha^{(c)}$ and Urbach energy E_u plotted against deposition temperature T_d.

deposition temperature T_d. For comparison, the variation of the Urbach energy E_u is also given in this figure, which is another physical quantity closely linked with the degree of disorder. It is found that the $\Delta\alpha^{(a)}/\Delta\alpha^{(c)}$ decreases with increasing T_d up to 200°C, beyond which it turns to increase. A similar behavior is observed for E_u, although the minimum of E_u occurs at slightly higher temperature, 230°C. We stress here the ratio $\Delta\alpha^{(a)}/\Delta\alpha^{(c)}$ holds a fundamental advantage over E_u as a measure of disorder, since it can be directly related to the carrier mean free path ℓ and free carrier mobility μ through eqns. (5-19) and (5-21), whereas E_u depends also on the density-of-states near the band edge.

The normalized mean free paths $\bar{\ell}_c$ and $\bar{\ell}_v$ at the conduction and valence band edges, respectively, evaluated through combining eqns. (5-19) and (5-20), and plotted against the deposition temperature T_d in Fig.5-6. Immediately read from the figure is that the highest mean free path (about 12.5Å for electrons, and 5.5Å for holes) occurs for undoped a-Si:H deposited at

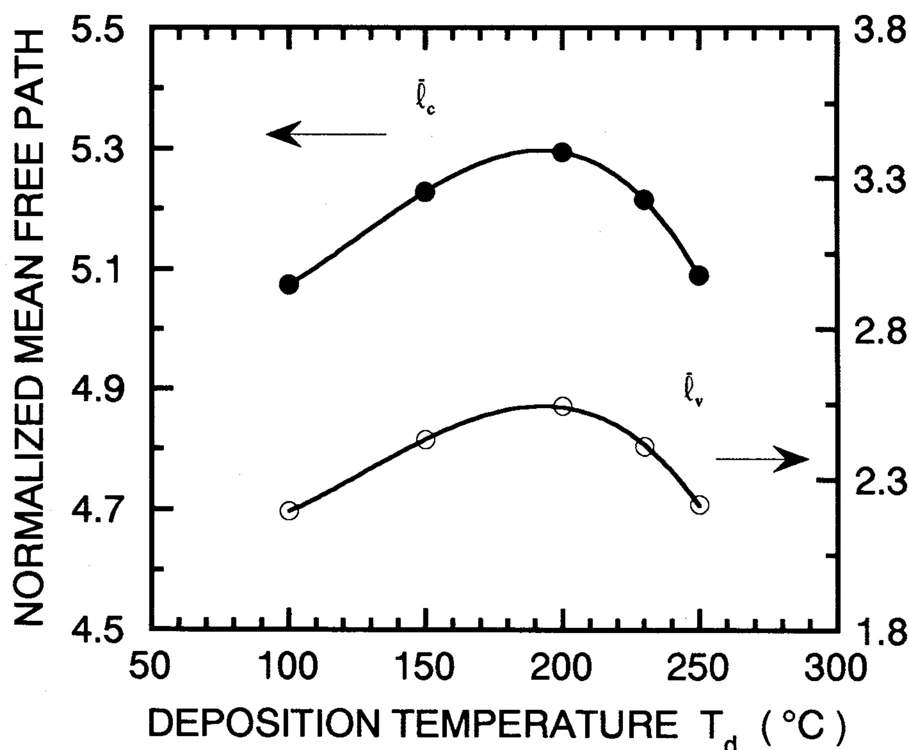

Fig. 5-6. Normalized mean free paths $\bar{\ell}_c$ and $\bar{\ell}_v$ at the conduction and valence band edge plotted against deposition temperature T_d.

T_d=200°C. Here, an average interatomic spacing "a" is set at 2.35Å, being independent of [H] from 5 to 20 at.% [12]. The range of the mean free path for electrons in undoped a-Si:H coincidences with that estimated from the subband absorption of a-Si/a-SiC quantum well systems [13], and does not contradict with current understanding of transport properties, including the anomalous Hall effect [11].

The central issue here is an evaluation of free carrier mobility which is hardly accessed by conventional means. The mean free path in Fig.5-6 is converted into free carrier mobility through eqn.(5-21), which is plotted in Fig.5-7 again as a function of T_d. The electron mobility reaches about 11.2 cm^2/Vs for undoped a-Si:H deposited at T_d=200°C, while the hole mobility is roughly 20% of that for electrons. These numbers are in good agreements with those deduced from TOF related measurements [14].

A fundamental question arises why the carrier mobility attains maximum for a specific

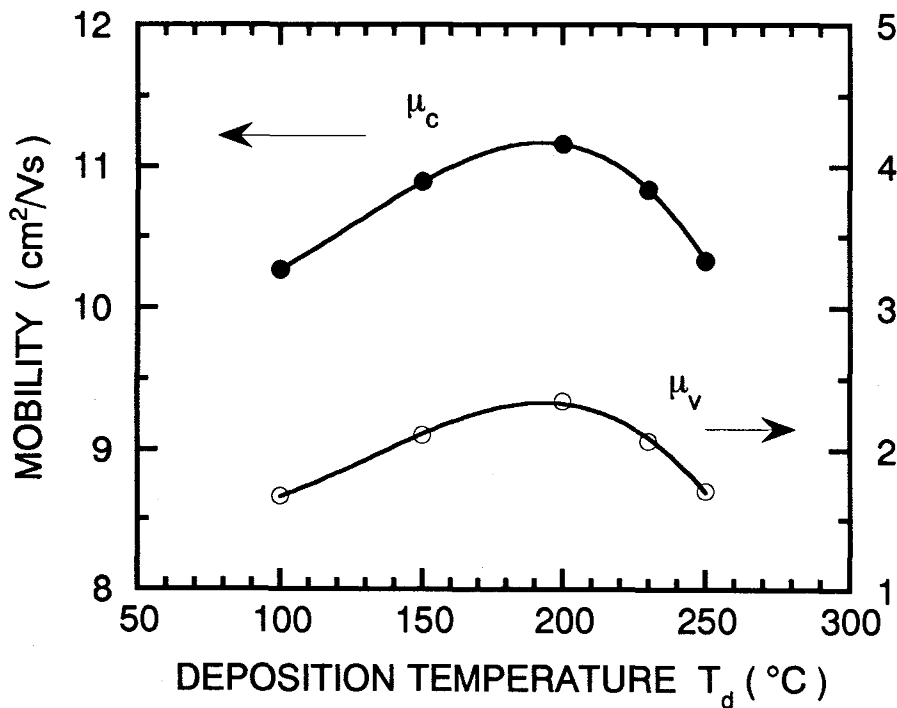

Fig. 5-7. Electron mobility μ_c and hole mobility μ_v as a function of deposition temperature T_d.

deposition temperature. The magnitude of room-temperature mobility is essentially governed by the structural disorder involved in the materials. The structural disorder is likely to be determined by the extent of structural relaxation occurred during the growing process for the low temperature deposition case, while for high temperature deposition case it would be dominated by the thermal disorder which is to be frozen-in during the cooling process after deposition. These two competing mechanisms would operate to yield a mobility maximum at a particular deposition temperature. It should be remarked here that the optimum deposition temperature "200°C" found in the present experiment can never be a universal quantity characteristic of plasma CVD a-Si:H, but it should be largely dependent on some details of deposition conditions, i.e., deposition rate, flux and energy of plasma species including ions impinging on growing surface, cooling rate after deposition and so on.

5-4-2. Effect of thermal annealing in undoped a-Si:H

As mentioned in the former section, the mobility is considered to be determined by structural disorder arising from insufficient structural relaxation during deposition of a-Si:H alloys deposited at low temperatures. It is then of some interest to investigate how such structural disorder is relieved by thermal annealing treatment. Figure 5-8 shows the ratio $\Delta\alpha^{(a)}/\Delta\alpha^{(c)}$ and E_u measured on a-Si:H (deposited at 100 °C) annealed at various temperatures T_a. The content of bonded hydrogen [H] stays constant, about 17.8 at.%, for annealing conditions in the present study. This figure indicates that both the ratio $\Delta\alpha^{(a)}/\Delta\alpha^{(c)}$ and E_u decrease monotonically with increasing T_a, in contrast to the tendency found in deposition temperature dependence. The decrease in the ratio $\Delta\alpha^{(a)}/\Delta\alpha^{(c)}$ and E_u, that is structural disorder, might be accounted for in terms of thermal reconstruction of local bonding structures presumably mediated by hydrogen migration. The reduction in the structural disorder is reflected in an improvement of carrier mobilities as shown in Fig.5-9. With annealing treatment at the highest temperature, 400 °C, both the electron and hole mobilities reach the level achieved by our optimum deposition temperature, although the hydrogen content and Tauc optical band gap are largely different for each other.

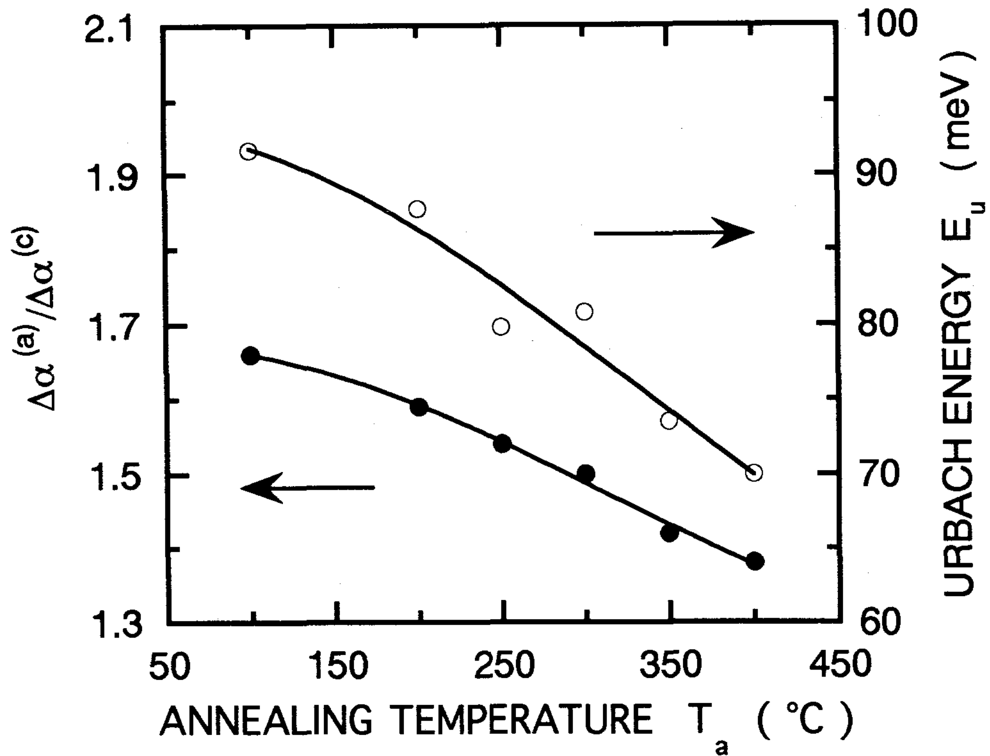

Fig. 5-8. *Ratio $\Delta\alpha^{(a)}/\Delta\alpha^{(c)}$ and Urbach energy E_u plotted against deposition temperature T_a.*

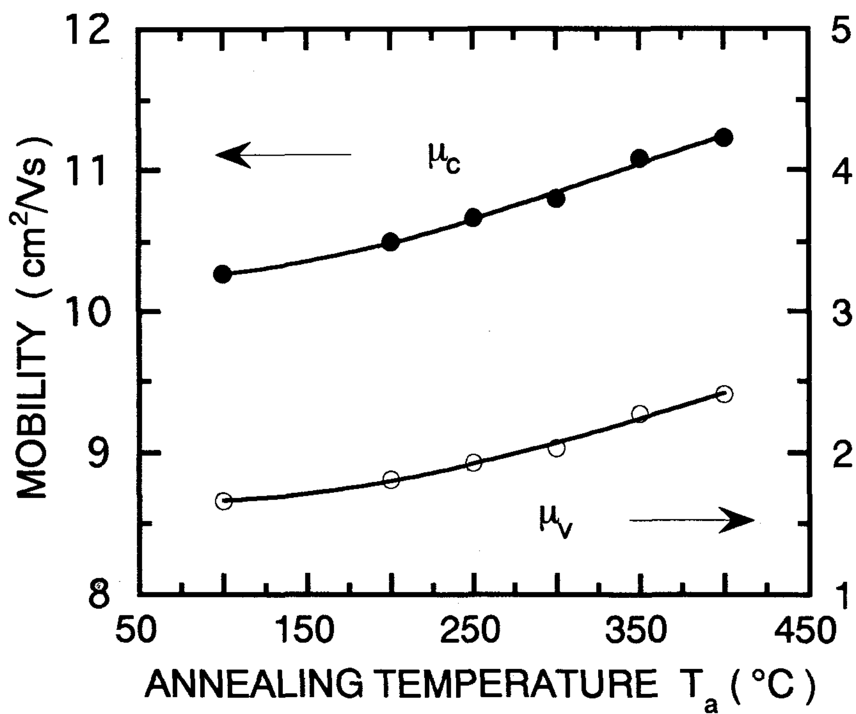

Fig. 5-9. *Electron mobility μ_c and hole mobility μ_v as a function of annealing temperature T_a.*

5-4-3. Alloying effects

Effects of chemical disorder owing to alloying is of great interest from both the fundamental and technological view points. In Fig.5-10, the ratio $\Delta\alpha^{(a)}/\Delta\alpha^{(c)}$ taken on undoped a-$Si_{1-x}Ge_x$:H alloys (x=0 - 52 at.%) and a-$Si_{1-x}C_x$:H (x=0 - 10 at.%) is summarized in comparison with the Urbach energy E_u. A positive, but not unique, correlation stands between these two disorder indicator quantities as explained in the previous section. Free carrier mobilities are estimated from $\Delta\alpha^{(a)}/\Delta\alpha^{(c)}$ data, assuming composition independent dipole matrix element as well as interatomic spacing, and are plotted as a function of Tauc optical band gap in Fig.5-11. It should be mentioned here that the band-gap dependence itself has no physical significance in the sense that the material property can never be determined uniquely by the Tauc optical gap. Immediately read from the figure is that the highest mobility occurs for undoped a-Si:H and it continuously decreases upon alloying, which is likely to be due to the effect of alloy-induced

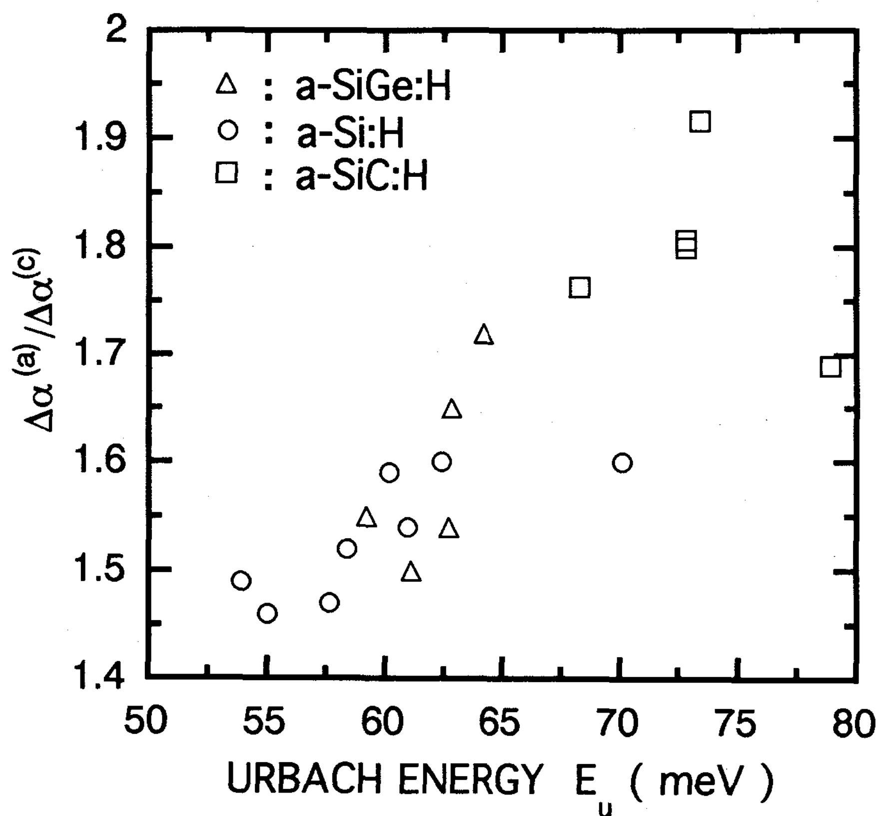

Fig. 5-10. Ratio $\Delta\alpha^{(a)}/\Delta\alpha^{(c)}$ plotted against Urbach energy E_u.

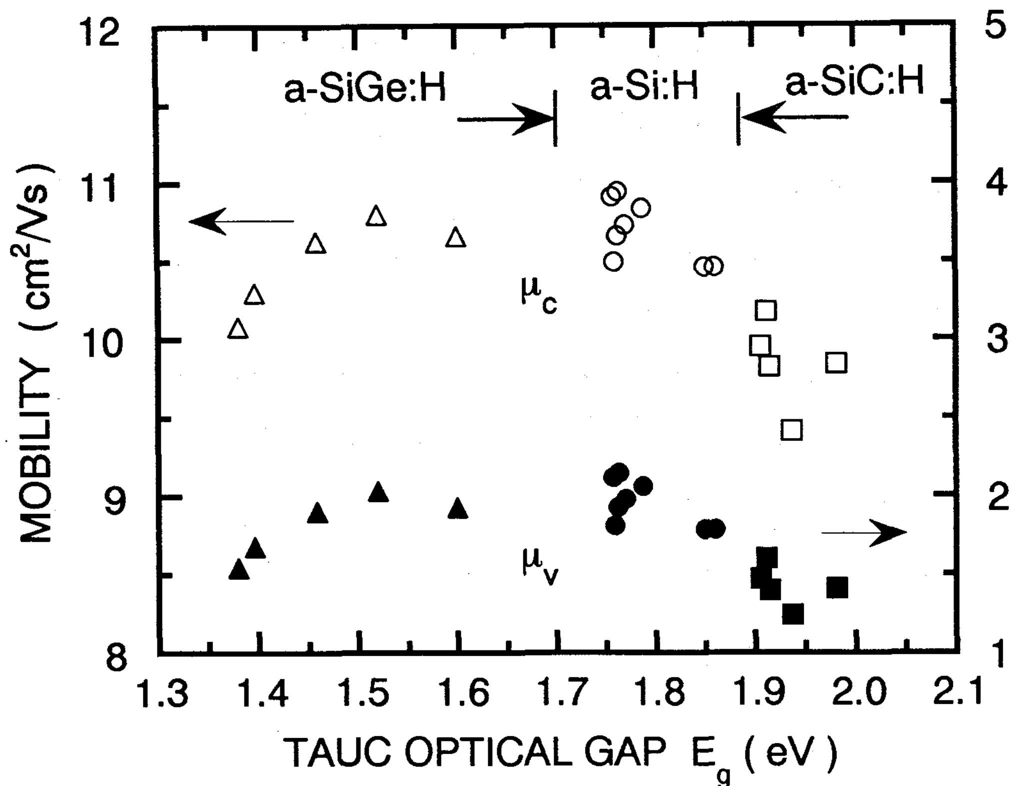

Fig. 5-11. Electron mobility μ_c and hole mobility μ_v as a function of Tauc optical gap E_g.

disorder. Alloying with Ge does not lead to any significant effect on the electron mobility for concentrations up to about 35 at.% (Eg=1.5eV), beyond which it sharply decreases down to about 90% of the a-Si:H value. The same quantitative tendency holds for the hole mobility. The results are in good agreement with that inferred from time-of-flight measurements [15)]. On the other hand, a more pronounced reduction of the mobility is found for carbon alloying. More than a 15% drop results from a carbon concentration of only about 10% (Eg=1.94eV) for both electron and hole mobilities. The behavior of carrier mobilities upon alloying here reported should be regarded as a specific example, and there remains large room for improved mobilities in such alloy materials. Extended experimental efforts based on deeper understandings of growth kinetics are clearly needed to achieve alloy materials possessing carrier mobilities as high as those of present-day standard a-Si:H.

5-5. Summary

The theory of polarized electroabsorption in amorphous semiconductors, which can satisfactorily interpret various characteristic features of observed EA spectra, have been presented. In accordance with theory, a new characterization method has been developed for the determination of carrier mean free path as well as mobility near the band edges in amorphous semiconductors and applied it to a series of undoped a-Si:H alloy materials. The result shows that the electron (hole) mean free path is about 12.5Å (5.5Å) for device quality undoped a-Si:H, which yields estimate of the electron (hole) mobility of 11.2 cm^2/Vs (2.35 cm^2/Vs). The mobilities attain maximum at a particular deposition temperature which would depend on details of deposition conditions. Annealing treatment on a-Si:H deposited at a low temperature improves carrier mobilities through the reduction of structural disorder. Alloying with carbon leads to a continuous reduction of mobility, with the largest drop (15%) for a carbon concentration of about 10%, this being in sharp contrast to a less-pronounced effect by germanium alloying. Finally, the polarized EA technique is expected to offer new possibilities for investigating disorder-induced effects on carrier transport property, as well as for material design for possible device applications.

References

(1) D. E. Aspenes and N. Bottka, in Semiconductor and semimetals, 9, edited by R. K. Willardson and A. C. Beer (Academic, New York, 1972), p. 457.

(2) J. Tauc, Optical Properties of Solids, edited by F. Abeles (Amsterdam: North Holland, 1972), p.279.

(3) G. Weiser, U. Dersch and P. Thomas, Phil. Mag. B, 57 (1988) 721.

(4) H. Okamoto, K. Hattori and Y. Hamakawa , J. Non-Cryst. Solids, 137/138 (1991) 672.

(5) Y. Tsutsumi, H. Okamoto, K. Hattori and Y. Hamakawa, Phil. Mag. B, 69 (1994) 253.

(6) Y. Tsutsumi, H. Yamamoto, K. Hattori, H. Okamoto and Y. Hamakawa, J. Non-Cryst. Solids, 164-166 (1993) 893.

(7) R. Kubo, J. phys. Soc. Japan, 17 (1962) 1100.

(8) T. Lukes and K. T. S. Somartna, J. Phys. C, 3 (1970) 2044.

(9) D. E. Aspnes, Surf. Sci., 37 (1973) 418.

(10) W. B. Jackson, S. M. Kelson, C. C. Tsai, J. W. Allen and S. -J. Oh, Phys. Rev. B, 31 (1985) 5187.

(11) H. Okamoto, K. Hattori and Y. Hamakawa , J. Non-Cryst. Solids, 164-166 (1993) 445 .

(12) K. Tsuji and S. Minomura, J. de Phys. C4, 42 (1981) 233 .

(13) K. Hattori, H. Okamoto and Y. Hamakawa, J. Non-Cryst. Solids, 114 (1989) 678.

(14) T. Tiedje , in Semiconductor and semimetals, 21, C, edited by J. I. Pankove (Academic, New York, 1972), p. 207.

(15) H. Karg, W. Kruhler, M. Moller and K. v. Klitzing, J. Appl. Phys., 60 (1986) 2016.

(16) Y. Tsutsumi, H. Okamoto, K. Hattori and Y. Hamakawa, Mat. Res. Soc. Symposium Proceeding Vol."Amorphous Silicon Technology-1994", (1994) (in press).

Chapter 6. DEVICE MODELING OF AMORPHOUS SILICON SOLAR CELLS

6-1. Introduction

Amorphous silicon (a-Si) p-i-n junction device born in 1975 have now become a viable technology for the production of low-cost and large-area solar cells [1]. Efficiencies of these devices have been increased up to the level of 12% through continuous optimization of material and junction formation processes and geometrical configuration of the devices, and also by an introduction of amorphous silicon carbide as a wide-window heterojunction contact. However, since the achievable maximum efficiency is determined by the number of photons in the solar radiation spectrum which can be absorbed in the active material of the devices, drastically increase in the efficiency will not be expected for the conventional a-SiC/a-Si heterojunction devices whose active layer, a-Si, has the band gap in the range of 1.7eV-1.8eV.

One of the promising ways to break this limitation is to introduce narrow band gap amorphous alloys and to form tandem junction structure so that a larger portion of the solar radiation spectrum can be converted by the devices. Then, we are urged to developed amorphous silicon based alloys with the band gap below 1.7eV, while retaining the film quality as a photovoltaic active layer. A large deal of efforts has been made along with this direction, and some encouraging results have now reported [2][3]. However, at the present stage of the development, the film quality tends to become worse as the band gap of the alloys is reduced, which will result in the inferior collection efficiency, and thereby limit the utility of the narrower band gap alloys. Therefore, there should be optimum selection of the band gaps for the present-day narrow band gap alloys in both single and tandem device configurations.

A simple analytical model for simulating photovoltaic characteristics of amorphous based p-i-n junction devices have developed in current paper [4]. The model can also be used to extract information about physical parameters responsible for the photovoltaic performances in actual device structures [5]. In this chapter, the author has characterized several physical parameters in the p-i-n junctions using amorphous silicon germanium (a-SiGe) alloys of various band gaps, and evaluated realistic efficiencies for geometrically optimized devices. This chapter describes

how high efficiencies are expected in the single and tandem junction devices (two- and four-terminal two-cell tandem structures) based on present-day a-SiGe alloys as well as to give a guideline for the band gap selection in these devices.

6-2. Device modeling of single and tandem solar cell

As is now well recognized, the photovoltaic operation of amorphous based p-i-n junction devices is very much complicated. A formal modeling must be based up simultaneous solutions to carrier continuity equations and Poisson's equation [6)7)8)], which requires detailed knowledge about the gap states profile and relevant carrier capture cross section. Unfortunately, consensus has not yet been gained even about energy location of the dangling bond states in most extensively studied a-Si:H which is considered to play a central role in carrier recombination [9)]. Although the formal modeling relying on arbitrary choice of these basic parameters will have some significance in understanding the general feature of the photovoltaic operation, it may not serve as a practical modeling for amorphous-based devices with less-studied materials.

In the contrast, our simple model can not describe details of the operation, nevertheless, it can be readily applied to the practical devices and provide useful information needed for the optimization procedure [10)]. This model basically relies on the regional approximation first proposed by Crandall [11)]. The photovoltaic active layer is separated into two regions by a characteristic boundary x_c; in each region, either electrons and holes are assumed to behave just like the minority carriers recombining with counter carriers with apparent photovoltaic lifetimes $\tau_{n(PV)}$, $\tau_{p(PV)}$. The boundary x_c is determined through the distribution of excess carriers (photogenerated carriers plus carriers injected from both sides of doped contact layers), and thereby tends to move according to the incident light spectrum and bias voltage [4)]. The effects of carrier recombination and an inhomogeneous electric field in the surface and interface regions are renormalized into the effective surface recombination factors S_n, S_p at the p/i and i/n interfaces, respectively [5)].

In this model, the original electric field is assumed to be reserved even under sunlight illumination. For the sake of simplicity, a uniform electric field approximately is adopted, and

then it is represented in terms of the built-in potential V_b. Eventually, the J-V characteristics of the devices are described with a set of physical parameters; $\mu_n\tau_{n(PV)}$, $\mu_p\tau_{p(PV)}$, S_n, S_p, V_b and conductivities σ_n, σ_p of doped contact layers [4]. Here, since our main concern in this report is to relate efficiency to band gap energy and film quality of the active layer, it is best to show how the J-V characteristics varies with the film quality parameter $\mu\tau_{(PV)}$ (here, sum of the photovoltaic mobility-lifetime products of electrons and holes). For the sake of simplicity, we adopted that $\mu\tau_{(PV)}=\mu_n\tau_{n(PV)}=\mu_p\tau_{p(PV)}$, $S_n=S_p=10^3$V/cm, $\sigma_p=10^{-7}$S/cm and $\sigma_n=10^{-5}$S/cm and calculated the J-V characteristics of a-Si alloy solar cell under simulated AM1.5 sunlight of 100mW/cm^2. Then, the thickness of the active layer with which the conversion efficiency becomes maximum for a set of physical parameters is selected. Figure 6-1 and 6-2 demonstrate examples of J-V

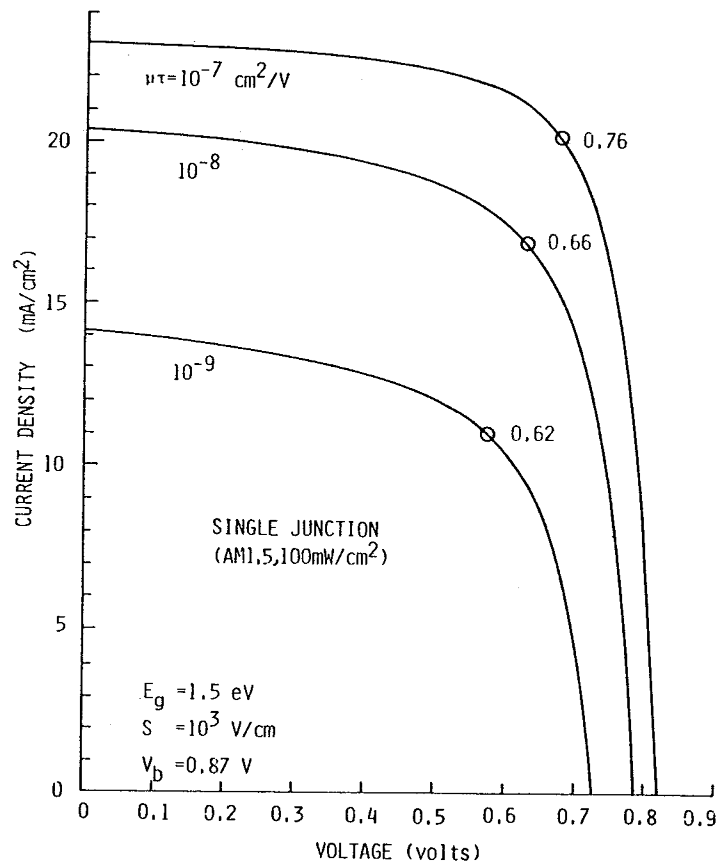

Fig.6-1. Illuminated J-V characteristics as a function of photovoltaic mobility-lifetime products under AM1.5 sunlight. The absorption coefficient spectrum of a-Si:H film with the band gap of 1.75eV were used for the calculation.

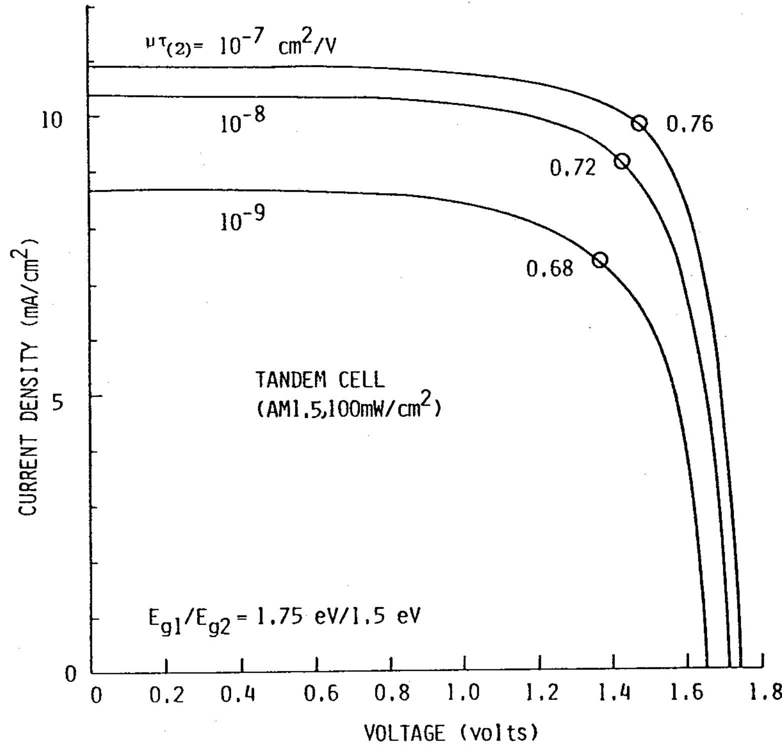

Fig.6-2 Illuminated J-V characteristics as a function of photovoltaic mobility-lifetime product under AM1.5 sunlight. The absorption coefficient spectrum of a-SiGe film with the band gap of 1.5eV were used for the calculation.

characteristics of geometrically optimized single junction devices (E_g=1.5eV) and two-terminal two-cell tandem junction devices (E_{g1}/E_{g2}=1.75eV/1.5eV) with various film qualities, respectively. In Fig.6-2, we adopted the present-day best a-Si, of which $\mu\tau_{(PV)}$ was assumed to be $10^{-7}cm^2/V$ [13], as a top cell materials (E_g=1.75eV). Clearly, these figures indicate that all the solar cell parameters are strongly controlled by the film quality parameter. The interface quality parameter S also makes an important contribution in determining the performance, which was fixed at 10^3V/cm (minimum value actually observed) for all the calculations in this work. Moreover, as shown in Fig.6-2, it is noted that the film quality of the bottom cell material (here,E_g=1.5eV) for the two-terminal two-cell tandem device has less influence than that for the single junction device. Therefore, it is suggested that as the tandem structure device is used, the worse film quality of the narrow band gap materials may be covered somewhat and the effective utilization of the light with long wavelength may be made.

6-3. Efficiency estimates for single and tandem devices

6-3-1. Built-in potential

In amorphous-based p-i-n junction devices, carrier drift due to the built-in field makes a predominant role in the photogenerated carrier collection process. In this sense, it is of prime importance to know its magnitude in the active layer to make realistic estimates of the efficiencies. The built-in field or built-in potential can be measured by means of field-modulated absorption in the back surface reflection geometry (Back-Surface-Reflected-Electroabsorption; BASREA) on actual device structures [12]. The internal electric field is modulated by either the square or sinusoidal-wave of a peak-to-peak voltage ΔV_{pp}, superimposed to the dc bias voltage V_{dc}. The monochromatic light is directed on the cell, and the field-induced change in the magnitude of the reflected light intensity is monitored by the standard lock-in technique. The field-induced change, BASREA signal ΔS, is observed at the low absorption region in the vicinity of the optical absorption edge. The BASREA signal ΔS then provides an information about how the internal electric field in the i-layer is modulated by the modulation field, as well as that about the unperturbed built-in field. Theoretical analysis on the BASREA signal leads to a conclusion that if the unperturbed electric field is uniform within the entire i-layer region, ΔS should have a simple form [12],

$$\Delta S(\lambda;V_{dc},\Delta V_{pp}) = D(\lambda) \cdot \Delta V_{pp}[V_{dc} - V_b] \ , \qquad (6\text{-}1)$$

where the electroabsorption (EA) line-shape function $D(\lambda)$ depends only on the light wavelength. The important consequences of this relation are i) ΔS linearly depends on the dc bias voltage V_{dc}, and if normalized by ΔV_{pp}, then all the date points fall on a single straight line in the S vs. V_{dc} plot, ii) the built-in potential V_b is determined from the point at which this line intercepts the V_{dc} axis and iii) V_{dc} is uniquely determined regardless of the light wavelength used for the measurement.An example of the experimental data taken on the cell of a structure SnO_2/p a-Si/i a-SiGe(E_g=1.4eV)/n μc-Si/Al is shown in Figure 6-3. The BASREA signal appears in the spectral region near around the optical band gap energy of the active material, as shown in

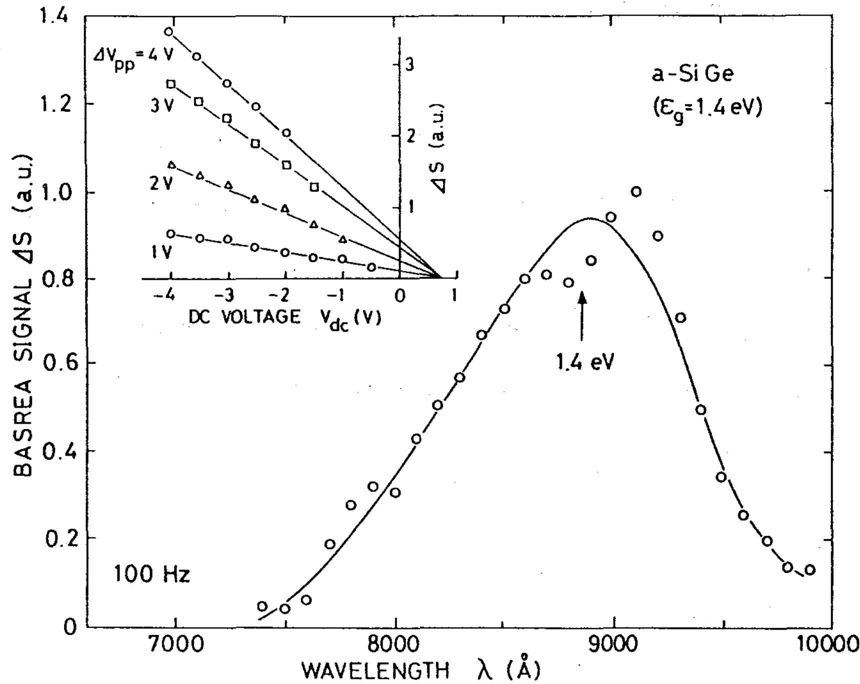

Fig.6-3. Typical BASREA spectrum of an actual p a-Si/i a-SiGe/n μc-Si single junction devices whose active layer, a-SiGe, has the energy band gap of 1.4eV. Inset shows BASREA signal intensity plotted as a function of the bias voltage V_{dc} for various modulation voltages ΔV_{pp}.

Fig.6-3. The inset shows the BASREA signal intensity plotted against the dc bias voltage V_{dc} for various modulation voltage ΔV_{pp}. The observed behavior of the signal ΔS is coincident with the above prediction. It can been seen that the BASREA signal has a linear dependence of the V_{dc} and all the extrapolated straight lines intercept the dc voltage axis at the same point. This implies that the internal electric field in the active layer is uniform, and the V_b is determining at the crossing point on V_{dc} axis. Figure 6-4 summarizes V_b thus measured upon p a-Si/i a-SiGe/ n μc-Si devices having active layers of a-SiGe with various energy band gaps. As is found, the V_b gradually decreases from about 0.9V to 0.68V as reducing the band gap from 1.8eV to 1.3eV. The previous experiment has revealed that the V_b increases by about 80mV with providing p-type a-SiC of 2eV band gap instead of p-type a-Si [12]. Hence, we suppose this to be true for devices of the a-SiC/a-SiGe/μc-Si heterojunction structure.

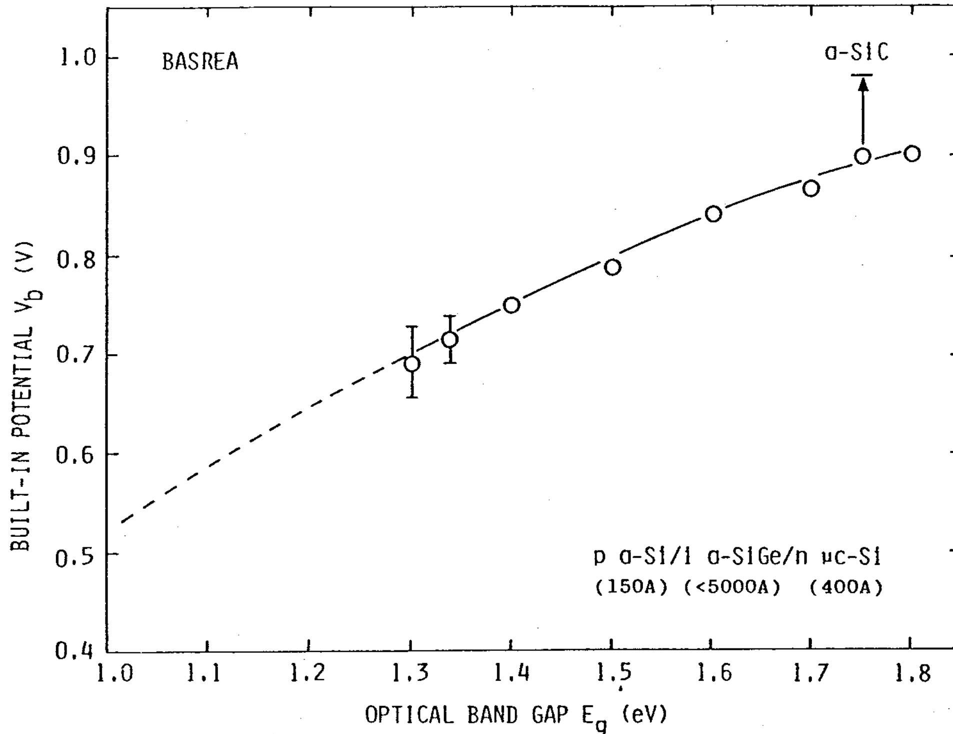

Fig.6-4. Built-in potential V_b of p a-Si/i a-SiGe/n μc-Si single junction devices measured by means of the BASREA technique.

6-3-2 Relation between film quality and conversion efficiency

By means of the device modeling described in section 6-2, the author have calculated efficiencies expected for the single p a-SiC/i a-SiGe/n μc-Si heterojunction devices having active a-SiGe layers with various band gaps and film quality parameters. Each device has been geometrically optimized so as to attain the highest efficiency. In the calculation, the built-in potential V_b projected from the results of Fig.6-4 was used, and the interface quality parameters were assumed to be 10^3V/cm. The upper-limit of the film quality was fixed at that for the present-day best a-Si. Results are plotted in Fig.6-5. If the reduction of the band gap does not involves any degradation of film quality, as is seen is this plot, an efficiency of about 14% will be achieved with a-SiGe alloys of the 1.4eV band gap. Similar calculations have been made for the two- and four-terminal two-cell tandem devices, where we adopted 1.75eV a-Si:H as a top cell material. All the geometrical parameters have again been optimized for the various sets of the band gap and film quality parameters of the bottom cell. Results are plotted in Fig.6-6 and

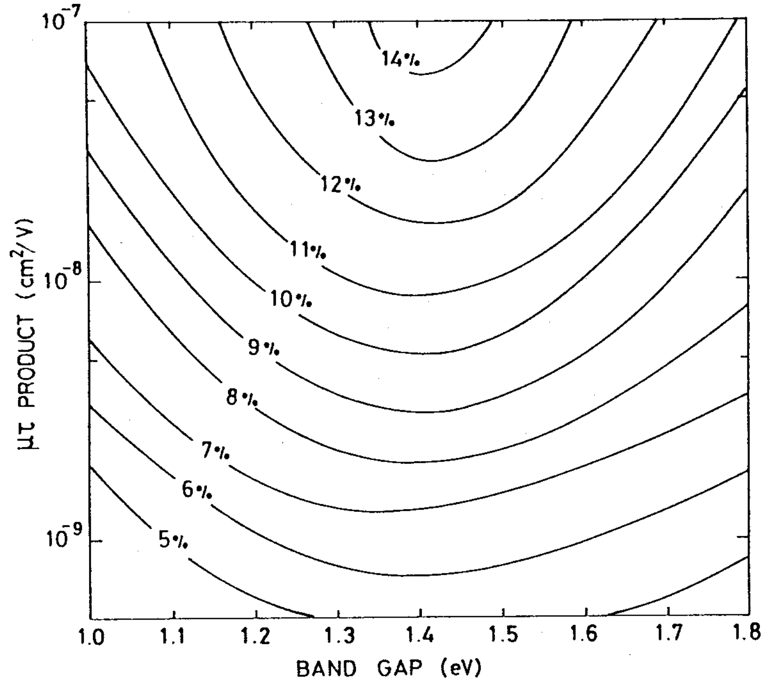

Fig.6-5. Iso-efficiency plots for p a-SiC/i a-SiGe/n μc-Si single junction device. Thickness of the active a-SiGe layer was optimized so as to give the highest efficiency.

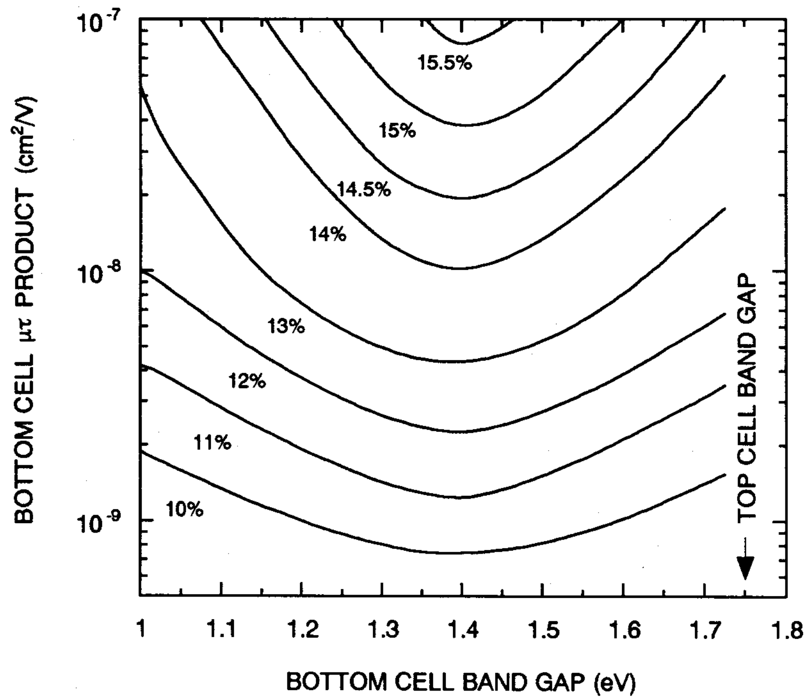

Fig.6-6. Iso-efficiency plots for p a-SiC/i a-SiGe/n μc-Si two-terminal tandem junction device. Thickness of the active a-SiGe layer was optimized so as to give the highest efficiency.

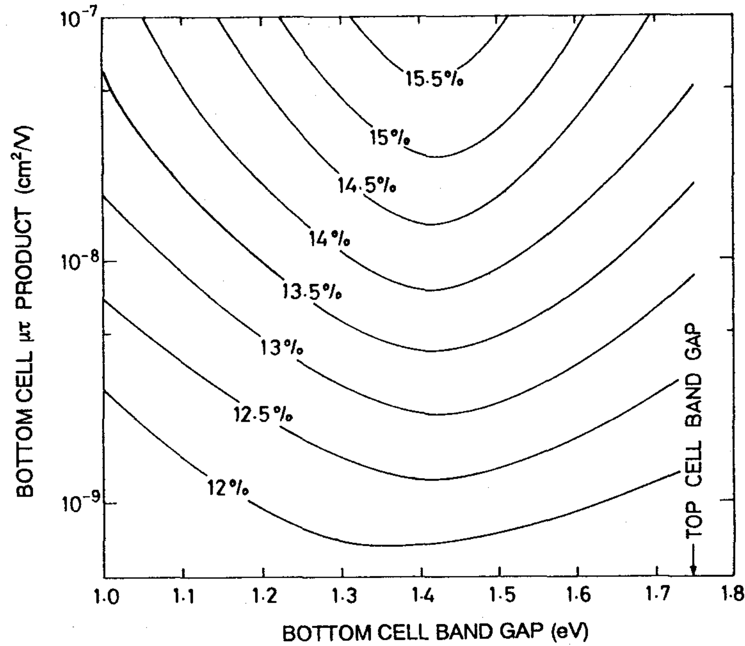

Fig.6-7. Iso-efficiency plots for p a-SiC/i a-SiGe/n μc-Si four-terminal tandem junction device. Thickness of the active a-SiGe layer was optimized so as to give the highest efficiency.

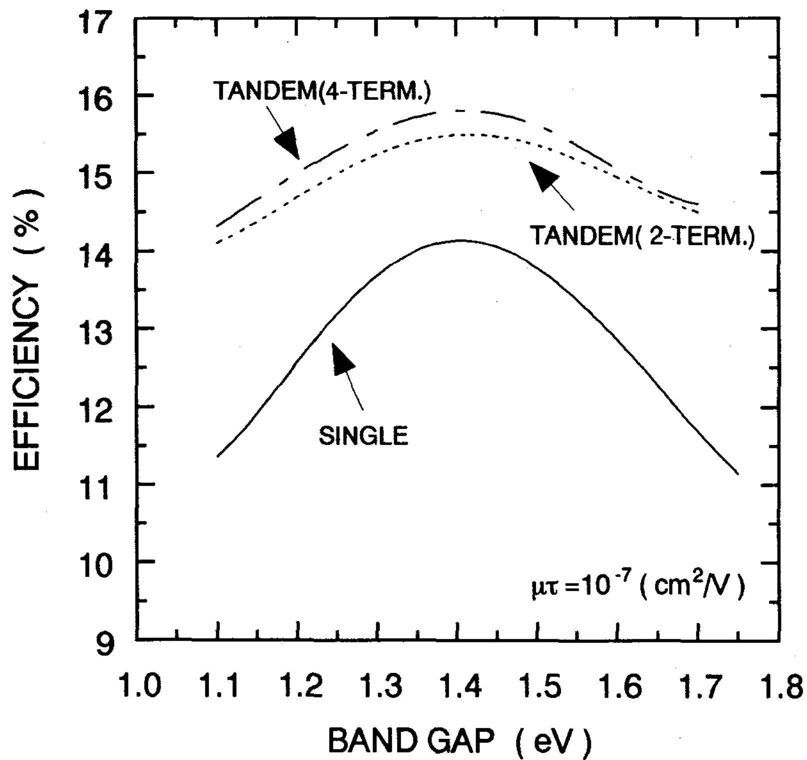

Fig.6-8. Efficiencies expected for the single and tandem junction devices provided the film quality of this alloy is comparable of that of present-day best a-Si.

6-7, indicating that efficiency in around 16% is expected for the two- and four-terminal two-cell tandem devices having 1.4eV band gap bottom cell if the film quality of this alloy is comparable to that of present-day best a-Si. Figure 6-8 shows efficiencies of these devices provided the film quality of this alloy is comparable of that of present-day best a-Si. Efficiencies estimated here are almost identical with those reported by Hack although the basis for the calculation is different each other [13].

6-4. Realistic efficiencies of single and tandem devices with present-day a-SiGe alloys

6-4-1 Determination of film quality parameters

In other to make realistic estimates of efficiencies achievable in single and tandem devices based upon present-day best a-SiGe alloys, we must know the film quality parameters($\mu\tau$–products) of these alloys. If the built-in potential V_b is known, the mobility-lifetime products can be characterized by an analysis on the variation of the carrier collection efficiency spectrum with the applied bias voltage V_a [5]. In practice, it is better to treat the normalized carrier collection efficiency $\eta(\lambda,V_a)/\eta(\lambda,0)$, because such normalization procedure compensates for the spectral dependencies of the optical system including monochrometor and light source. Figure 6-9 shows an example of normalized carrier collection efficiency spectra measured upon 1.6eV a-SiGe single junction device. Detailed examination of $\eta(\lambda,V_a)/\eta(\lambda,0)$ spectra has shown that they are mainly dominated by the magnitudes of $\mu_n\tau_n+\mu_p\tau_p$ and $S_n x S_p$ at the lower absorption region $\mu_n\tau_n/\mu_p\tau_p$ and the front side effective surface recombination parameter at the higher absorption region. Making use of this trend, if experimental data of $\eta(\lambda,V_a)/\eta(\lambda,0)$ for at least two different applied voltages V_a's in both lower and higher absorption regions are given, $\mu_n\tau_n$, $\mu_p\tau_p$, $S_n$and S_p can be separately evaluated. In Fig.6-9, solid lines are theoretical plots fitted to the measured spectra with determined physical parameters. Details of the fitting procedure are described in the present paper [5]. Then, Figure 6-10 summarizes film quality parameter, that is the photovoltaic mobility-lifetime product $(\mu\tau)_{PV}$, as a function of the band gap of a-SiGe alloys. The closed circles refer to the mobility-lifetime product $(\mu\tau)_{PC}$ measured by photoconductivity. As is seen in this figure, the film quality parameter gets gradually worse as the band

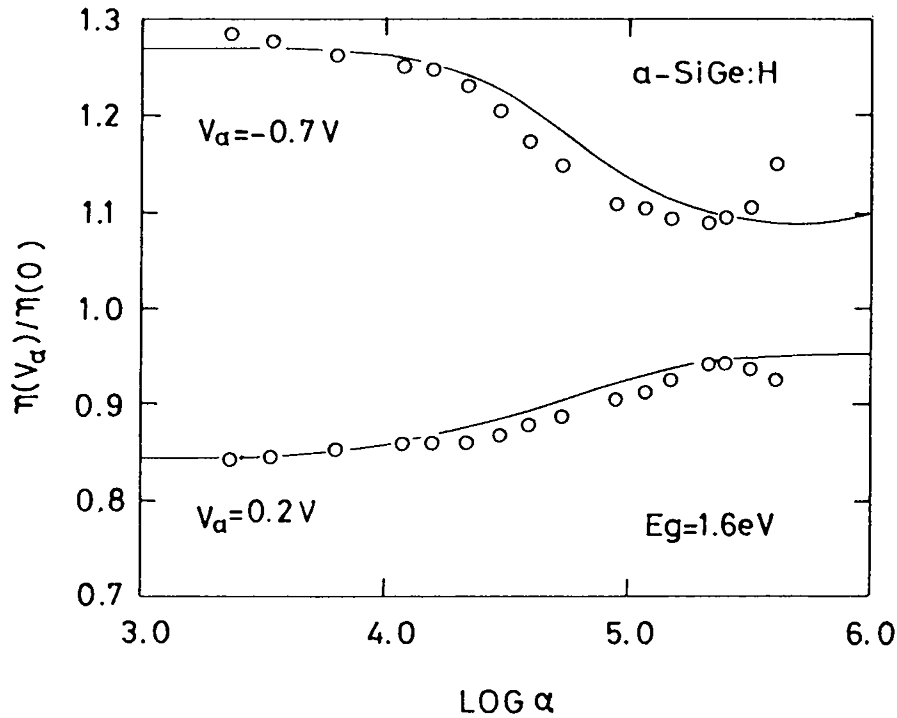

Fig.6-9. An example of normalized carrier collection efficiency spectra as a function of the absorption coefficient a of the a-SiGe active layer. The solid lines are theoretical plots calculated with determined physical parameters.

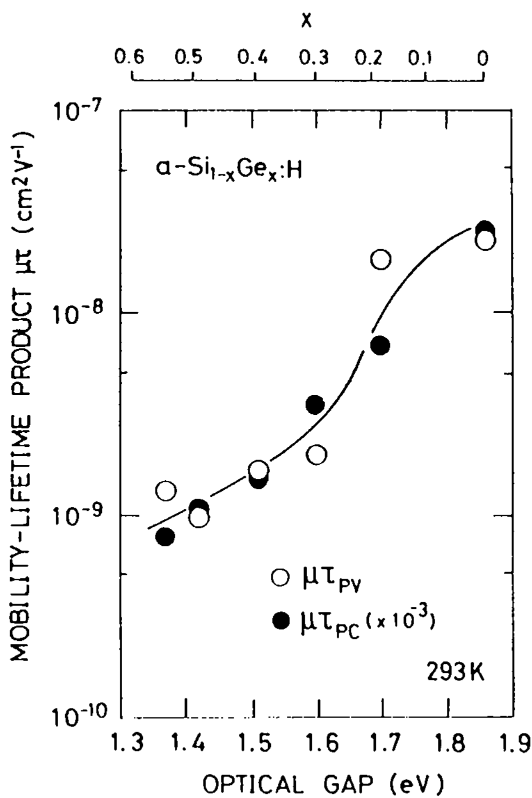

Fig.6-10. Photovoltaic mobility-lifetime product $\mu\tau_{(PV)}$ as a function of the band gap determined with an analysis of the normalized carrier collection efficiency spectrum. $\mu\tau_{(PC)}$ denotes mobility-lifetime product measured by photo-conductivity.

gap is reduced. A noticeable point found in this figure is that the photovoltaic film quality parameter varies along with the photoconductivity parameter. We assume this to hold for wide range of a-SiGe alloys so far as the equilibrium Fermi level located near around the center of the gap. Assumption is made thereby that this criterion does hold for further improved a-SiGe alloys. Based upon this criterion, we have estimated the photovoltaic film quality from the projection of the photoconductivity data released from the ETL group for further improved (triode+hydrogen dilution) a-SiGe alloys shown in Figure 6-11 [3], where it is assumed that $(\mu\tau)_{PV}$=(photoconductivity)x10^{-3}.

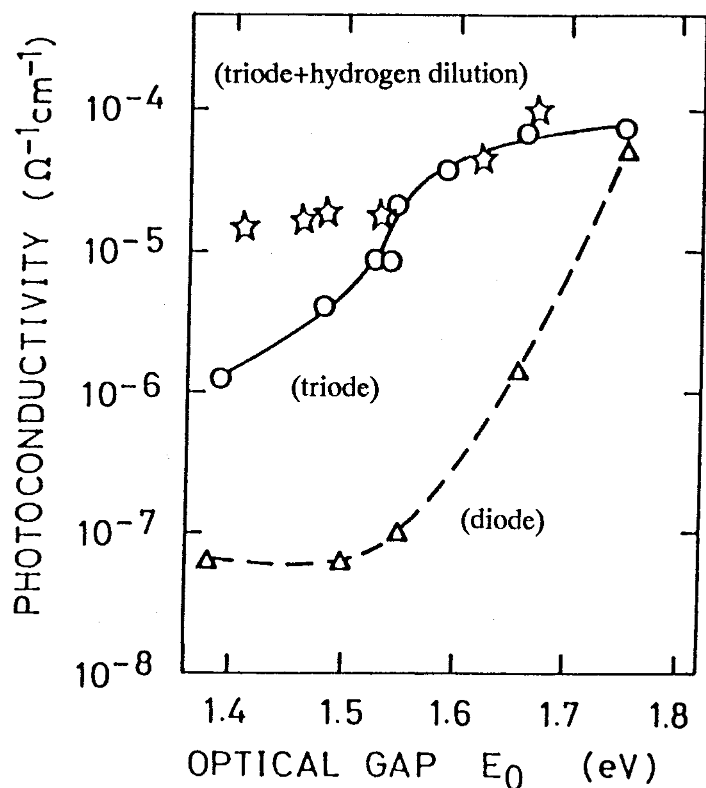

Fig.11 Photoconductivity data released from the ETL group for further improved a-SiGe alloys [3].

6-4-2 Realistic efficiencies

Film quality parameters estimated for present-day a-SiGe alloys with various band gaps were applied to Fig.6-5 ,6-6 and 6-7 to yield realistic estimates of efficiencies achievable in the single and tandem junction devices. Figure 6-12 shows realistic efficiencies of these devices plotted against band gap, where the upper- and lower-limit of the efficiencies in the tandem cells present the value of four- and two-terminal cells respectively. This figure suggests that optimum band gap for the single junction device is around 1.55eV, and the highest efficiency is about 12.3%. An a-SiGe alloy with the band gap of 1.5eV is conventionally applied for the

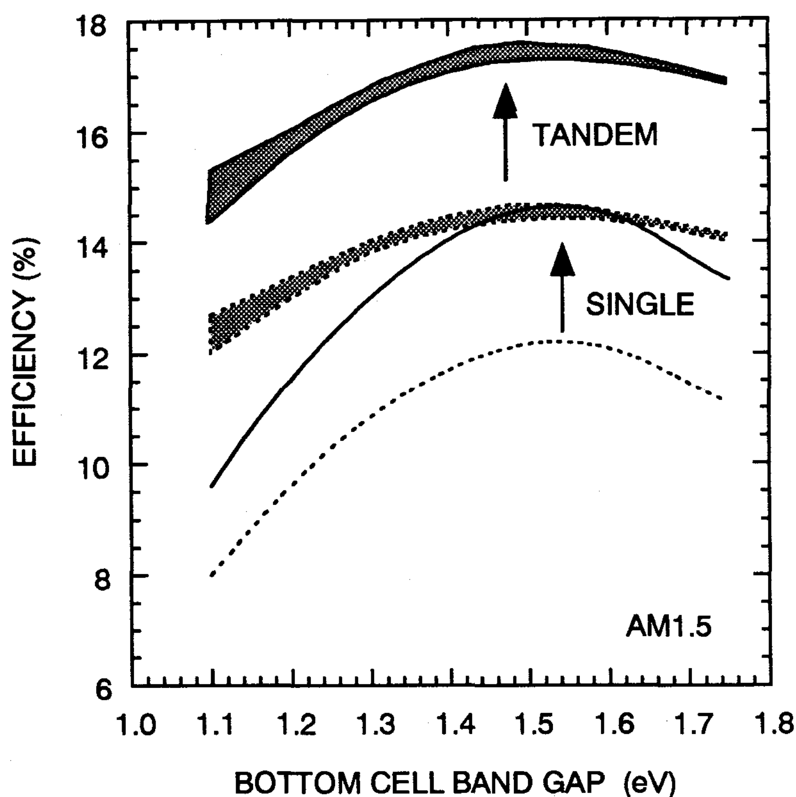

Fig.6-12. Realistic efficiencies achievable in single and tandem junction devices using presently available a-SiGe alloys, prepared by a triode-type reactor with hydrogen dilution, where the upper- and lower-limit of the efficiencies in the tandem cells present the value of four- and two-terminal cells respectively. The arrows indicate the value of an enhancement of the efficiencies by a factor of about 20%, which will be possible through utilization of optical confinement and introduction of photovoltaically active wide-window heterojunction materials.

single junction devices, however, as is seen in this figure, achievable efficiencies are at most 12% for present-day a-SiGe alloys. Similarly, with 1.5eV a-SiGe alloys, efficiencies of the tandem junction devices will be in the range of 14.2-14.7%. The world-record efficiencies reported by ECD group correspond to those expected for the two-terminal two-cell tandem device. In the two-terminal two-cell tandem junction devices, the highest efficiency is about 14.2% with the band gap around 1.55eV, while efficiency around 14.8% is expected in the four-terminal two-cell tandem device with a-SiGe alloy of the band gap around 1.48eV. These calculated efficiencies are a little bit smaller as compared with those derived by Hack through the calculations including realistic physical parameters [15].

Finally, it should be noted that efficiencies over 12% have been achieved an a-Si based single junction solar cells, with the highest number 13.2%. These accomplishments are attributed basically to an incorporation of highly conductive wide-band gap p-layer [16] including μc-SiC, δ-doped a-Si and a-Si/a-C multilayers as well as to an effective utilization of long-wavelength lost by means of textured TCO substrates, both of which are not taken into account in the present simulation. In this sense, the prospect efficiencies here presented would be underestimated by a factor around 20% for a-Si:H of the band gap 1.75eV. If the same is assumed to be true for a-SiGe based solar cells, then efficiencies around 14%, 17–17.6% are expected for single and tandem solar cells respectively, using the present-day best a-SiGe alloys, which are also shown in Fig.6-12.

6-5. Summary

An attempt has been made to model the performance of both single and tandem junction devices using present-day best a-SiGe alloys. Efficiencies up to 12.3%, 14.2% and 14.7% are projected for these devices with present-day best a-SiGe alloys having band gap of 1.55eV, 1.55eV and 1.48eV, respectively. Additional efficiency improvement will be possible through utilization of optical confinement effect and introduction of photovoltaically active wide-window heterojunction materials, which would yield an enhancement of the efficiencies by a factor of about 20%.

References

(1) D.E. Carlson and C.R. Wronski, Appl. Phys. Lett., 28 (1976) 671.

(2) T. Yang, R. Rose, R. Mohr and J.P. Fournier, Proc. 18th IEEE Photovoltaic Specialists Conf., Las Vegas (1985) 1519.

(3) A. Matsuda, M. Koyama, N. Ikuchi, Y. Imanishi and K. Tanaka, Jpn. J. Appl. Phys., 25 (1986) L54.

(4) H. Okamoto, H. Kida, S. Nonomura and Y. Hamakawa, Solar Cells, 8 (1983) 317.

(5) H. Okamoto, H. Kida, S. Nonomura, K. Fukumoto and Y. Hamakawa, J. Appl. Phys., 54 (1983) 3236.

(6) M. Hack and M. Shur, J. Appl. Phys., 58 (1985) 997.

(7) I. Sakata and Y. Hayasi, Appl. Phys. Lett., 42 (1983) 279.

(8) P.J. Schwartz, J.L. Gray, G.B. Turner, D. Kanani and H. Ullal, Proc. 17th IEEE Photovoltaic Specialists Conf., Orlando (1984) 369.

(9) R.A Street, J. Zesch and M.T. Thompson, Appl. Phys. Lett., 43 (1983) 672.

(10) H. Okamoto, H. Kida, K. Fukumoto, S. Nonomura and Y. Hamakawa, J. Non-Cryst. Solids, 59/60 (1983) 1103.

(11) R.S. Crandall, J. Appl. Phys., 54 (1983) 3136.

(12) S. Nonomura, H. Okamoto and Y. Hamakawa, Appl. Phys. A, 32 (1983) 31.

(13) M. Hack and S. Guha, Appl. Phys. Lett., 45 (1984) 244.

Chapter 7. CONCLUSIONS

A systematic study has been carried out on the localized states in the mobility gap as well as the carrier transport property of amorphous silicon alloys. The main results obtained in this thesis work are enumerated as follows:

(1) The modulation photocurrent spectroscopy (MPCS) has been utilized to investigate deep localized states in undoped a-Si:H alloys. Two types of defect center are observed in undoped a-Si:H, one of which is assigned as due to a dangling bond. Measurements performed under different temperatures and excitation photon energies read to a completely identical density-of-states distribution of the D^-center; a near-Gaussian distribution centered at about 0.5eV below the conduction band edge. Upon light soaking, the densities of not only the dangling bonds but also as-yet unidentified defect center (H1) designate systematic changes, suggesting that these two centers are involved in the photo-induced degradation effects although the dangling bonds may play a central role in carrier recombination.

(2) Attempt-to-escape frequency shows a temperature dependence of the form exp(0.39eV/kT) in the temperature range from 240 to 320K, while it tends to saturate at around $10^{12}s^{-1}$ for temperature below 230K. This behavior is accounted for by assuming two-step emission from the D^- center via an intermediate unrelaxed state. The MPCS reveals the existence of another electron state located shallower by about 0.2eV than the D^- center. It has tentatively been assigned to the unrelaxed state (E1) of the D^- center. The plausibility of this assignment has been discussed, although the microscopic nature of the unrelaxed state is not yet identified.

(3) Density-of-states distribution in a-Si alloy materials derived by MPCS reveals a distinct feature associated with doubly occupied dangling bonds (D^-), of which the total density increases by about two orders of magnitude as the bandgap of the alloys decreases from 1.8eV (a-Si:H) to 1.16eV (a-$Si_{0.2}Ge_{0.8}$:H). The peak of the D^- center shows a non-monotonic depen-

dence on the band gap energy, shifting from about 0.56eV in a-Si:H to about 0.33eV as the band gap decreases, and then an abrupt downward shift of about 0.1eV occurs when the bandgap crosses 1.5eV (Ge concentration, about 35 at.%), again shifting to 0.32eV in a 1.16eV bandgap alloy. The attempt-to-escape frequency behaves in different ways for the alloys with band gaps larger than 1.5eV and less than 1.5eV, suggesting that different electron transition mechanisms may be operative in each alloy composition or bandgap region. The experimental results allow us to conclude that the D^- center observed in the MPCS originates from the Si dangling bonds in the alloys with a bandgap larger than 1.5eV and from the Ge dangling bonds in the alloys with a bandgap less than 1.5eV. For a-SiC:H with the band gap less than the 2.01eV, only Si-related D^- center has been observed, of which the density designates a sharp increase upon carbon alloying.

(4) Time-resolved photocurrent spectroscopy (TPCS) analysis is proven successful to extract localized states distribution from photocurrent transients, irregardless of "pre" and "post" transit time regimes. The TPCS spectra measured on a-Si:H exhibit the electron trap states at about 0.35eV (E1) below the conduction band edge and the hole trap states at 0.35-0.45eV (H2) above the valence band edge . The origin of these newly-observed trap states has not yet been identified, however, they appear to be closely linked with carrier transport property as well as the light-induced effects.

(5) Light-induced change of MPCS and TPCS spectra indicates that the present of non-equilibrium carriers itself is essentially responsible for the creation of metastable defect centers, although carrier recombination may further enhance the creation probability. The bond breaking model associated with Si-Si weak bonds is likely to be applied to interpret the carrier-induced defect creation phenomenon. On the other hand, the different behaviors of the increase in the defect densities suggests that another process may also be operative in addition to the defect creation process; that is, defect conversion from the H1 to D center, which is triggered by carrier capture, specifically by hole capture. This implies that the H1 center works as an optional

source for the metastable dangling bond centers.

(6) Optical absorption spectra of various a-Si:H alloys measured by the photothermal deflection spectroscopy demonstrates that the valence band-tail states varies systematically with material composition and details of preparation conditions and/or thermal history.

(7) Polarized electroabsorption (EA) technique has been investigated on various a-Si:H alloys. The electron (hole) mean free path is estimated about 12.5Å (5.5Å) for device quality undoped a-Si:H, which yields estimate of the electron (hole) mobility of 11.2 cm2/Vs (2.35 cm^2/Vs), by the analysis of the polarized EA signal. The mobilities attain maximum at a particular deposition temperature which would depend on details of deposition conditions. Annealing treatment on a-Si:H deposited at a low temperature improves carrier mobilities through the reduction of structural disorder. Alloying with carbon leads to a continuous reduction of mobility, with the largest drop (15%) for a carbon concentration of about 10%, this being in sharp contrast to a less-pronounced effect by germanium alloying. Polarized electroabsorption (EA) technique is expected to offer new possibilities for investigating disorder-induced effects on carrier transport property, as well as for material design for possible device applications.

(8) An attempt has been made to model the performance of both single and tandem junction devices using present-day best a-SiGe alloys. Efficiencies up to 12.3%, 14.2% and 14.7% are projected for these devices with present-day best a-SiGe alloys having band gap of 1.55eV, 1.55eV and 1.48eV, respectively. Additional efficiency improvement will be possible through utilization of optical confinement effect and introduction of photovoltaically active wide-window heterojunction materials, which would yield an enhancement of the efficiencies by a factor of about 20%.

VITA

Yasuo Tsutsumi was born in Himeji, Hyogo, Japan in Feburary 17, 1954. He graduated from Himejinishi Senior High School, Himeji in March 1972 and entered Gifu University, Gifu in April 1972. He graduated from Gifu University in March 1976 and entered the Graduate School in April of that year. While at Gifu University, he became a member of the Japan Society of Applied Physics. He recieved his Master of Engineering degree in Electronic Engineering in March 1978 from Gifu University. In Octorber 1985, he joined Akashi College of Technology, Akashi.

LIST OF PUBLICATIONS

(I) FULL PAPER

(1) S. Nitta, K. Shimakawa, T. Endo, Y. Tsutsumi and M. Morigaki:
"Optical properties of glow discharge amorphous silicon films", in Oyo Buturi, No.47 (1978) 1080-1083 .

(2) K. Abe, H. Okamoto, Y. Nitta, Y. Tsutsumi, K. Hattori and Y. Hamakawa:
"Gap states in undoped amorphous silicon studied by below-gap modulated photocurrent spectroscopy", in Phil. Mag. B, 58 (1988) 171-184.

(3) Y. Tsutsumi, H. Okamoto and Y. Hamakawa:
"Measurement of gap states in undoped a-SiGe:H alloys by modulated photocurrent spectroscopy", in Phil. Mag. B, 60 (1989) 695-712.

(4) Y. Tsutsumi, H. Okamoto, K. Hattori and Y. Hamakawa:
"Polarized electroabsorption effect in hydrogenated amorphous silicon alloys and its implication for band edge mobility", in Phil. Mag. B, 69 (1994) 253-261.

(II) INTERNATIONAL CONFERENCE

(1) K. Shimakawa, S. Nitta, M. Mori, T. Endo and Y. Tsutsumi:
"Localized states in Te_xSe_{1-x} glass semiconductors estimated by dielectric relaxation", in Proceeding of 11th International Congress on Glass, Prague, Vol.1 (1977) 381-386.

(2) S. Nitta, K. Shimakawa, Y. Tsutsumi, T. Endo and K. Morigaki:
"Optical properties of glow discharge amorphous silicon films", in 14th Conference on physics of semiconductors, Edinburgh, 1978; Inst. Conf. Ser. No.43, Chapter 30 (1979) 1151-1154.

(3) Y. Tsutsumi, S. Sakata, K. Abe, Y. Nitta, H. Okamoto and Y. Hamakawa:
"Study of gap states in a-SiGe:H alloy systems by below-gap modulated photocurrent spectroscopy", in 12th Int. Conf. on Amorphous and Liquid Semiconductors, Prague, 1987; J. Non-Cryst. Solids 97/98 (1987) 1063-1066.

(4) Y. Tsutsumi, K. Abe, Y. Nitta, H. Okamoto and Y. Hamakawa:
"Below-gap photocurrent spectroscopy for determination of gap states distribution in a-Si alloy systems", in Technical Digest of the International PVSEC-3, Tokyo (1987) 657-660.

(5) H. Okamoto, Y. Tsutsumi, K. Abe and Y. Hamakawa:
"Modulated photocurrent spectroscopy of amorphous silicon alloys", in Proceeding of. 4th International PVSEC, Sydney (1989) 71-80.

(6) Y. Tsutsumi, K. Uchiyama, H. Okamoto and Y. Hamakawa:
"Light-induced change in deep-states of undoped a-Si:H", in 13th Int. Conf. on Amorphous and Liquid Semiconductors, Prague, 1989; J. Non-Cryst. Solids 114 (1989) 627-629.

(7) Y. Tsutsumi, K. Uchiyama, K. Hattori, H. Okamoto and Y. Hamakawa:
"Gap-states distribution in undoped a-Si:H", in Technical Digest of the International PVSEC-5, Kyoto (1990) 809-812.

(8) Y. Tsutsumi, H. Yamamoto, K. Hattori, H. Okamoto and Y. Hamakawa:
"Study of band-edge parameters in a-Si:H alloys by polarized electroabsorption effects", in 15th Int. Conf. on Amorphous Semiconductors, Cambridge, 1993; J. Non-Cryst. Solids, 164-166 (1993) 893-896.

(9) Y. Tsutsumi, H. Okamoto, K. Hattori and Y. Hamakawa (invited):
"Polarized electroabsorption and carrier mobilities in amorphous silicon alloys", in Material Research Society Symposium Proceeding Vol."Amorphous Silicon Technology - 1994" (1994) (in press).

(III) DOMESTIC CONFERENCE

(1) Y. Tsutsumi, S. Nitta, K. Shimakawa and K. Morigaki:
"Photoluminescence in glow discharge a-Si", in the Japan Society of Applied Physics, Extended Abstracts (The 38th Autumn Meeting, 1977), p470.

(2) K. Morigaki, Y. Tsutsumi, S. Nitta, and K. Shimakawa :

"Photoluminescence in glow discharge a-Si", in the Physical Society of Japan, Extended Abstracts (The 32th Autumn Meeting, 1977), p118.

(3) T. Endo, Y. Tsutsumi, M. Mori, S. Nitta and K. Shimakawa:
"Optical and electrical properties of glow discharge a-Si", in the Japan Electrical Related Societies, Extended Abstracts (The Tokai branch Meeting, 1977), p93.

(4) Y. Tsutsumi, K. Oishi, T. Chikuma, S. Nitta, K. Shimakawa and K. Morigaki:
"Photoluminescence in glow discharge a-Si", in the Japan Society of Applied Physics and Related Societies, Extended Abstracts (The 25th Spring Meeting, 1978), p512.

(5) Y. Tsutsumi, K. Abe, H. Kida, H. Okamoto, S. Sakata, M. Ishii, T. Tomikawa, H. Itozaki, N. Fujita and Y. Hamakawa:
"Study of a-SiGe:H by below-gap photocurrent spectrum", in the Japan Society of Applied Physics, Extended Abstracts (The 47th Autumn Meeting, 1986), p853.

(6) K. Abe, Y. Nitta, K. Hattori, Y. Tsutsumi, H. Okamoro and Y. Hamakawa:
"Study of gap states by below-gap modulated photocurrent spectroscopy (I) - undoped a-Si:H -, in the Japan Society of Applied Physics and Related Societies, Extended Abstracts (The 34th Spring Meeting, 1987), p217.

(7) Y. Tsutsumi, K. Abe, H. Okamoto, S. Sakata, M. Ishii, T. Tomikawa, H. Itozaki, N. Fujita and Y. Hamakawa:
"Study of gap states by below-gap modulated photocurrent spectroscopy (II) - undoped a-SiGe:H -, in the Japan Society of Applied Physics and Related Societies, Extended Abstracts (The 34th Spring Meeting, 1987), p217.

(8) K. Abe, Y. Nitta, Y. Tsutsumi, H. Okamoto and Y. Hamakawa:
"Study of gap states by below-gap modulated photocurrent spectroscopy (III) - undoped a-Si:H -, in the Japan Society of Applied Physics, Extended Abstracts (The 48th Autumn Meeting, 1987), p253.

(9) K. Abe, T. Wada, Y. Tsutsumi, H. Okamoto and Y. Hamakawa:
"Study of gap states by below-gap modulated photocurrent spectroscopy (IV), in the Japan Society of Applied Physics and Related Societies, Extended Abstracts (The 35th

Spring Meeting, 1988), p346.

(10) K. Uchiyama, Y. Tsutsumi, K. Hattori, H. Okamoto and Y. Hamakawa: "Study of gap-states by transient primary-photocurrent (II)", in the Japan Society of Applied Physics, Extended Abstracts (The 51th Autumn Meeting, 1990), p703.

(11) H. Yamamoto, Y. Tsutsumi, H. Okamoto and Y. Hamakawa: "Evaluation of carrier mobility in a-Si:H alloys by polarized electroabsorption", in the Japan Society of Applied Physics, Extended Abstracts (The 54th Autumn Meeting, 1993), p824.

(12) H. Yamamoto, Y. Tsutsumi, S. Yoshihara, H. Okamoto and Y. Hamakawa: "Evaluation of carrier mobility in a-Si alloys by polarized electroabsorption (II)", in the Japan Society of Applied Physics and Related Societies, Extended Abstracts (The 41th Spring Meeting, 1994), p810.